A Transport Laser with Shape and Amplitude Control for Ultracold Strontium Atoms

Ein Transportlaser mit Form- und Amplitudenkontrolle für ultrakalte Strontiumatome

Wissenschaftliche Arbeit zur Erlangung des Grades
M.Sc. im Studiengang Applied and Engineering Physics
an der Fakultät für Physik der Technischen Universität München.

Betreut von Prof. Dr. Rudolf Gross

Lehrstuhl für Technische Physik der Technischen Universität München

Direktor des Walther-Meißner-Instituts für Tieftemperaturforschung

Prof. Dr. Immanuel Bloch

Lehrstuhl für Experimentalphysik der Ludwig-Maximilians-Universität

Direktor am Max-Planck-Institut für Quantenoptik

Eingereicht von Fabian Finger

Ulmenweg 10

84186 Vilsheim

Eingereicht am München, den 5.10.2018

Contents

List of Figures

List of Tables

Abstract

In this thesis, we report on a system for a dynamically shaped optical dipole trap and optical transport. We were able to generate an optical dipole trap where shape and amplitude can be individually controlled. The beam size is tuned by using focus-tunable lenses as an adjustable telescope. Moreover, the aspect ratio of the beam is shaped using a frequency modulated acousto-optic deflector. This deflector is scanning the beam along one dimension to generate a time-averaged dipole potential. As a result, we achieved a vertical waist of 23 µm and a horizontal waist of 541 µm yielding an aspect ratio of 23.5. Besides, the RF power of the deflector is modulated to counteract frequency-dependent efficiency losses. This modulation also allows for different amplitudes of the dipole trap, enabling a variety of evaporative cooling schemes. Furthermore, the system can optically transport atoms using the adjustable telescope in combination with an additional diverging tunable lens. After reshaping the beam to a waist of 148 µm, we reproduced the same waist over a distance of 95 cm.
In conclusion, this system offers a highly-controllable way of generating optical dipole traps of varying size and power. It also enables the optical transport of strontium atoms into our second vacuum chamber.

1 Introduction

Not even the best classical computers today can simulate the most complex quantum many-body problems. The numerical power needed to keep track of all degrees of freedom in such systems scales exponentially with their size. For instance, describing a system of N spin-1/2 particles requires 2^N numbers. In this example, taking only $N = 70$ particles would demand 5×10^9 terabytes of data to represent the full state of the system, assuming single precision. For comparison, this amount of storage is about 3 times larger than the projected global IP traffic in 2018 [1].

In general, solving analytical models for many-body problems is difficult and good approximations are rarely available [2]. However, these models are at the heart of many fields such as high-energy physics, condensed matter physics, or quantum chemistry. A famous example is the Hubbard model, the simplest model of interacting particles in a lattice – a situation naturally found in solids [3]. A breakthrough was achieved, when, for the first time, the so-called Bose-Hubbard model for bosonic particles could be experimentally realized, *i.e.*, *simulated*, with an atomic gas in an optical lattice [4]. This experiment entered the regime of strong atom-atom interaction in an atomic gas, complementing the very successful theory of weakly interacting atomic gases [5]. The authors used optical lattices, generated by interfering several laser beams, which can trap atoms by taking advantage of the latter's induced dipole moment [6]. This ability allows them to model highly-controllable, "artificial" crystals of light. The model's fermionic counterpart, the Fermi-Hubbard model [7], is strongly connected to a another very prominent phenomenon: high-T_c superconductivity [8–10]. High-T_c materials conduct current without losses already above liquid nitrogen temperatures of 77 K. Fully understanding them might give rise to the development of room temperature superconductors, which would greatly advance today's technology, reaching from medicine to industry [3]. However, a complete theory of high-T_c superconductivity remains, to date, one of the major open questions in quantum many-body physics.

Studying quantum many-body systems also greatly benefited from a second breakthrough – the realization of *quantum gas microscopes*. Quantum gas microscopes combine optical lattices with high resolution fluorescence detection, and were first demonstrated for alkali metals like rubidium [11, 12]. This new tool allowed for manipulation and precision read-out of quantum systems at the single-atom level, providing, *e.g.*, access to unique correlations otherwise difficult to measure [13].

From today's perspective, following the route of *quantum simulation* presumably offers the only way to fully understand quantum many-body systems [14]. In our experiment, we also want to perform quantum simulation, but with strontium, an alkaline earth metal [15]. Its rich electronic structure, with singlet and triplet states connected by narrow intercombination lines, famously established strontium as an ideal candidate for atomic clocks and high precision measurements like atom interferometers [16].

In our experimental sequence, we take advantage of strontium's unique electronic properties, with the aim of obtaining degenerate strontium quantum gases. We start by laser cooling strontium atoms inside our first vacuum chamber in a "blue", 461 nm magneto-optical trap (MOT) and a subsequent "red", 689 nm MOT [17]. The red MOT is special in the sense that, due to its narrow transition linewidth, it allows us to reach µK temperatures on very fast timescales of ~ 100 ms. Moreover, the trapped atomic gas in the red MOT has a very particular, elliptical shape with aspect ratios of up to 1:20 [18], strongly dependent on the bosonic or fermionic nature of the used strontium isotope. All these properties determine our subsequent optical dipole trap (ODT). It too should be able to form a highly elliptical shape to assure good phase-space overlap between the red MOT and the ODT, whilst achieving high vertical trapping frequencies [17] – otherwise the atoms would escape due to gravity. High vertical trapping frequencies are especially important for evaporative cooling [17], crucial for achieving quantum degeneracy [19]. Finally, we want to load the atoms into our optical lattices, generated inside our second vacuum chamber. However, our first and second vacuum chambers are physically separated by at least 50 cm to allow for better optical access to the microscope. This setup thus necessitates an optical transport scheme connecting both chambers.

In this Master's thesis, we report on my work on the last steps in this experimental sequence: the engineering of a setup which creates the optical dipole trap, including a controllable shape and amplitude, as well as performing the optical transport. This setup is shown in a simplified way in Fig. 1.1.

This thesis is structured as a guide through the preceding steps of the experiment and the presented setup. In Chapter 2, we start by exploring strontium, review the basics of laser cooling of neutral atoms and apply these to our experimental sequence for strontium. Specifically, we take a look at optical trapping of neutral atoms and the important concept of time-averaged potentials, which allows us to "paint" arbitrary potential landscapes for the atoms. In Chapter 3, we investigate the 1070 nm dipole laser used for this setup by

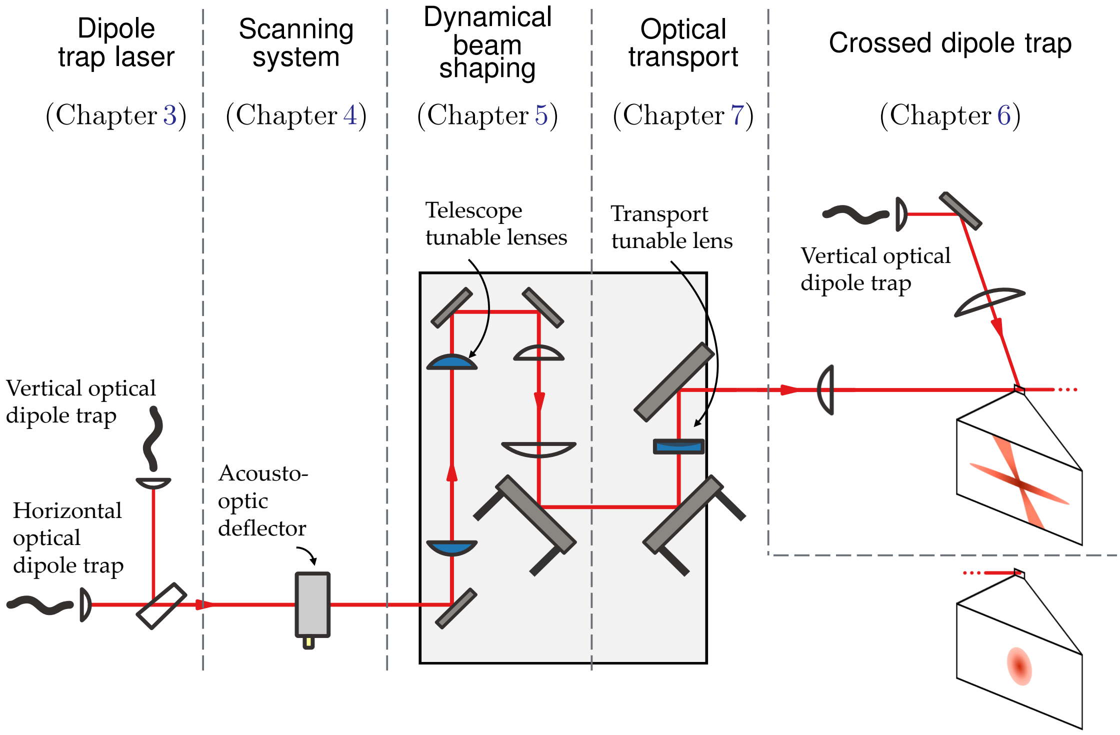

Figure 1.1 | Schematic overview of the transport laser setup with shape and amplitude control Each part of the setup (separated by the dashed lines) is described in the corresponding Chapter.

measuring its emission spectrum and relative intensity noise. In Chapter 4, we present the ideas behind the scanning system used to deflect our dipole laser beam and generate the aforementioned time-averaged potential. In Chapter 5, we show how to further tailor the dipole laser to our needs by dynamically adjusting the beam size. For that purpose, we take advantage of an adjustable telescope that uses focus-tunable lenses. In Chapter 6, we deduce the requirements for the shape and amplitude control of our optical dipole trap. Additionally, we simulate its trap potential and benchmark its performance in a test setup. In Chapter 7, we describe how to realize the optical transport with another type of focus-tunable lens. As before, we examine its performance in theory and in a test setup. Finally in Chapter 8, we summarize the most important results and take a look at future prospects.

2 Trapping and cooling of strontium

This Chapter lays the theoretical foundation for the trapping and cooling of strontium atoms in our experiment.

In Sec. 2.1, we explore the atomic and electronic properties of strontium and its isotopes. In Sec. 2.2, we give a brief review of the semiclassical interaction of neutral atoms with light. Based on this discussion, in Sec. 2.3, we show how to cool strontium atoms with light. Moreover, we explain how to confine them using an additional magnetic field, which results in a magneto-optical trap (MOT). Finally, we examine in Sec. 2.4 how to trap strontium atoms only using light, forming an optical dipole trap (ODT). We also introduce the concept of time-averaged potentials.

2.1 Strontium

In this Section, we give a short overview of the most important properties of strontium, crucial for understanding our experimental sequence.

Strontium is an *alkaline earth metal* with atomic number 38 and four naturally occurring isotopes as shown in Table 2.1.

Table 2.1 | Strontium isotopes and their properties. The data was taken from Stellmer *et al.* [19]

Isotope	Abundance	Nuclear spin I	Statistics
^{84}Sr	0.56%	0	Bosonic
^{86}Sr	9.86%	0	Bosonic
^{87}Sr	7.00%	9/2	Fermionic
^{88}Sr	82.58%	0	Bosonic

Depending on the number of fermionic particles like electrons, protons and neutrons in an atom, the atom is either fermionic (odd number) or bosonic (even number). As for all isotopes, there is an equal number Z of electrons and protons. This contribution is thus always even in every isotope. As a result, only the number of neutrons N determines the statistics of the strontium isotopes. Since for strontium $Z = 38$, the parity of the total number of fermions can be directly inferred from the familiar mass number $A = Z + N$. Therefore all strontium isotopes of even mass number are bosonic and all isotopes of odd mass number are fermionic. Additionally, ^{87}Sr has a non-zero nuclear spin $I = 9/2$. Strontium has a rich electronic structure of which only a small part, most relevant for the experiment, is depicted in Fig. 2.1.

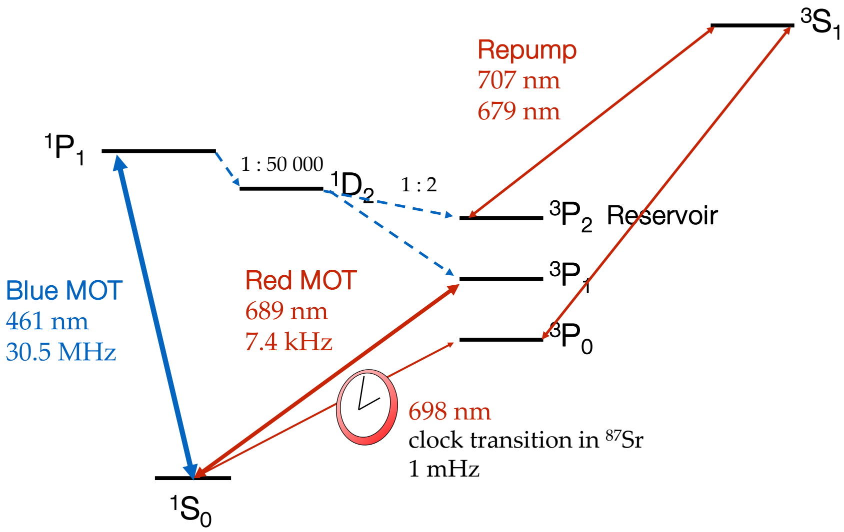

Figure 2.1 | Simplified electronic level structure of strontium. The data was taken from Boyd [20]. The electronic ground state is the 5s^2 $^1S_0$ state. Transitions between singlet and triplet states are dipole forbidden via the $\Delta S = 0$ selection rule. The transition from the ground state to the 5s4p $^3P_0$ state is even doubly forbidden breaking the $\Delta J = 1$ selection rule. This transition has a finite transition rate only in ^{87}Sr due to hyperfine state mixing. It is also called a *clock transition* because of its use in atomic clocks. The meaning of other special names for certain transitions is explained in the text.

The two electrons in the outer shell of strontium can form a *singlet* or *triplet state*, depending on their spin orientation. The electronic ground state is the 5s^2 $^1S_0$ state. In general, transitions between singlet and triplet states are dipole forbidden via the $\Delta S = 0$ selection rule. The transition from the ground state to the 5s5p $^3P_0$ state is even doubly forbidden breaking the $\Delta J = 1$ selection rule. Only the fermionic isotope ^{87}Sr is special in that sense. There, the transition has a finite rate due to hyperfine state mixing [21]. Because of its extraordinarily narrow linewidth, this transition is very useful for atomic clocks [18]. Therefore, this transition is also called a *clock transition*. Two transitions called the *"blue" and "red" MOT* are used to trap strontium atoms in magneto-optical traps, named after the color of the corresponding wavelengths. The *repump* transitions are used to optically pump atoms from the $^3P_2$ and $^3P_0$ states back to the ground state, which is crucial for the blue MOT.

2.2 Atom-light interaction: Semiclassical model for two-level atoms

In the last Section, we already mentioned several important transitions in strontium. These transitions are intimately connected to our experimental sequence and its physical principles. Before we start explaining these parts, we quickly review the basics of atom-light interaction. This knowledge is essential for understanding the following Sections.

Let us first consider a neutral two-level atom with ground state $|1\rangle$ and excited state $|2\rangle$. Both states are separated by an energy $\hbar\omega_{21}$, where ω_{21} is the transition frequency and $\hbar$ is the reduced Planck constant. The excited state decays with a rate $\Gamma \equiv 1/\tau$, called the *natural linewidth*, where τ is the lifetime of the state. We let this two-level atom interact with light, described by a classical electric field $\mathbf{E}(\mathbf{r},t) = \mathbf{E}_0 \mathrm{e}^{-i\mathbf{k}\cdot\mathbf{r}} \mathrm{e}^{i\omega t}$, where $\mathbf{E}_0$ is the amplitude of the electric field with its direction called the polarization, $\mathbf{k}$ is the wavevector with wavenumber k, $\omega = 2\pi f$ is the angular frequency of the field with frequency f, and $\lambda = c/f$ is the wavelength in the medium, here assumed to be vacuum. The coupling strength between the atom and the electric field is given by the *effective Rabi frequency* Ω' [17]

$$
\begin{aligned}
\Omega' &\equiv \sqrt{\Omega^2 + \Delta^2}, \\
\Omega &\equiv -\frac{e|\mathbf{E}_0|}{\hbar} \langle 2|r|1\rangle ,
\end{aligned}
\tag{2.1}
$$

where we defined the on-resonance Rabi frequency Ω with electron charge e, electron coordinate r, and the *detuning* $\Delta \equiv \omega - \omega_{21}$. We assume here that the electric field is not spatially dependent over the atom since the optical wavelengths of our transitions $\approx 400 - 700\,\mathrm{nm}$ usually exceed the atomic dimensions $\approx 0.25\,\mathrm{nm}$ of strontium by far. This approximation is called the *electric dipole approximation.* As outlined in many textbooks (see, *e.g.*, Metcalf and Van der Straten [17]) using the density-matrix formalism, the *excited state population* in the steady state is given by the diagonal matrix element

$$
\rho_{22} = \frac{s_0/2}{1 + s_0 + (2\Delta/\Gamma)^2}, \tag{2.2}
$$

where we defined the on-resonance saturation parameter $s_0 \equiv 2|\Omega|^2/\Gamma^2 = I/I_s$, with the field intensity $I(\mathbf{r},t) = 1/2\epsilon_0 c|\mathbf{E}(\mathbf{r},t)|^2$, and the saturation intensity $I_s \equiv \pi hc/(3\lambda^3\tau)$. The atom scatters photons with a *scattering rate* [17]

$$\Gamma_{\mathrm{sc}} = \Gamma\rho_{22}, \tag{2.3}$$

which is directly proportional to the natural linewidth Γ. This absorption and subsequent emission, *i.e.*, scattering of photons with momentum $\hbar\mathbf{k}$, gives averaged over time, a force, called the *radiation pressure force* [17]

$$\mathbf{F}_{\mathrm{sc}} = \hbar\mathbf{k}\Gamma_{\mathrm{sc}} = \hbar\mathbf{k}\frac{\Gamma}{2}\frac{s_0}{1+s_0+(2\Delta/\Gamma)^2}, \tag{2.4}$$

where we assumed that the momentum transfer by the photons is always aligned with the direction of light propagation $\hat{\mathbf{k}}$, and the momentum change caused by subsequent spontaneous emission averages out. It is maximum on resonance, *i.e.*, for a vanishing detuning $\Delta = 0$, and increases with light intensity. This force can thus be used to perform *laser cooling of atoms* for $\Delta < 0$.

2.3 Zeeman slower and magneto-optical traps

After we reviewed the atomic properties of strontium and the basics of atom-light interaction, we go through the experimental sequence step-by-step and describe the physical principles behind it. We start in Sec. 2.3.1 with the oven and the Zeeman slower. In Sec. 2.3.2, we continue with an explanation of magneto-optical traps (MOT) in general and our "blue" MOT in detail. We then show in Sec. 2.3.3 the subsequent "red" MOT and how its narrow linewidth transition makes it different from the blue MOT. We also show the important differences between bosonic and fermionic isotopes that become especially apparent during this step. Finally, in Sec. 2.4, we explain the principles of optical dipole traps and take a look at the principle of time-averaged potentials.

2.3.1 Oven and Zeeman slower

In our experiment, we start with strontium atoms heated by the atomic oven (Createc *LT-DFC-40-10-WK-2B-SHE*) up to ≈ 600 °C Subsequently, they leave the oven in the x

direction. Then, they are slowed down by a *Zeeman slower* as shown in Fig. 2.2.

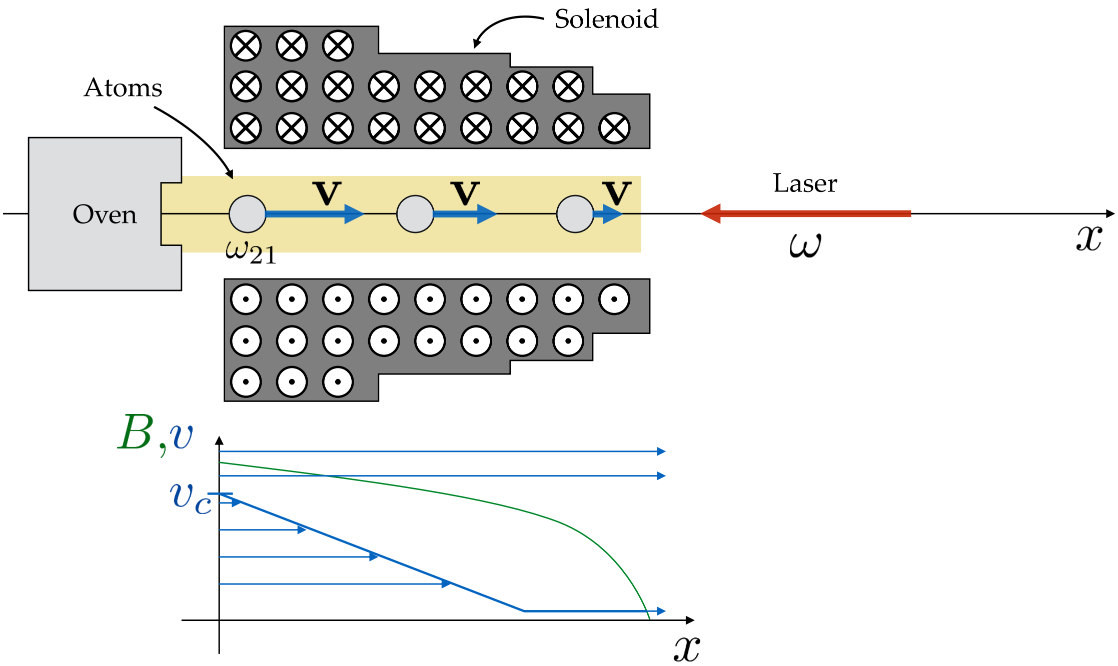

Figure 2.2 | Principle of a Zeeman slower. Atoms (yellow, highlighted in gray circles) with transition frequency ω_{21} leave an atomic oven in the x direction with a velocity $v = |\mathbf{v}|$. A counterpropagating laser beam of frequency ω (red arrow) and a non-uniform axial magnetic field $B(x)$ (green line in the lower graph) produced by a solenoid-like coil (dark gray) are tuned such that the atoms are always in resonance with the light. This condition makes the atoms constantly absorb photons incident from the $-x$ direction and subsequently emit them spontaneously into all directions. Looking at the classical phase-space trajectories (blue lines), one finds that below a critical velocity v_c, all atoms are slowed down to a smaller final velocity. (adapted from Inguscio and Fallani [22])

This procedure works as follows: in general, we want to slow these atoms down using a counterpropagating laser on resonance and thereby taking advantage of the maximum radiation pressure force defined in Eq. (2.4). However, the strontium atoms follow a *modified Maxwell-Boltzmann distribution* [23] and leave the oven with a mean velocity of $v = |\mathbf{v}| \approx 665\,\mathrm{m/s}$. Thus, to guarantee resonance, we have to make sure that the Doppler shifted frequency $\omega(1 + v/c)$ [22] seen by the atoms equals the transition frequency ω_{21}. However, once decelerated, the atoms will immediately move out of resonance with the laser again due to their altered Doppler shift. To constantly exert maximum force on them, we can use a position-dependent magnetic field $B(x)$ provided by a solenoid-like coil that Zeeman shifts the atomic energy level. For simplicity, let us take an atom with $J = 0$ in the ground state and $J' = 1$ in excited state to have, where J is the angular momentum quantum number. Then, the excited state will be shifted by an amount $\Delta E = \mu_B g_{J'} m_{J'} B(x)$. This Zeeman shift is tuned to always equal the Doppler shift $\hbar\omega v/c$, where $\mu_B = e\hbar/(2m_e)$ is the Bohr magneton, J is the angular momentum quantum number, g_J is the Landé factor, and m_J is the angular momentum component along the x direction [22]. For this step in our experiment, we use a broad transition with $\Gamma = 2\pi \times 30.5\,\mathrm{MHz}$, called the blue MOT transition (see Fig. 2.1). The angular momentum quantum numbers are $J = 0$ for the ground state $^1\mathrm{S}_0$ and $J = 1$ for the excited state $^1\mathrm{P}_1$. In conclusion, the Zeeman slower decelerates the atoms down to $30\,\mathrm{m/s}$, sufficient to be captured in the blue MOT.

2.3.2 Blue MOT

Before we take a look at the blue and red MOT, we will first explain the principle of *optical molasses/Doppler cooling*, see Fig. 2.3a.

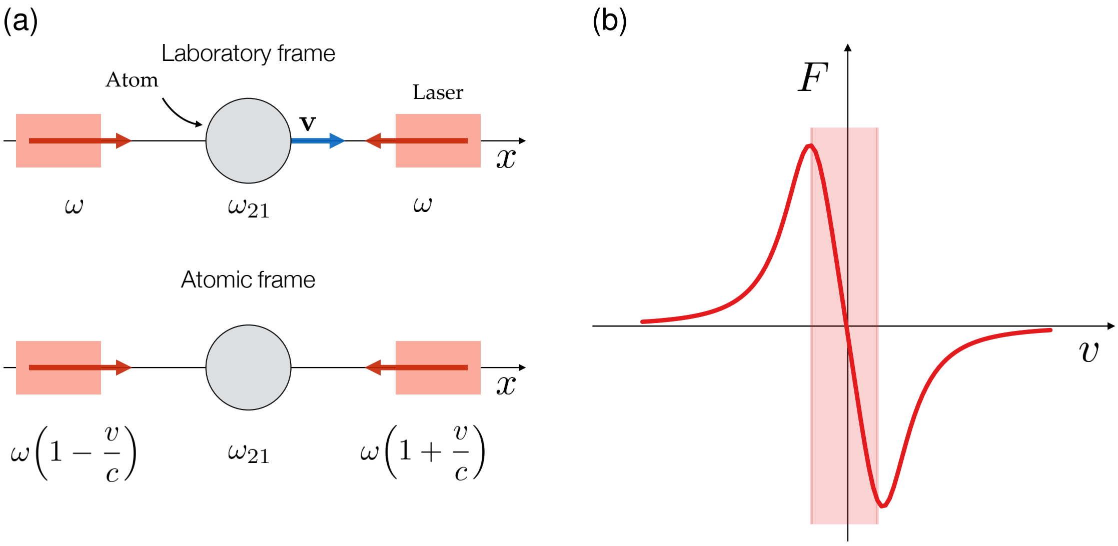

Figure 2.3 | Principle of 1D Doppler cooling. (a) In the laboratory frame, an atom (gray circle) moves with velocity $v = |\mathbf{v}|$ in the x direction and faces a copropagating and counterpropagating beam (red arrow) with frequency $\omega < \omega_{21}$. In the atomic frame, the atoms experiences the frequency of the counterpropagating beam as upshifted by $\omega v/c$ and vice versa for the copropagating beam. The atom will thus predominantly absorb photons from the upshifted $-x$ direction with momentum $\hbar\mathbf{k}$ and re-emit them spontaneously into all directions which leads to cooling in the $-x$ direction. This process takes place analogously for a movement in the other direction. (b) Magnitude of the damping force F defined in Eq. (2.5), experienced by the atom moving with velocity $v = |\mathbf{v}|$. For small velocities (red filled area), we can approximate this force as linear damping force. (adapted from Inguscio and Fallani [22])

Instead of one, we use two counterpropagating beams of frequency ω aligned with the velocity vector $\mathbf{v}$ of the atoms. The atom will experience an upshifted frequency $\omega(1 + v/c)$ of the counterpropagating beam and a downshifted frequency $\omega(1 - v/c)$ of the copropagating beam. For $\omega < \omega_{21}$, the counterpropagating beam will be closer to resonance and thus exert a larger average force (see Eq. (2.4)). In conclusion, the atoms experience a cooling force with shifted detuning compared to Eq. (2.4) [17]

$$\mathbf{F} = \hbar\mathbf{k}\Gamma\frac{s_0}{2}\left[\frac{1}{1+s_0+(2(\Delta-\mathbf{k}\cdot\mathbf{v})/\Gamma)^2} - \frac{1}{1+s_0+(2(\Delta+\mathbf{k}\cdot\mathbf{v})/\Gamma)^2}\right] \approx -\beta v, \tag{2.5}$$

which is shown qualitatively in Fig. 2.3b and can cool atoms in a velocity interval limited by the capture velocity $v_{\text{cap}} = \Delta/k$ [17]. For small velocities we can identify this cooling force simply as a frictional force with friction coefficient $\beta(\Delta)$ that is positive for “red” detunings $\Delta < 0$. The minimum temperature attainable with this technique is defined by two fundamental limits, namely

- the *Doppler temperature* [17]

  $$T_{\text{Doppler}} = \frac{\hbar\Gamma}{2k_B}, \tag{2.6}$$

  where k_B is the Boltzmann constant. It is obtained for optimal detuning $\Delta = -\Gamma/2$ and related to the equilibrium between cooling and heating rates, and

- the *recoil temperature* [17]

  $$\begin{aligned} T_{\text{recoil}} &\equiv \frac{\hbar^2 k^2}{2k_B m}, \\ \omega_r &\equiv \frac{\hbar k^2}{2m}, \end{aligned} \tag{2.7}$$

  associated to the recoil of a single photon. We also defined a *recoil frequency* for convenience.

However, this force is only decelerating. It does not provide any spatial confinement and as a result the atomic cloud would expand diffusively. To prevent that, one adds a quadrupole magnetic field $B(x) = bx$ with gradient b, created by a pair of coils in an anti-Helmholtz configuration, as shown in a simplified way in Fig. 2.4a.

The position-dependent Zeeman shift of the excited state $J' = 1$ is again $\Delta E = \mu_B g_{J'} m_{J'} bx$, where b is chosen such that $g_{J'} b > 0$. To understand how this configuration causes spatial confinement and prevents the cloud from expanding, consider first an atom slowed down and located at $x > 0$ as shown in Fig. 2.4a. The Zeeman shift of the magnetic quadrupole field causes the atom to preferentially absorb a photon from the σ^- beam, since this beam

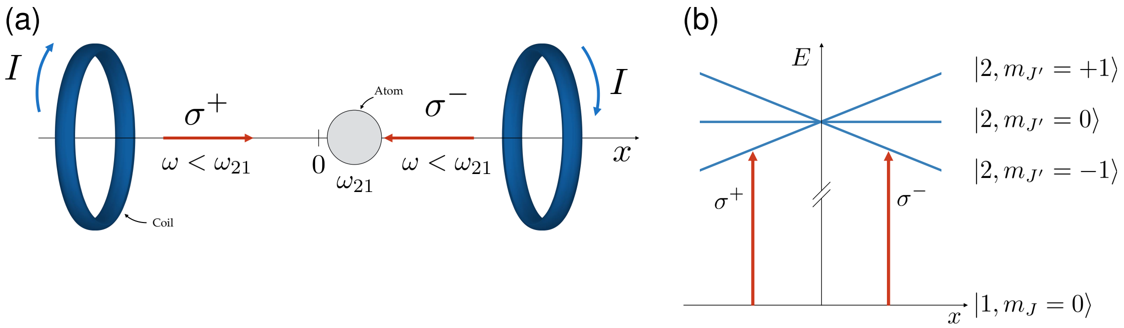

Figure 2.4 | Principle of a 1D MOT. (a) An atom located at $x > 0$ interacts preferably with one of the two red-detuned counterpropagating laser beams of opposite circular polarizations $\sigma^{\pm}$. Also present is a magnetic field B generated by two quadrupole coils with counter-circulating current I. (b) Energy level splitting of an atom having an angular momentum quantum number $J = 0$ for the ground state and $J' = 1$ for the excited state in the presence of the magnetic field. The absorption of polarized photons becomes spatially-dependent. (adapted from Inguscio and Fallani [22])

is closer to resonance (see Fig. 2.4b). In addition to cooling, the force is also directed towards the trap center and we obtain a *magneto-optical trap (MOT)*. The total force is [17]

$$\begin{aligned}\mathbf{F} &= \hbar\mathbf{k}\Gamma\frac{s_0}{2}\left[\frac{1}{1+s_0+(2(\Delta-\mathbf{k}\cdot\mathbf{v}-\mu_B g_{J'} bx/\hbar)/\Gamma)^2}-\frac{1}{1+s_0+(2(\Delta+\mathbf{k}\cdot\mathbf{v}+\mu_B g_{J'} bx/\hbar)/\Gamma)^2}\right],\\ &\approx -\beta v - kx.\end{aligned} \tag{2.8}$$

The MOT works only for velocities below a certain capture velocity. As before, a small velocity expansion reveals a friction force, this time combined with a restoring force. Taking the blue MOT transition at 461 nm, we have a standard broad laser cooling line, where the ratio of the power-broadened linewidth $\Gamma' = \Gamma\sqrt{1+s_0}$ to the single photon recoil frequency is $\Gamma'/\omega_r \sim 3\times10^3$. The Doppler temperature is $T_{\mathrm{Doppler},461} = 732\,\mu\mathrm{K}$ and the recoil temperature is $T_{\mathrm{recoil},461} = 518\,\mu\mathrm{K}$ for ^{87}Sr. In the experiment, the atoms are slow enough after the Zeeman slower to be loaded into the blue MOT. We use a magnetic field gradient of ≈ 50 G/cm along the vertical axis and ≈ 25 G/cm along the other two axes. The MOT beams have a detuning of 30 MHz, an average beam waist of ≈ 6 mm, an average power of ≈ 4 mW along the vertical axis and ≈ 5 mW along the other two axes yielding $s \sim 1$. As a result, we are able to cool the atoms down to 1 mK, close to the Doppler temperature. We note that the blue MOT transition is not fully closed (see Fig. 2.1). Atoms can decay over the intermediate state $^1D_2$ into the $^3P_2$ state and accumulate there. This state functions as a reservoir and is only limited by the vacuum lifetime, which is $\approx 30-50$ s in our case. The other excited atoms return to the ground state.

2.3.3 Red MOT

To continue efficient cooling of the atoms further after the blue MOT, we need to optically pump the atoms from the reservoir state $^3P_2$ back to the ground state. We accomplish this by using two repumping lasers. The 707 nm repumping laser is used to optically pump atoms from the $^3P_2 \rightarrow ^3S_1$ state. From there they decay back from $^3S_1 \rightarrow ^3P_1$ and subsequently from $^3P_1 \rightarrow ^1S_0$. But atoms in the $^3S_1$ state can also decay from $^3S_1 \rightarrow ^3P_0$, which has a very long lifetime $\approx 150\,\mathrm{s}$ [24]. Therefore, we need to use a second 679 nm repumping laser to again pump these atoms back from $^3P_0 \rightarrow ^3S_1$. Now they have once more the possibility to decay from $^3S_1 \rightarrow ^3P_1$ and then from $^3P_1 \rightarrow ^1S_0$ back to the ground state.

With all atoms in the ground state, we can start to operate laser cooling on the "red" MOT intercombination line (see Fig. 2.1). In contrast to the blue MOT, the red MOT intercombination line is a narrow laser cooling line, where the ratio of the power-broadened linewidth Γ' to the single photon recoil frequency is $\Gamma'/\omega_r \sim 1$ or less.

We first examine the behavior of the red MOT for the *bosonic* isotopes resembling our former setting where $J = 0$ for the ground state and $J = 1$ for the excited state.

The nature of the cooling strongly depends on the detuning Δ and the saturation parameter s. As a result, we can qualitatively distinct two regimes [25] relevant in this setting:

1. $\Delta < \Gamma'$: For small detunings and high intensities, the situation is analog to standard broad line Doppler cooling as shown for the blue MOT. The ratio of maximum radiative to gravitational force $\hbar k\Gamma'/(2mg)$ is about 5 orders of magnitude [20], so gravity can be safely ignored. The atoms will accumulate at the position, where the Zeeman resonance condition is fulfilled. This condition is mainly determined by the axial and radial magnetic field gradients of the two coils. Thus the atoms are confined to a resonance region resembling an ellipsoid of aspect ratio $\sim 2:1$ [24].

2. $\Delta > \Gamma'$: For large detunings and low intensities however, the cooling dynamics are strongly altered. Now the ratio of maximum radiative to gravitational force $\hbar k\Gamma'/(2mg)$ is usually only on the order of ~ 16, so gravity plays a role. As a result, the atoms will accumulate at the position, where the Zeeman resonance condition including a gravitational energy shift is fulfilled. This modification causes the atoms

to "sag" to the lower part of the resonance ellipsoid, creating a "pancake"-shaped MOT (see Fig. 2.5b).

For the *fermionic* MOT, the situation is more complex because of the non-vanishing nuclear spin $I = 9/2$. The excited $^3P_1$ state with $J = 1$ now experiences splitting into several hyperfine states $F = I \pm J$ with $F = 11/2, 9/2$ and $7/2$. Each of the hyperfine states also has $2F + 1$ m_F substates. Depending on the substate the atoms can be either attracted or repelled from the trap center [20]. Briefly speaking, the solution to this problem is the use of an additional "stirring laser" on the $^1S_0, F = 9/2 \rightarrow ^3P_0, F = 9/2$ transition. The stirring laser effectively mixes the different m_F sublevels. As opposed to the bosonic case, we do not have only two cooling transitions where $\Delta m_J = \pm 1$ giving rise to one resonance ellipsoidal shell. Now, each transition where $\Delta m_F = \pm 1$ has its own Zeeman resonance ellipsoidal shell. All these shells effectively overlap and merge, creating a fermionic red MOT shape that resembles the one of a broad cooling transition as shown in Fig. 2.5a.

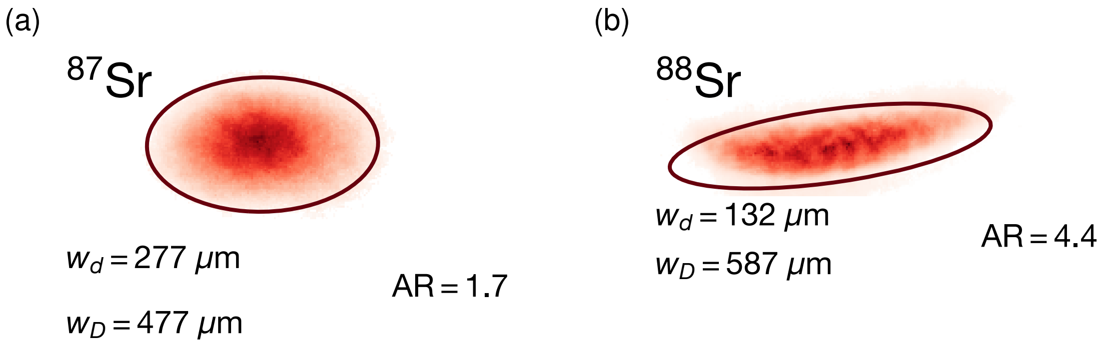

Figure 2.5 | Red MOTs of fermionic and bosonic strontium isotopes. (*a*) A typical picture of the red MOT for ^{87}Sr, obtained in our experiment. It is fitted by a 2D Gaussian (red solid lines mark the $1/e^2$ intensities) giving waists of $w_D = 477\,\mu m$ along the long axis and $w_d = 278\,\mu m$ along the short axis. The resulting aspect ratio AR $\equiv w_D/w_d$ is 1.7. The final single-frequency detuning here is -240 kHz. (*b*) A typical picture of the red MOT for ^{88}Sr, obtained in our experiment. It has a waist of $w_D = 587\,\mu m$ along the long axis and $w_d = 133\,\mu m$ along the short axis. The resulting aspect ratio AR $\equiv w_D/w_d$ is 4.4. Clearly visible is a sagging of the atoms, giving rise to a "pancake" shape. The final single-frequency detuning here is -150 kHz. For both pictures, the final magnetic field gradient is 0.65 G/cm.

In the experiment, after the blue MOT stage, we first ramp down the magnetic field gradient to 1 – 6 G/cm. At this point, the atoms have a temperature on the order of the Doppler temperature ≈ 1 mK, which is far bigger than the corresponding Doppler temperature $T_{\text{Doppler},689} = 178$ nK or the recoil temperature $T_{\text{recoil},689} = 232$ nK of the red MOT. Thus, their velocity is also larger than the capture velocity of the red MOT. Therefore, to capture the atoms, we use a broadband red MOT, where we modulate the frequency of the light with a sawtooth waveform of period 40 µs in a detuning range of −8 MHz to ±100 kHz. This modulation allows us to cover a large fraction of the velocity distribution of the atoms. This technique is a modified version of *laser cooling by sawtooth-wave adiabatic passage* [26]. We also ramp the beam powers for every axis from 4 mW → 1 mW. We use a beam waist of 3 mm, giving $s \gg 1$. We end up with 10^7 atoms of ^{87}Sr or 10^8 atoms of ^{88}Sr at a temperature of 10 µK. The last step is a single frequency red MOT stage, where we ramp the detuning from −350 kHz → −150 kHz in 10 ms for ^{87}Sr and 50 ms for ^{88}Sr. During this ramp, we keep the magnetic field gradient at 1 G/cm and lower the beam powers to a few µW, equivalent to $s \sim 1$. The atoms are now at a final temperature of ≈ 1 µK without significant losses in atom number.

After the red MOT, we will load the atoms into an optical dipole trap that is explained in the next Section.

2.4 Optical dipole traps

Besides the diagonal elements in the density matrix for the two-level atom interacting with light (see Sec. 2.2), we also associate physical meaning with the off-diagonal elements. These off-diagonal elements are called *coherences* and describe the strength of the induced dipole moment $\mathbf{d}(\mathbf{r}, t)$ [17]. For *large detunings* $\Delta \gg \Gamma'$ with very small population in the excited state, $\rho_{22} \ll 1$, we find that this induced dipole moment is linearly proportional to the applied field $\mathbf{d}(\mathbf{r}, t) = \alpha(\omega)\mathbf{E}(\mathbf{r}, t)$, where the proportionality factor $\alpha(\omega)$ is called the *complex polarizability* [6]:

$$\alpha(\omega) = 6\pi\epsilon_0 c^3 \frac{\Gamma/\omega_{21}}{\omega_{21}^2 - \omega^2 - i(\omega^3/\omega_{21}^2)\Gamma}. \tag{2.9}$$

We can decompose this interaction into two parts:

1. The part of $\mathbf{d}$ in phase with $\mathbf{E}$ is dispersive and gives rise to a conservative *dipole*

potential resulting in the optical dipole force $\mathbf{F}_{\mathrm{dip}} = -\nabla V_{\mathrm{dip}}(\mathbf{r})$ [6]:

$$\begin{aligned} V_{\mathrm{dip}}(\mathbf{r}) &= -\frac{1}{2}\langle \mathbf{d}\cdot\mathbf{E}\rangle = -\frac{1}{2\epsilon_0 c}\mathrm{Re}(\alpha)I(\mathbf{r}), && (2.10a)\\ &= -\frac{3\pi c^2}{2\omega_{21}^3}\left(\frac{\Gamma}{\omega_{21}-\omega}+\frac{\Gamma}{\omega_{21}+\omega}\right)I(\mathbf{r}), && (2.10b)\\ &\approx \frac{3\pi c^2}{2\omega_{21}^3}\frac{\Gamma}{\Delta}I(\mathbf{r}), && (2.10c)\end{aligned}$$

where $\langle\rangle$ denotes the time average over rapid oscillating terms. In the last line, we made use of the rotating-wave approximation (see, *e.g.*, [27]). The factor 1/2 takes into account the induced nature of the dipole moment. For red detuning $\Delta < 0$ relevant here, the optical dipole potential is negative $V_{\mathrm{dip}} < 0$ and therefore attractive. Atoms are trapped at potential minima, *i.e.*, points of maximum intensity. In the other case of blue detuning $\Delta > 0$, the situation is reversed.

2. The part of $\mathbf{d}$ out-of-phase with $\mathbf{E}$ is dissipative and gives rise to absorption of energy from the driving field $\mathbf{E}$ by the oscillator. It is given here only for completeness and is the already known *scattering rate* [6]:

$$\begin{aligned} \Gamma_{\mathrm{sc}} &= \frac{1}{\hbar\epsilon_0 c}\mathrm{Im}(\alpha)I(\mathbf{r}), && (2.11a)\\ &= \frac{3\pi c^2}{2\hbar\omega_{21}^3}\left(\frac{\omega}{\omega_{21}}\right)^3\left(\frac{\Gamma}{\omega_{21}-\omega}+\frac{\Gamma}{\omega_{21}+\omega}\right)^2 I(\mathbf{r}), && (2.11b)\\ &\approx \frac{3\pi c^2}{2\hbar\omega_{21}^3}\left(\frac{\Gamma}{\Delta}\right)^2 I(\mathbf{r}), && (2.11c)\end{aligned}$$

where we again used the rotating-wave approximation.

For lasers not too far detuned, we can obtain a simple and insightful relation for optical dipole traps. Looking at Eq. (2.10c) and Eq. (2.11c), we deduce [6]

$$\hbar\Gamma_{\mathrm{sc}} = \frac{\Gamma}{\Delta}V_{\mathrm{dip}}. \tag{2.12}$$

Here, the dipole potential V_{dip} scales with I/Δ and the scattering rate scales with I/Δ^2. As a result, we should thus use large detunings and high intensities to keep the scattering rate as low as possible for a given trap depth.

We will conclude this Chapter by giving an example for an optical dipole trap. Consider, *e.g.*, a *circular Gaussian beam* with intensity profile [28]

$$I(r,z) = \frac{2P}{\pi w^2(z)} \exp\left(-\frac{2r^2}{w^2(z)}\right), \tag{2.13}$$

where P denotes the total power of the beam, $w(z) = w_0\sqrt{1 + z/z_R}$ is the $1/e^2$ beam radius with Rayleigh range $z_R = \pi w_0^2/\lambda$, minimal waist w_0 and wavelength λ, r is the radial coordinate, and z the axial coordinate. We take strontium as our two-level system with ground state $^1S_0$ and excited state $^1P_1$, which is the dominant, already known blue MOT transition. Let us also assume a 1070 nm laser that is far detuned from the 461 nm resonance. Inserting these parameters into Eq. (2.10a), assuming a red detuned beam $\Delta < 0$, and adding the gravitational potential mgy, gives us the dipole potential shown in Fig. 2.6a.

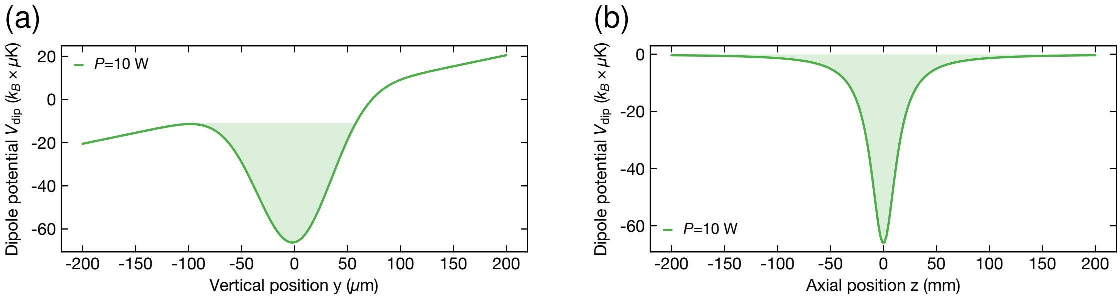

Figure 2.6 | Dipole potential for a circular Gaussian beam in radial and axial direction. The parameters used are $P = 10\,\mathrm{W}$ and $w(z) = w_0 = 70\,\mu\mathrm{m}$. (*a*) The dipole potential (green solid line) along the radial, vertical direction y provides strong confinement. Gravity induces a tilt in the potential along the vertical direction and reduces the effective potential depth (green filled area). (*b*) The dipole potential provides weak confinement in the axial direction. Note the comparable trap depths but the different units of the abscissas.

As we can see, a circular Gaussian beam provides weak confinement in the axial direction but strong confinement in the radial direction. Additionally, gravity induces a tilt in the potential specifically along the vertical direction and further reduces the effective potential depth.

However, we are not limited to circular traps. We can also imagine other geometries like elliptical traps. One way to generate these is by using cylindrical lenses. In contrast to this static method, we use a "dynamic" one. By "wiggling" a laser beam "fast enough" with an acousto-optic deflector, the beam will appear elliptical for the atoms. This so-generated potential is called a *time-averaged potential.*

In the experiment, we do use a high-power 1070 nm laser that is detuned from the dominant 461 nm blue MOT transition in strontium. This dipole laser is described in the next Chapter.

3 Dipole trap laser

In this Chapter, we describe the dipole trap laser used in our setup.

First, in Sec. 3.1, we discuss the laser's optical spectrum and determine its coherence length l_c. In Sec. 3.2, we investigate the laser's relative intensity noise spectrum and explain its characteristic peaks.

3.1 Optical spectrum and coherence length

It is crucial to have precise knowledge of the *optical spectrum* of the 1070 nm laser that we use, namely the central wavelength λ_c and the full width half maximum (FWHM) linewidth $\Delta\lambda$. To determine if unavoidable back reflections from viewports can cause standing waves via interference with incoming light, we also need to know the coherence length l_c of the laser.

The laser used in the experiment is a 100 W single-mode ytterbium fiber laser (IPG Photonics, *YLR-100-LP-WC*), its output beam waist is 1.67 mm as measured with a knife edge.

For measuring the laser's optical spectrum, we connected the laser to an optical spectrum analyzer (OSA, Ando, *AQ6315E*, 10 averages, resolution of 0.05 nm) with a polarization maintaining, single mode 1064 nm fiber (Thorlabs, *P3-1064PM-FC-5*). We used a fixed input power of ≈ 1 mW at the OSA, measured with the powermeter (Thorlabs, *PM100D* and sensor *S121C*). The measured optical power spectral density (OPD) as a function of wavelength λ is shown in Fig. 3.1a for different setpoints of the laser's maximum output power P_{out}. The thereof derived FWHM linewidth is shown in Fig. 3.1b.

From Fig. 3.1a, we can determine the central wavelength λ_c of the laser in air to be 1070.3(1) nm. This is in good agreement with the value of 1070.2 nm given in the datasheet [29]. The linewidth $\Delta\lambda$ broadens with increasing output power and shows linear behavior between 20 – 80 W. Below 20 W and above 80 W a saturation effect can

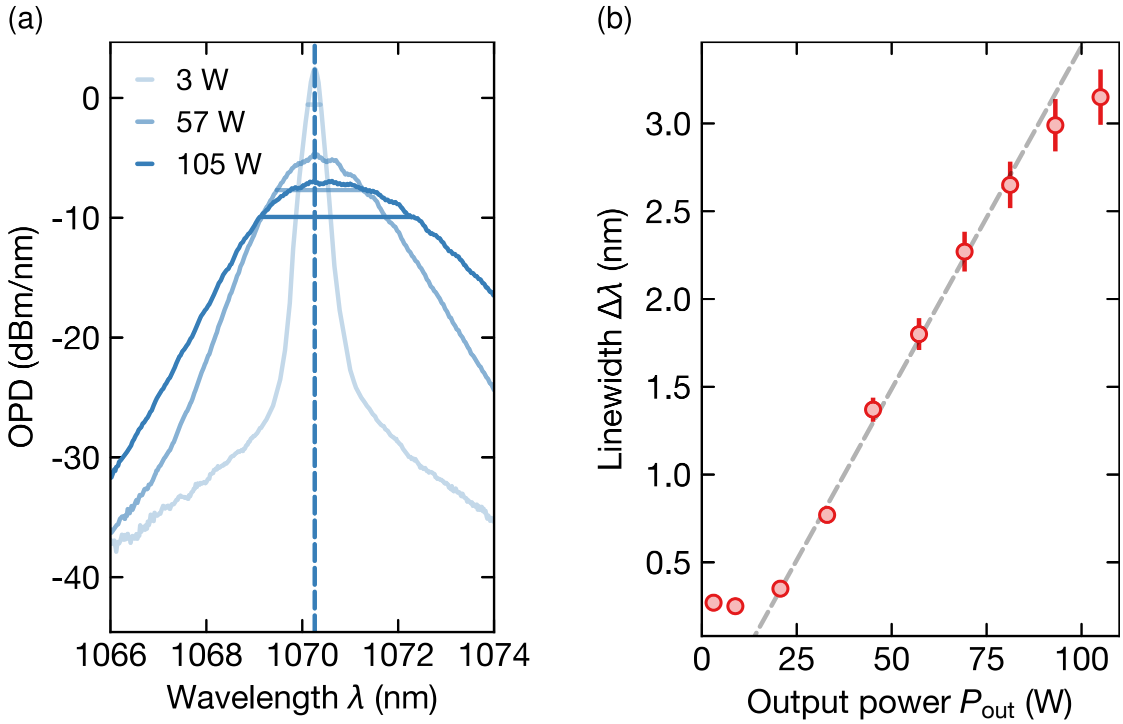

Figure 3.1 | Spectrum and linewidth $\Delta\lambda$ of the dipole laser for different output powers P_{out}. (a) Three exemplary spectra of the laser are shown for different output powers P_{out} of 3 W (light blue), 57 W (mid blue) and 105 W (dark blue). The horizontal lines indicate the respective linewidths. The central wavelength λ_c is 1070.3(1) nm (dashed line). The central peak decreases and broadens for higher output power. (b) The full width at half-maximum (FWHM) linewidth $\Delta\lambda$ as a function of output power is shown. The linewidth broadens with increasing output power and shows linear behavior (dashed line) between 20 – 80 W. Below 20 W and above 80 W a saturation effect can be observed. The error bars account for the increased noise at higher running power.

be observed. The origin of this broadening mechanism is explained in the subsequent Section.

From the central wavelength and the linewidth, we can calculate the *coherence length* of a presumed Lorentzian spectrum as [28]

$$l_c = c\tau_c = \frac{c}{\pi \Delta f} = \frac{\lambda_c^2}{\pi \Delta \lambda}, \tag{3.1}$$

where we defined the coherence time τ_c and the linewidth in the frequency domain Δf. We also used $|\Delta\lambda/\Delta f| \sim c/f^2$ for small wavelength intervals. We note that the coherence length is, despite its dimension, a measure for the *temporal* and not spatial coherence, as can be seen in Eq. (3.1). Mathematically speaking, the coherence length is the propagation length after which the magnitude of the temporal coherence function has dropped to $1/e$. Intuitively, the coherence length of a laser specifies over what length scales we can expect coherent behavior. Taking interferometers as a typical example, the coherence length should exceed at least the optical path length difference of the light. Otherwise, no interference fringes will be visible.

The calculated coherence length l_c for our laser as a function of linewidth $\Delta\lambda$ is shown in Fig. 3.2.

With increasing linewidth, corresponding to increasing output power (see Fig. 3.1b), the coherence length becomes shorter and reaches a minimum at about 0.12 mm. Comparing the maximum coherence length of 1.5 mm to the distance between the front and back viewport of ≈ 200 mm, we obtain a difference of two orders of magnitude. Thus, it is reasonable to assume that no standing waves caused by the interference between the incoming and backreflected laser light will occur.

3.2 Relative intensity noise spectrum

A good knowledge about the *relative intensity noise (RIN) spectrum* of the laser light is important to identify fluctuations around the average power of a laser.

For the RIN measurement, part of the laser light was coupled to a polarization-maintaining, single-mode 1064 nm fiber (Thorlabs, *P3-1064PM-FC-5*). After passing through a $\lambda/2$ waveplate (Newport, *10RP02-34*), a Brewster plate (ATF, *TFPI-1064-PW-1025-UV*) and

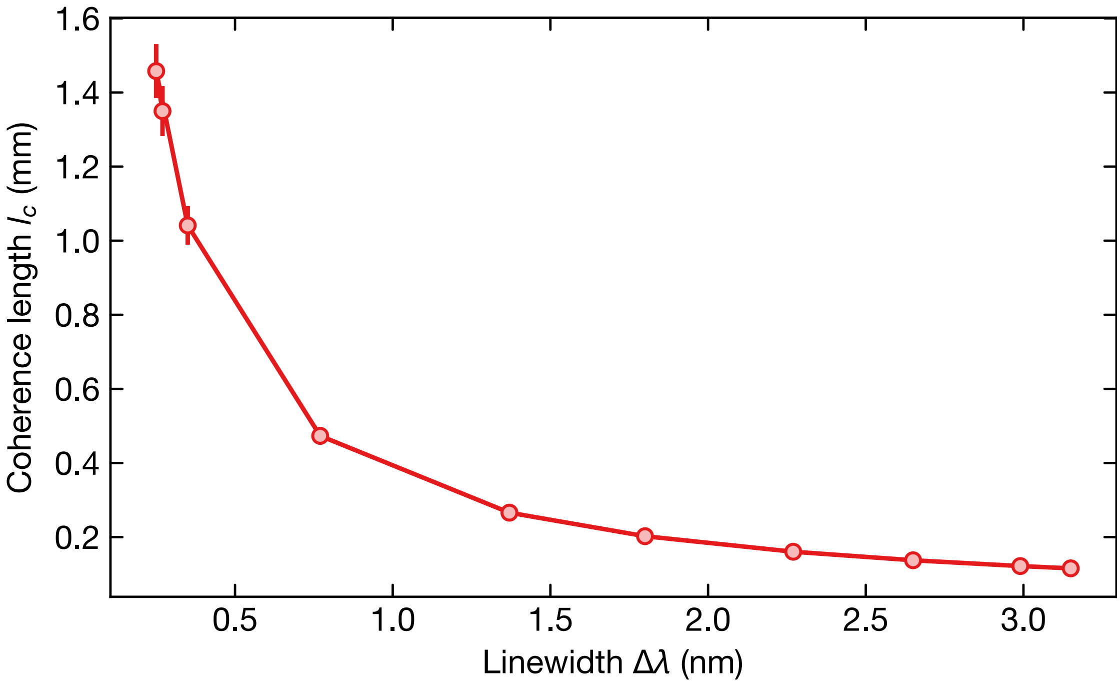

Figure 3.2 | Coherence length l_c as a function of linewidth $\Delta\lambda$. With increasing linewidth corresponding to increasing output power (see Fig. 3.1b), the coherence length becomes shorter and reaches a minimum at 0.12 mm. The errors are due to the finite precision in the linewidth measurement.

a beam sampler (Thorlabs, *BSF10-C*), the beam was aligned onto an InGaAs photodiode for 900 – 1700 nm (Thorlabs, *FGA10*) including a bandpass filter for 1070 nm (Thorlabs, *FB1070-10*) before the photodiode. The laser output power setpoint was tuned between 20-100% of its maximum power and the outcoupled power was adjusted such that at all times the same power of 0.3 mW was present at the photodiode. The output of the photodiode board [30] was then measured with multiple devices to cover the largest frequency range with the best precision, as summarized in Table 3.1. The complete RIN spectrum is shown in Fig. 3.3.

Table 3.1 | Devices and their settings for the measured intensity noise in different frequency spans. The spectra were combined using the unit conversions explained in App. B on page 89

Frequency span	Device	Relevant settings
DC/0 Hz	*Fluke 87V True RMS Multimeter*	Volt
0 – 100 kHz	*SR760 FFT Spectrum Analyzer*	RBW = 250 Hz, units = dBV_{rms}, number of averages = 1000, average type = RMS, average mode = linear
100 – 500 kHz	*Anritsu MS2721B*	RBW = 10 Hz, detection = RMS
500 kHz – 50 MHz	——"——	RBW = 100 Hz, ——"——

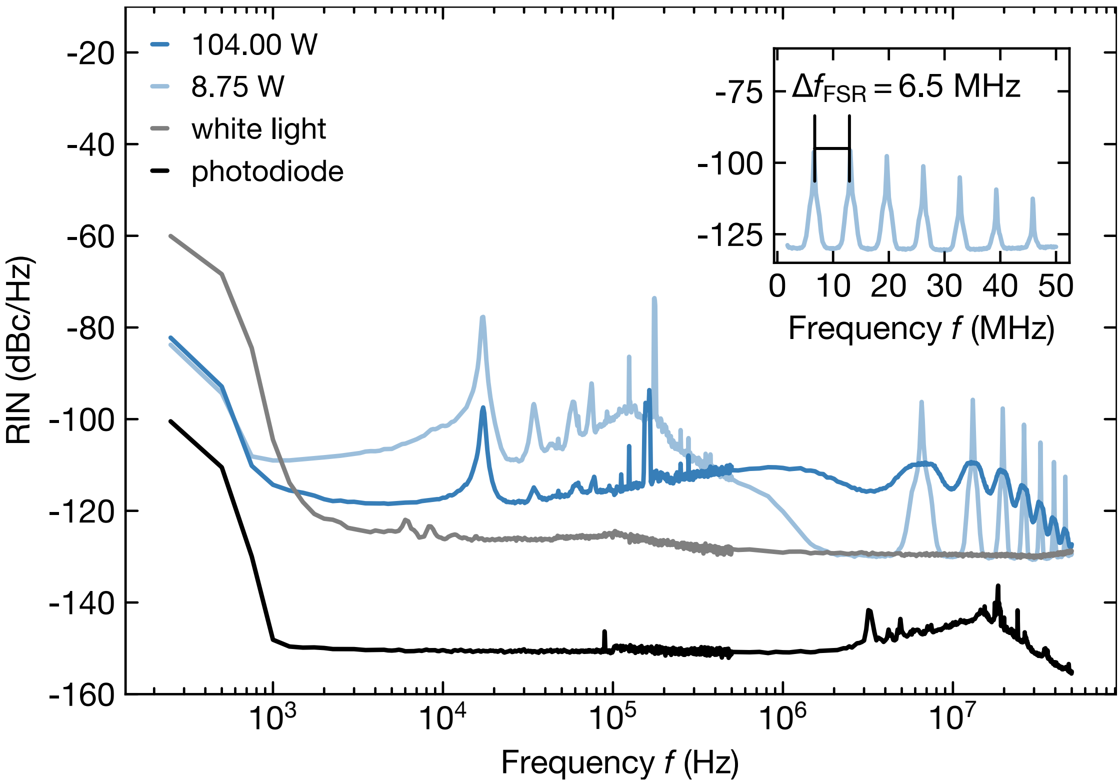

Figure 3.3 | Relative intensity noise versus frequency f. The photodiode (black) without light and the reference thermal light source (gray) both consist of broad peaks at low frequencies up to several 100 Hz and small electronic peaks. Both spectra are well below the two laser spectra at 8.75 W (mid blue) and 104 W (dark blue) output power above ≈ 1 kHz. In the 10 – 500 kHz regime, both laser spectra exhibit a series of relaxation oscillation peaks with comparable linewidth and position, but different height. Starting at 6.5 MHz, both laser spectra also show evenly spaced peaks (*inset*), which broaden for 104 W (see text for details). The total integrated normalized noise P/P_{dc} is $1.9 \cdot 10^{-9}$ for 8.75 W and $2.8 \cdot 10^{-8}$ for 104 W.

We take the photodiode itself without light, normalized similar to the other spectra, and a thermal light source (Euromex, *LE.5211*) as reference for the laser spectra. Both spectra show a broad peak at low frequencies up to several 100 Hz. Small electronic peaks at 100 kHz and above 2 MHz are visible in the photodiode spectrum. The thermal light source spectrum has additional electronic peaks slightly below 10 kHz and is well below the two laser spectra at 8.75 W and 104 W output power above ≈ 1 kHz. We conclude that all other features in the two laser spectra stem from the laser itself.

The peaks from 10 – 500 kHz in both spectra are very likely due to *relaxation oscillations*, which are typical for solid-state lasers [31]. These oscillations occur when the laser is perturbed by a small fluctuation in gain, cavity loss or alignment. The fluctuations can be caused, *e.g.*, by mechanical vibrations of the cavity, power supply noise or noise from the laser diode pumping the gain fiber of the fiber laser.

Starting at 6.5 MHz, both laser spectra also show evenly spaced *beat note* peaks. These beat notes can be understood by looking at a schematic picture of the oscillations in a laser, shown in Fig. 3.4.

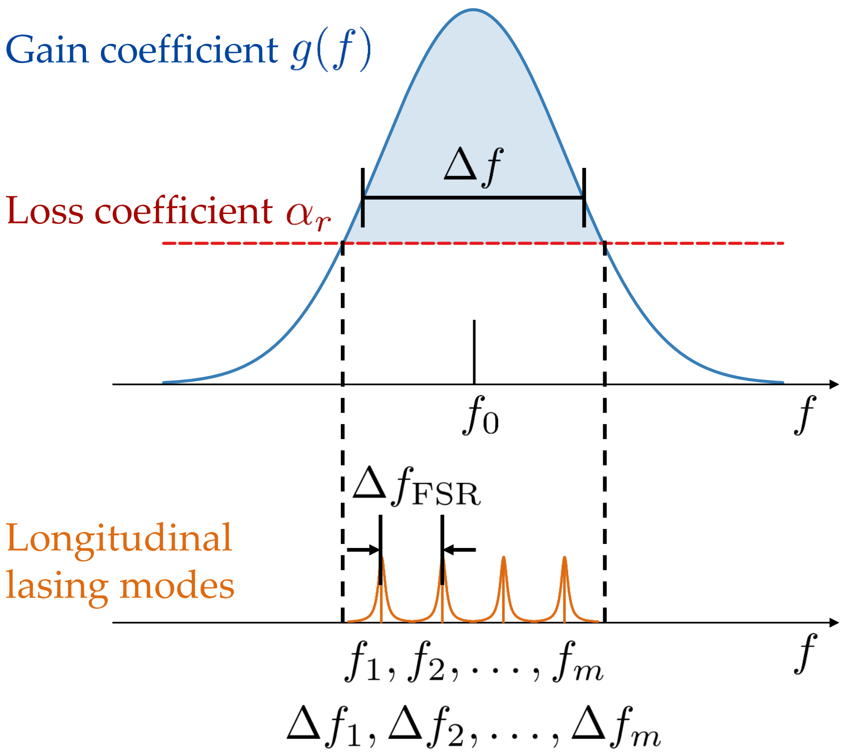

Figure 3.4 | Oscillating longitudinal modes in a laser. A laser medium is defined by its frequency-dependent gain coefficient $g(f)$ (blue solid line) of linewidth Δf and central frequency f_0. The cavity is characterized by its cavity loss coefficient α_r (red dashed line). The spacing of the cavity's longitudinal modes f_i with linewidth Δf_i is called the free spectral range Δf_{FSR}. The gain and loss coefficient restrict the manifold of longitudinal modes to a subset of lasing modes (orange).

A laser consists, in principle, of

- a medium with gain coefficient $g(f)$ of linewidth Δf and central frequency f_0 and
- a cavity with loss coefficient α_r that serves as cavity and defines the laser's longitudinal modes f_i with linewidth Δf_i, separated by the *free spectral range*

$$\Delta f_{\mathrm{FSR}} = \frac{c_0}{2n_1 L_r}, \tag{3.2}$$

defined by the vacuum speed of light c_0, the linear index of refraction of the gain medium n_1 and the cavity length L_r [32].

Not every longitudinal mode defined by the cavity is oscillating in a laser. Only the m longitudinal modes for which the gain coefficient exceeds the loss coefficient $g(f) > \alpha_r$ can lase. Each of these modes is of the form $U(t) = \sqrt{I}e^{j2\pi ft}$ [28]. Every single mode also interferes with its neighbors. As an example, consider nearest-neighbor interference between the modes of frequency f_1 and f_2. The combined field will be of the form $U(t) = \sqrt{I_1}e^{i2\pi f_1 t} + \sqrt{I_2}e^{i2\pi f_2 t}$. If we measure the resulting intensity of this field with a photodiode, we observe $I(t) = I_1 + I_2 + 2\sqrt{I_1 I_2}\cos[(2\pi(f_2 - f_1)t]$. Additionally to the constant intensity, a difference frequency – so-called beat note – is generated. This difference frequency of the lasing modes is equal to the free spectral range. Therefore, the first peak at around 6.5(1) MHz corresponds to the signal of all lasing modes interfering with their nearest neighbors. Consequently, all peaks at integer multiples i of Δf_{FSR} correspond to the signal generated by lasing modes interfering with their i^{th} neighbor mode. The peak height decreases with i since the number of interfering lasing modes also decreases.

From Eq. (3.2), we can determine the length $L_r = 15.4(2)$ m of the cavity in the fiber laser, taking a typical index of refraction $n_1 = 1.5$ for the gain fiber [31].

As can be seen from Fig. 3.3, most of the relaxation oscillation peaks keep their position and linewidth independent of output power. This highlights their origin outside of the gain medium. In contrast, the beat note peaks start to broaden for higher output powers. As an example, we measure and analyze the linewidth of the first beat note peak for different output powers (see Fig. 3.5a).

According to Lapointe and Piché [33], this linewidth broadening is not related to the deformation of the fiber Bragg gratings acting as mirrors in the gain fiber. Instead the broadening is associated to *four-wave mixing* (FWM) between the lasing longitudinal modes. For higher output powers, the nonlinear, intensity-dependent contributions to the index of refraction of the medium $n_2(I)$ start to become relevant such that $n = n_1 + n_2(I)$. This intensity dependent index of refraction leads to a nonlinear phase shift of the modes. Consequently, this phase shift broadens the linewidth of these modes [34].

Lapointe and Piché [33] observed a power-law relation between the linewidth and the output power of the laser with an exponent of ~ 1, assuming FWM being the major broadening mechanism. As shown in Fig. 3.5b, the linewidth indeed follows approximately linear behavior. This indicates that FWM is a good candidate to be the dominant broadening mechanism in this Ytterbium fiber laser. Since the beat note linewidth broadening is directly connected to the broadening of every longitudinal mode, the total linewidth of the laser, $\Delta\lambda$, will also broaden with increasing output power, as can be seen

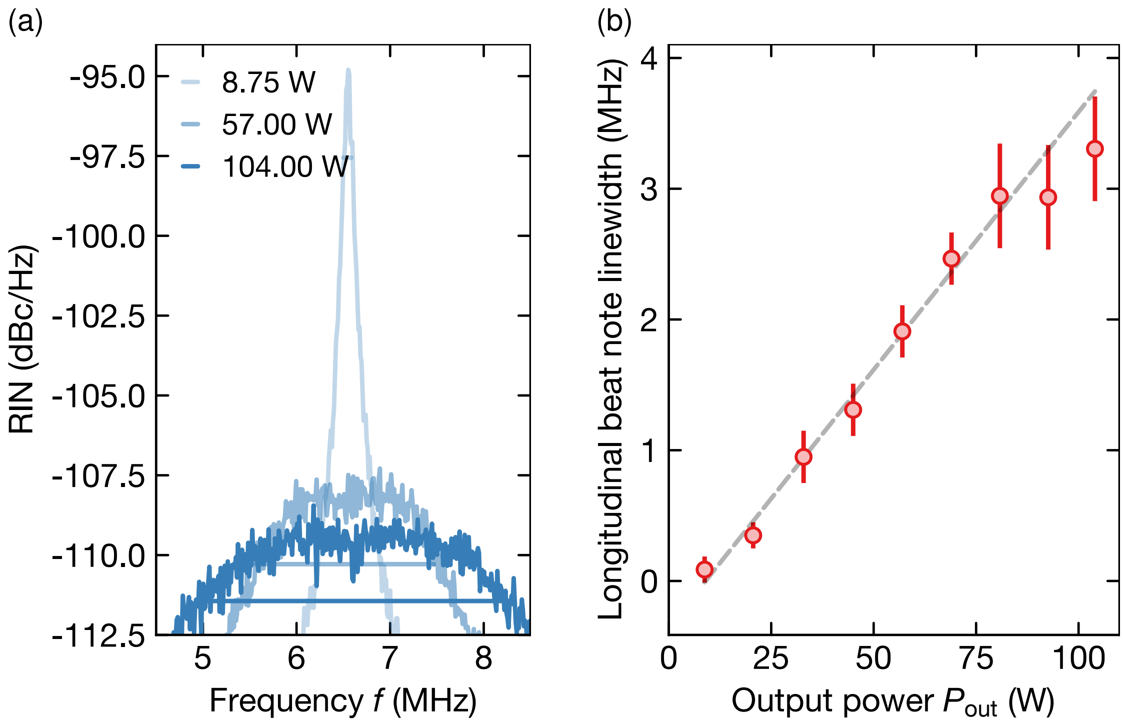

Figure 3.5 | Linewidth broadening of the first beat note peak for different output powers P_{out}. (a) The FWHM linewidth (blue colored horizontal lines) of the first beat note peak (see Fig. 3.3) increases with the output power of the laser. The output power was changed from 8.57 W (light blue) to 104 W (dark blue) in steps of 10% at the output level of the laser. (b) The beat note linewidth is shown for different output powers and shows approximately linear behavior (gray dashed line). Error bars indicate the noise-contingent uncertainty in the determination of the linewidth from the data.

in Fig. 3.1b and Fig. 3.4.

From Fig. 3.3, we can also determine that the total integrated normalized noise P/P_{dc} is $1.9 \cdot 10^{-9}$ for 8.75 W and $2.8 \cdot 10^{-8}$ for 104 W.

In conclusion, to determine the optimal running power of the laser, one has to balance the sharp peaks in the RIN at low power against the order of magnitude higher noise for high power.

In the next Chapter, we proceed with explaining the scanning system of the transport laser with shape and amplitude control.

4 Acousto-optic deflection and scanning system

After we investigated the characteristics dipole trap laser in the preceding Chapter, we now describe how to manipulate this laser via acousto-optics such that it generates not a circular but an elliptical beam.

For this, we first explore the acousto-optic effect in Sec. 4.1, starting with a simplified wave interaction picture and subsequently study it in a more extensive beam interaction picture. In Sec. 4.2, we explain, how we operate the acousto-optic devices, that we use in the setup. In Sec. 4.3, we use the knowledge of the preceding Section to compare the used acousto-optic devices, namely an acousto-optic modulator (AOM) and an acousto-optic deflector (AOD). In Sec. 4.4, we finally explain the scanning system for the laser and how to use it for generating time-averaged potentials.

4.1 Acousto-optic effect

For the subsequent Sections, it is essential to understand the general principles of acousto-optic interaction, explained in this part.

First, consider an *acoustic plane wave* created by a piezoelectric transducer, traveling in the x direction in an optically transparent medium of refractive index n, with wavevector $\mathbf{q}$, velocity of sound v_s, and acoustic frequency F, depicted in Fig. 4.1.

The acoustic wave is equivalent to a sinusoidal strain in the medium. This strain directly corresponds to a sinusoidal variation of the mediums refractive index $n(x,t) = n - \Delta n \cos(\Omega t - qx)$, where Δn is the amplitude of the perturbation, $\Omega = 2\pi F$ is the angular frequency and $q = 2\pi/\Lambda$ is the wavenumber with wavelength $\Lambda = v_s/F$. The minus sign shows that positive strain causes a reduction in the refractive index.

Furthermore, consider an *optical plane wave* entering this medium with wavevector $\mathbf{k}$,

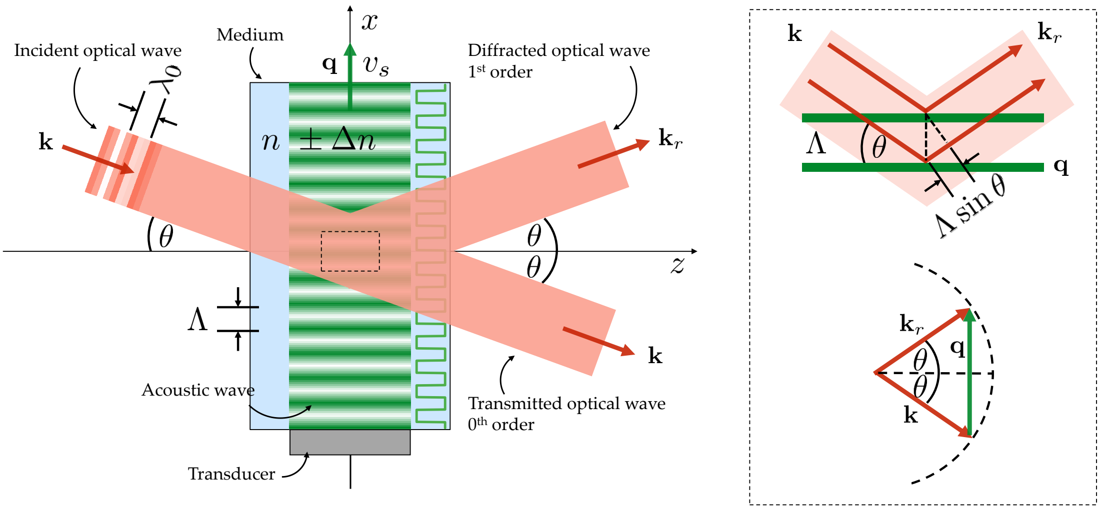

Figure 4.1 | Interaction of an optical wave with an acoustic wave. (*left*) An acoustic plane wave of wavelength Λ and wavevector $\mathbf{q}$ (green) generated by a piezoelectric transducer creates a varying refractive index $n \pm \Delta n$ in an optically transparent medium (blue). The refractive index variation is approximated as a static step function (green solid line), defining a set of parallel planes. An optical plane wave with free-space wavelength λ_0 and wavevector $\mathbf{k}$, incident at an angle θ is partially diffracted at every plane (dashed box). Consequently, a transmitted and diffracted optical wave with wavevectors $\mathbf{k}$ and $\mathbf{k}_r$, respectively, at the same angle $\pm\theta$ are generated. (*upper right*) The geometric relations relevant for Bragg diffraction of an optical wave represented by rays (red) at planes of varying refractive index (green) are shown. (*lower right*) The equivalent vector relations relevant for Bragg diffraction of an optical wave from an acoustic wave are shown. (adapted from Saleh and Teich [28])

frequency ν, free-space wavelength $\lambda_0 = c_0/\nu$, in-medium wavelength $\lambda = \lambda_0/n$, and wavenumber $k = 2\pi/\lambda$ incident at an angle θ relative to the z axis. Since in our setup the optical frequency $\nu \sim 300\,\mathrm{THz}$ is much greater than the acoustic frequency $F \sim 100\,\mathrm{MHz}$ (in the radio frequency (RF) range), we assume a static "frozen" refractive index n. We can thus replace the time-varying phase Ωt with a fixed φ. This incident optical wave is diffracted at every variation of the refractive index. To determine the total reflected optical wave, we first approximate the static sinusoidal variation of the refractive index as a step function. We thus obtain a set of parallel planes that act as partial reflectors. The resulting reflected optical wave is the sum of all partial reflections and generally composed of an upshifted and downshifted wave in frequency space, called the $+1^{\text{st}}$ order and the -1^{st} order. Here, we concentrate on the $+1^{\text{st}}$ order and call it 1^{st} order, the -1^{st} order can be treated in an analogous way. The transmitted optical wave is called the 0^{th} order.

The diffraction efficiency η is defined as the ratio of the optical power of the 1^{st} order P_1 and the total optical power P_{tot} after the acousto-optic device [35]:

$$\eta \equiv \frac{P_1}{P_{\text{tot}}}. \tag{4.1}$$

The maximum efficiency is reached for an angle of incidence where all the partial reflections from the planes interfere constructively. This condition is realized if the optical path difference inside the medium between two planes $2\Lambda \sin\theta$ is equal to the optical wavelength in the medium λ. This defines the *Bragg angle inside of the medium* θ_b, the *Bragg angle outside of the medium* θ_B and the *Bragg condition* (see Fig. 4.1):

$$\begin{aligned} \sin\theta_b \approx \theta_b &= \frac{\lambda}{2\Lambda} = \frac{\lambda_0 F}{2nv_s}, \quad \text{for} \quad \theta_B \ll 1, \\ \theta_B &= \frac{\lambda_0 F}{2v_s}. \end{aligned} \tag{4.2}$$

The same Bragg condition can also be stated as a vector relation $\mathbf{k}_r = \mathbf{k} + \mathbf{q}$, see Fig. 4.1) Eq. (4.2) creates the impression that the maximum efficiency can be reached for any angle θ by simply adjusting the acoustic frequency F. In reality, the acoustic-optic device has an optimal operating frequency called the *center frequency* F_c. This is due to the particular piezoelectric transducer and its tank circuit. As a result, we obtain one *true Bragg condition*:

$$\begin{aligned} \sin\theta_b \approx \theta_b &= \frac{\lambda_0 F_c}{2nv_s}, \\ \theta_B &= \frac{\lambda_0 F}{2v_s}. \end{aligned} \tag{4.3}$$

If one were to align the angle of incidence θ of the acousto-optic device at frequency F_c and one would than proceed to vary the acoustic frequency F, one would still see a 1$^{\text{st}}$ order beam. In fact, the *RF bandwidth* BW of an acousto-optic device is defined as the width around the center frequency $F_c \pm \text{BW}/2$ that results in half of the maximum diffraction efficiency.

If we want to be able to explain why there is light despite violating Eq. (4.3), *i.e.*, how the diffraction efficiency behaves when the Bragg condition is not met, we have to extend our simplified *plane wave* picture. We now consider *beams* that accurately describe light generated by a laser or sound generated by a transducer [28] as shown in Fig. 4.2.

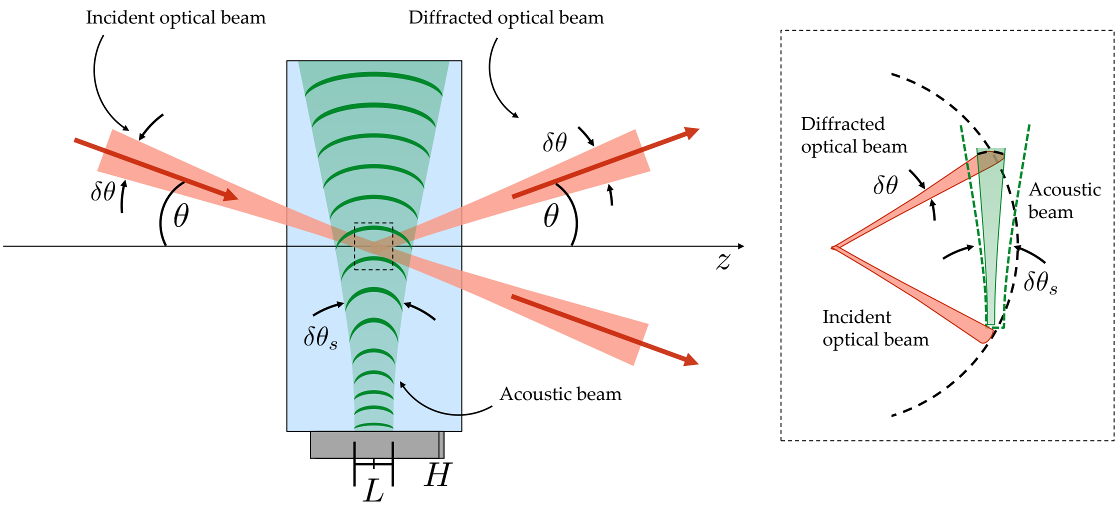

Figure 4.2 | Interaction of an optical beam with an acoustic beam. (*left*) An optical beam of angular divergence $\delta\theta$ incident at an angle θ interacts with an acoustic beam (green) of angular divergence $\delta\theta_s$ generated by a piezoelectric transducer (gray) of length L and height H. The diffracted optical beam has the same angle and divergence as the incident one. (*right*) The geometric relations relevant for Bragg diffraction of an optical beam (red) of an acoustic beam (green dashed lines) are shown. The incoming optical beam selects only part of the acoustic beam (filled green area) with wavevectors $\mathbf{q}_i$ that fulfill the Bragg condition for the optical wavevectors $\mathbf{k}_i$. (adapted from Saleh and Teich [28])

According to Fourier optics, beams are just a superposition of plane waves with wavevectors $\mathbf{k}_i$ for optical, and $\mathbf{q}_i$ for acoustic beams, respectively [28]. Their central directions occupy a cone of angular divergence [28, 36]

$$\begin{aligned} \delta\theta &\simeq \frac{\lambda_0}{\pi w_0}, \\ \delta\theta_s &\simeq \frac{1}{2}\frac{\Lambda}{L}. \end{aligned} \tag{4.4}$$

In our initial discussion for waves we matched exactly one wavevector $\mathbf{k}$ of an optical plane wave with one wavevector $\mathbf{q}$ of an acoustic plane wave (see Eq. (4.2)) to obtain the maximum diffraction efficiency, actually necessary to see any diffraction at all. In analogy to the plane wave picture and assuming $\delta\theta_s \gg \delta\theta$, the efficiency for beams is optimized if every $\mathbf{k}_i$ finds a matching $\mathbf{q}_i$. This condition is best met if the central directions of the optical and the acoustic beam fulfill Eq. (4.2), because these directions coincide with most of the directions of the wavevectors $\mathbf{k}_i$ and $\mathbf{q}_i$. If we thus change the acoustic frequency to $F = F_c$ and adjust the angle of incidence of the optical beam relative to our acousto-optic device according to Eq. (4.3), we still obtain the maximum efficiency as in the plane wave picture. To answer our initial question why we still see light when Eq. (4.3) is not met, we leave the angle of incidence unchanged and only alter the acoustic frequency F. We thus change the acoustic wavevectors $\mathbf{q}_i$. This situation is shown in Fig. 4.3.

First of all, since the $\mathbf{k}_i$ stayed the same, we now have a different and smaller subset of $\mathbf{k}_i$ that interact with the $\mathbf{q}_i$ at an angle $\theta = \lambda_0/2v_sF$ relative to the z axis outside of the medium, according to Eq. (4.2). The optical beam is deflected by 2θ and we still see a diffracted 1$^{\text{st}}$ order beam, but now weaker.

Additionally, the 1$^{\text{st}}$ order has shifted according to Eq. (4.2) and Eq. (4.3) by an angle $\beta \equiv \lambda_0(F_c - F)/v_s$ outside of the medium, compared to its direction for $F = F_c$. We define α as the angle between the central direction of the acoustic beam (its energy flow) and the bisector of the incident and 1$^{\text{st}}$ order beam and call this the *Bragg angle error*, Because only the 1$^{\text{st}}$ order has shifted relative to the acoustic beam direction and the 0$^{\text{th}}$ order remained at its initial position, we obtain a Bragg angle error of $\alpha = \beta/2$ outside of the medium and $\alpha = \beta/(2n)$ inside of the medium. The total deflection of the 1$^{\text{st}}$ order beam outside of the medium relative to the incident optical beam is, as mentioned before, 2θ, which defines the *scan angle* $\Delta\theta$:

$$\Delta\theta = 2\theta \cdot \frac{\mathrm{BW}}{F_c} = \frac{\lambda_0 \cdot \mathrm{BW}}{v_s}. \tag{4.5}$$

For later discussion, it is convenient to define a *characteristic interaction length* L_0:

$$L_0 \equiv \frac{n}{\lambda_0}\left(\frac{v_s}{F_c}\right)^2 \tag{4.6}$$

A detailed analysis shows that in this case the diffraction efficiency is given by [28, 36]

$$\eta = \rho \cdot \underbrace{\sin^2\left(\frac{\pi}{2}\sqrt{\frac{2LMP_a}{\lambda_0^2 H}}\right)}_{\eta_P} \cdot \underbrace{\operatorname{sinc}^2\left(\frac{\pi L \alpha}{\Lambda}\right)}_{\eta_F}, \tag{4.7}$$

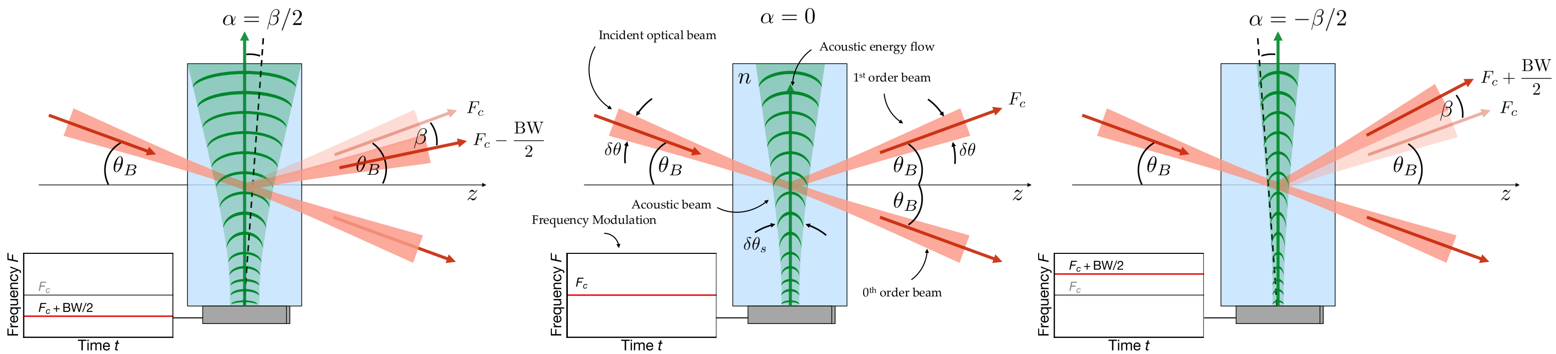

Figure 4.3 | Interaction of an optical beam with an acoustic beam of varying divergence. An acoustic beam (green) with divergence $\delta\theta_s$ is generated by a transducer. The acoustic beam interacts with an optical beam of divergence $\delta\theta$, incident at the Bragg angle $\theta = \theta_B$. The angle of deflection for the 0^{th} order is always θ_B while the angle θ of the 1^{st} order changes with acoustic frequency. (*middle*) The acoustic beam has frequency F_c and the 1^{st} order beam is deflected by an angle $\theta = \theta_B$ outside of the medium. The Bragg angle error α vanishes. (*left*) The acoustic beam has frequency $F_c - \mathrm{BW}/2$ and 1^{st} order beam is deflected by the angle $\theta = \theta_B - \beta$ outside of the medium. As a consequence, the Bragg angle error α is $\beta/2$. Also, the acoustic beam divergence $\delta\theta_s$ increases. (*right*) The acoustic beam has frequency $F_c + \mathrm{BW}/2$ and 1^{st} order beam is deflected by an angle $\theta = \theta_B + \beta$ outside of the medium. As a consequence, the Bragg angle error α is $-\beta/2$. Here, the acoustic beam divergence $\delta\theta_s$ decreases.

where ρ is a nonlinear function mainly dependent on beam divergences, M is the figure of merit – a material parameter describing the strength of the acousto-optic effect in the material, and P_a is the acoustic power transformed from the electric RF power P_{RF} by the lossy transducer. Here, we assume full conversion and use both terms interchangeably. The factors in Eq. (4.7) are the following:

1. ρ is the amplitude and a nonlinear function proportional to $\delta\theta_s/\delta\theta$.

2. η_P defines the dependence of the diffraction efficiency on the acoustic power P_{RF}. The optimal acoustic power for the maximum efficiency is given by $P_{\mathrm{a}}^{\mathrm{sat}} = \frac{\lambda_0^2 H}{2LM}$. This is the main application of *acousto-optic modulators*, varying the intensity of the diffracted light via the acoustic power.

3. η_F defines the dependence of the diffraction efficiency on the acoustic frequency. This is the main application of *acousto-optic deflectors* that vary the outcoming angle of the diffracted light via the acoustic frequency.

We describe the difference between a modulator and a deflector after the next Section.

4.2 RF Setup

Before we apply the expression derived in Sec. 4.1 to our acousto-optic devices, we briefly explain how we actually vary acoustic frequency or power in practice using the electronic setup shown in Fig. 4.4.

The RF driver box (engineered by Karsten Förster, *V7.1*) used in the experiment can be externally controlled by two signals: an amplitude modulation (AM) signal, ranging between 0 – 6 V and a frequency modulation (FM) signal, ranging between 0 – 10 V. The FM signal is fed to a voltage-controlled oscillator (VCO, Minicircuits, *POS-150*). The output signal of the VCO is successively combined with the amplitude modulation in a mixer. The resulting signal is

$$u(t) = \mathrm{AM}(t) \cdot \sin\left[k_{\mathrm{VCO}} \cdot \mathrm{FM}(t) + \varphi\right], \tag{4.8}$$

where k_{VCO} is the linear voltage-to-frequency conversion factor of the VCO (see App. C on page 93 for the calibration curves of the used RF drivers) and φ is a random phase.

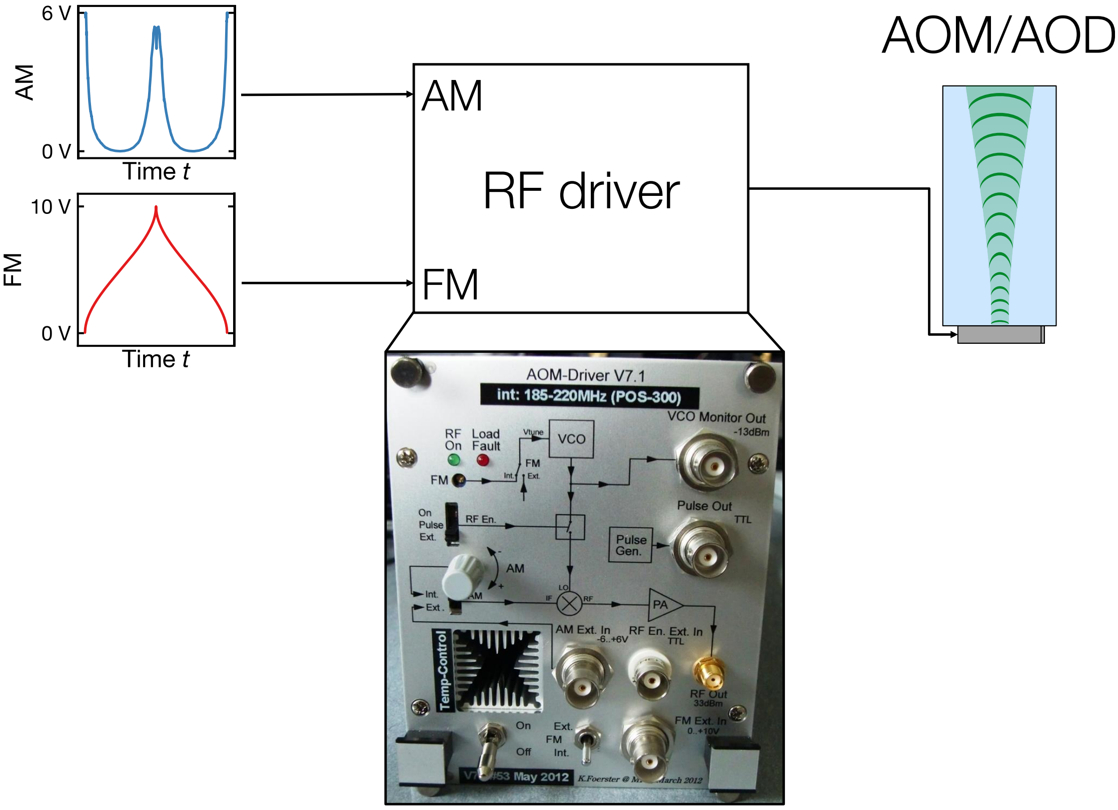

Figure 4.4 | Simplified electronic setup to control the acousto-optic devices. The RF driver (schematic and sample picture) used in the experiment has two signal inputs consisting of an amplitude modulation (AM) between 0 – 6 V and a frequency modulation (FM) between 0 – 10 V controlling a voltage-controlled oscillator (VCO, Minicircuits, *POS-150*). The input signals shown are later used in the experiment, but not to scale. The FM signal is send to the VCO and its out is combined with the amplitude modulation in a mixer, resulting in a signal $u(t) = \mathrm{AM}(t) \cdot \sin\left[k_{\mathrm{VCO}} \cdot \mathrm{FM}(t) + \varphi\right]$, where k_{VCO} is the conversion factor of the VCO and φ is a random phase. This combined signal is sent to the transducer of the AOM/AOD and controls the frequency and power of the resulting acoustic beam.

This combined signal is sent to the piezoelectric transducer of the AOM/AOD and thus controls the frequency and power of the resulting acoustic beam.

4.3 Comparison: AOM and AOD

We can now compare the diffraction efficiency η and the scan angle $\Delta\theta$ of the used acousto-optic devices, namely the AOM (Gooch & Housego, *AOMO 3080-198*) and AOD (Gooch & Housego, *AODF 4090-6*). This analysis will be very useful for the following Sections, *e.g.*, when we want to counteract efficiency losses while tuning the acoustic frequency by simultaneously tuning the acoustic power. For convenience, all key figures for both devices are summarized in Table 4.1.

Table 4.1 | Key figures for AOM and AOD. The data without errors was taken from [37–39] or has smaller errors than significant digits. The remaining data was obtained from the fits of Fig. 4.5, Fig. 4.6 and Fig. 4.7.

	AOM	AOD		AOM	AOD
Material	TeO_2	TeO_2	$P_{\mathrm{RF}}^{\mathrm{max}}$ (W)	3.0	1.5
Acoustic mode	Longitudinal	Shear, off axis	Active ap. (mm^2)	2 × 1.75	2 × 2
w_0 (mm)	0.79	0.47	η_{max}	0.97	0.86
$\delta\theta_s$ (mrad)	1.12	3.06	$\delta\theta$ (mrad)	0.19	0.3
L (mm)	24.1(6)	1.1	L_0 (mm)	6.2	0.1
M ($10^{-15}\mathrm{m}^2/\mathrm{W}$)	34.5	660	v_s (mm/µs)	4.2	0.656
H (mm)	3.1	1.9	$\Delta\theta$ (mrad)	6.4(2)	26.3(8)
F_c (MHz)	77.7(2)	89.8(2)	BW (MHz)	25.2(8)	16.1(5)

For the subsequent analysis we assume a mean refractive index of $n = 2.26$ for both devices, which corresponds to the material TeO_2. This implies that we restrict ourselves to an isotropic discussion and we say that anisotropic interactions, like in a shear-mode device, only leads to a reduction of the acoustic velocity.

The beam is collimated after several attenuators at the position of the AOD by a 3:1 telescope with lenses of focal lengths 300 mm (Thorlabs, *LA4579-C-ML*) and 100 mm (Thorlabs, *LA4380-YAG-ML*), having a waist $w_0 = 0.47$ mm (see Table 4.2). The angular movement of the AOD will later be reproduced at the vertical breadboard (see Fig. A.1 and Fig. A.2a) by a $4f$ system consisting of two 500 mm lenses (Newport, *SPX055AR.33*, see Table 4.2).

Table 4.2 | Pictures of the beam at the AOD and as reproduced by a 4f system. The pictures were fitted with a 2D Gaussian function (solid lines mark the $1/e^2$ value) and their long and short axis waist sizes are denoted w_D and w_d, respectively.

Position	AOD	Reproduced 50 mm before first tunable lens
Picture	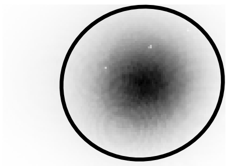	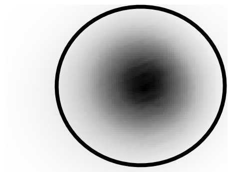
	$w_d = 0.43$ mm $w_D = 0.46$ mm	$w_d = 0.45$ mm $w_D = 0.48$ mm

For reaching the maximum efficiency of the AOD, it is crucial to set the correct horizontal p-polarization of the light with respect to the AOD's mounting plane. This requires a separate $\lambda/2$ waveplate before the AOD, since after the waveplate and Brewster plate combinations, the light is only *partially* p-polarized [28].

To measure the diffraction efficiencies as a function of RF power, we set the AOM and the AOD to their nominal center frequencies of 80 MHz and 90 MHz, respectively. We ramped the RF power with a waveform generator (Agilent, *33220A*) between the limits of 0 – 6 V of the AM input of the RF driver (Frequency 10 Hz) and record the optical power with a powermeter of sufficient bandwidth (Thorlabs, *PM100D* and sensor *S121C*). We converted the measured signals on an oscilloscope (Tektronikx, *TDS 2024C*) using the built-in scale of the powermeter V → mW for the optical power, and the calibration curves V → W for the RF power (see App. C on page 93). We determined the power of the 0^{th} order without applied RF power to be 148.8 mW for the AOM and 8.50 mW for the AOD (dashed line). The resulting diffraction efficiency η_P as a function of RF power is shown in Fig. 4.5.

We fit the data for the AOM and the AOD with the function η_P defined in Eq. (4.7) using only the height H of the acoustic transducer and absolute amplitude as free parameters, the other variables are taken from [37–39]. From the fit we obtain an electrode height of 3.1 mm for the AOM and 1.8 mm for the AOD. When compared to the active aperture of 2×1.75 mm^2 and 2×2 mm^2 for the AOM and AOD, respectively, both heights are reasonable. The maximum efficiency is 0.97 for the AOM and 0.86 for the AOD, in good agreement with their datasheets, and both show a saturation behavior as expected. By looking at the amplitude ρ in Eq. (4.7), we expect that for these high diffraction

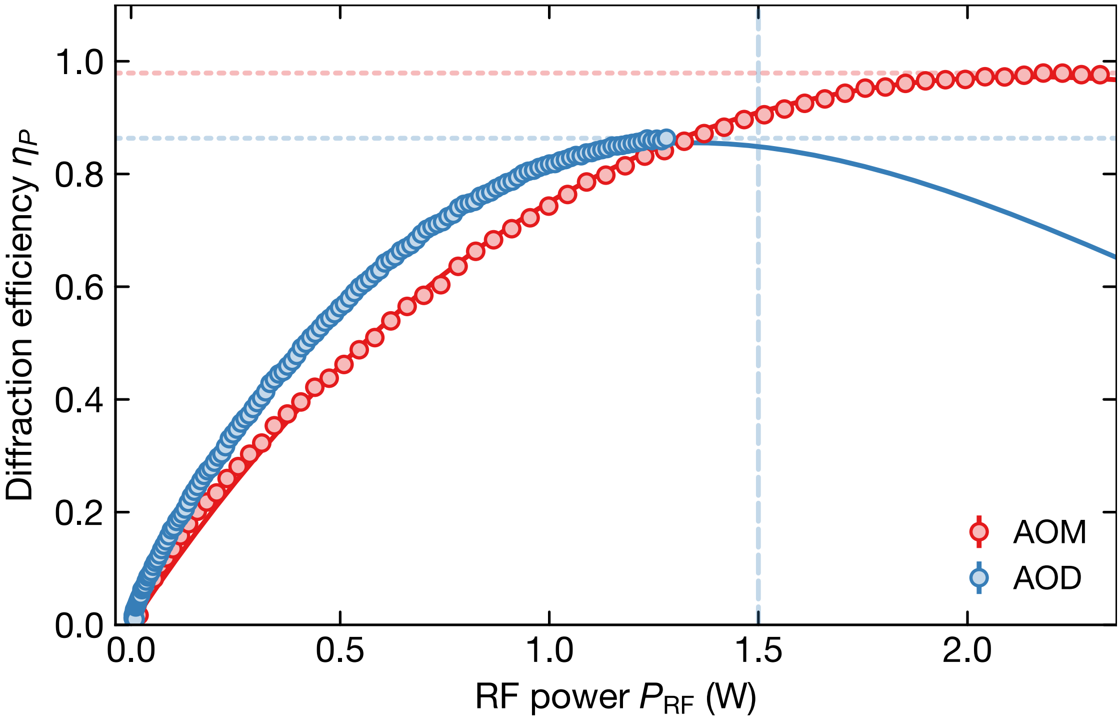

Figure 4.5 | Diffraction efficiency η_P as a function of RF power P_{RF}. The data for the AOM (red) and the AOD (blue) was fitted by η_P in Eq. (4.7) (solid lines) using only the height H and absolute amplitude as free parameters. The maximum efficiency (dotted lines) is 0.97 for the AOM and 0.86 for the AOD. The maximum RF power P_{RF} (dashed line) is 3 W for the AOM (not shown) and 1.5 W for the AOD. Both the AOM and AOD show a saturation behavior.

efficiencies the acoustic divergence $\delta\theta_s$ must exceed the optical divergence $\delta\theta$. Taking into account the beam sizes at the devices (see Table 4.1), and using Eq. (4.4), we obtain for the AOM $\delta\theta_s/\delta\theta \approx 6$ and for the AOD $\delta\theta_s/\delta\theta \approx 10$.

To measure the diffraction efficiencies as a function of acoustic frequency, we set the input RF power to the AOM and the AOD to 1 W and 1.4 W, respectively. Then, we ramp the acoustic frequency with the same waveform generator between the limits of 0 – 10 V of the FM input of the RF driver (Frequency 10 Hz) and record the optical power with the same powermeter as before. The absolute diffraction efficiency η is the product of both η_F and η_P (see Eq. (4.7)). Thus we can treat η_F independently of η_P and normalized it to its maximum value. The resulting normalized diffraction efficiency η_F as a function of acoustic frequency F is shown in Fig. 4.5.

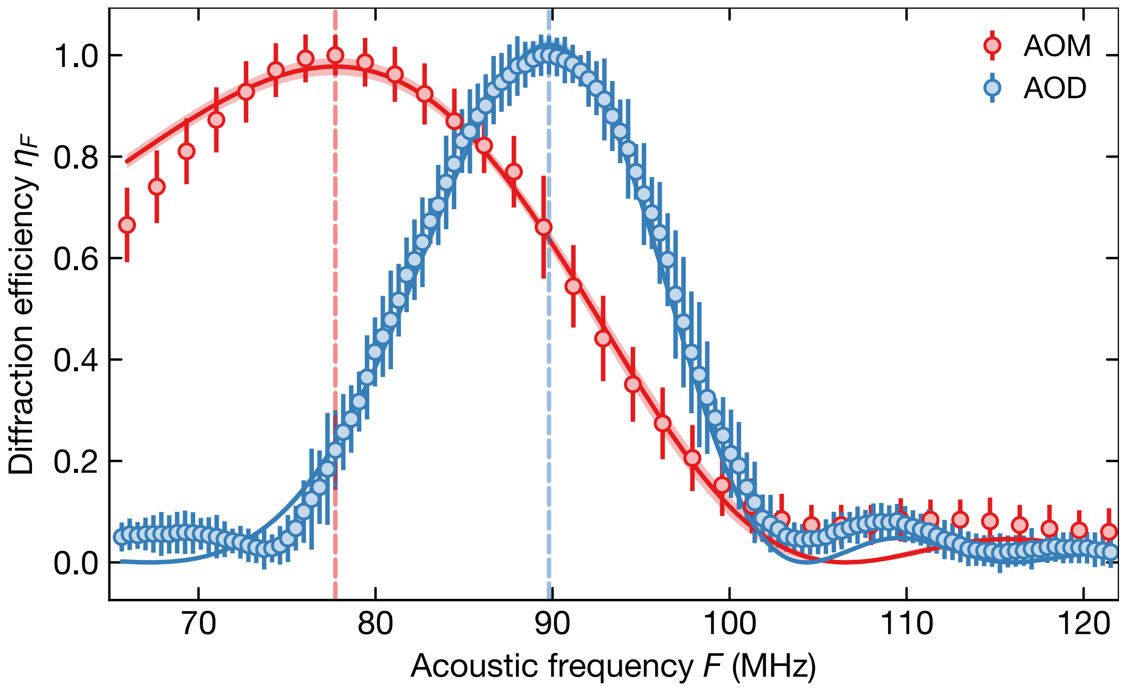

Figure 4.6 | Normalized diffraction efficiency η_F as a function of acoustic frequency F. The AOM has a center frequency $F_c = 77.7(2)$ MHz and an approximated FWHM bandwidth BW = 25.2(8) MHz, obtained by doubling the visible right half of the bandwidth. The AOD has a higher center frequency $F_c = 89.8(2)$ MHz and a smaller bandwidth BW = 16.1(5) MHz compared to the AOM. The data is fitted with η_F of Eq. (4.7) using Eq. (4.6). It is visible that the response curve of the AOD is slightly asymmetric around its center frequency. The accessible acoustic frequency is limited by the VCO. The error bars account for the limited resolution of the power meter and the oscilloscope.

The AOM has a center frequency $F_c = 77.7(2)$ MHz and an approximated FWHM bandwidth BW = 25.2(8) MHz, obtained by doubling the visible right half of the bandwidth. The center frequency is a little bit lower than the 80 MHz specified [38]. The bandwidth is in good agreement with the one given in the datasheet [38] of 20 MHz at −10 dB return loss. From the fit, using the calculated interaction length L_0 (see Eq. (4.6)), we also obtain a value for the length of the acoustic transducer electrode of 24.1(6) mm. Again, if we compare this value to the real dimensions of a typical AOM device it appears reasonable. The AOD has a higher center frequency $F_c = 89.8(2)$ MHz and a bandwidth BW = 16.1(5) MHz. The center frequency is very close to the 90 MHz specified in the datasheet [39] while the bandwidth is considerably lower than the nominal 35 MHz. To fix this discrepancy, the manufacturer suggested to align the AOD for maximum efficiency at the upper and lower limits of the bandwidth/scanning range. We could not verify this yet in the setup.

The data is fitted to the expression for η_F in Eq. (4.7). For the fit we reformulated η_F using the definitions of the interaction length L_0 (see Eq. (4.6)) and the Bragg angle error α, giving $\eta_F = \mathrm{sinc}^2(\pi/2L/L_0F/F_c(1-F/F_c))$ with only the electrode length L as free parameter. For the AOM, we thus obtain a ratio $L/L_0 \approx 4$ while for the AOD we obtain $L/L_0 \approx 11$, and thus a normalized interaction length nearly three times bigger. These ratios and the bandwidth of both devices are consistent with the theory curves given by Isomet [36]. They also go well with the fact that, the shorter the normalized interaction length, the less severe is a reduction of intensity due to misalignment (larger BW), and the higher is the required RF power for saturation (higher P_{RF}) similar to the AOM. It is also visible that the rolloff of the AOD is slightly asymmetric around its center frequency. This asymmetry in rolloff can be explained by a varying acoustic divergence $\delta\theta_s$ with acoustic frequency F, shown in Fig. 4.3. For acoustic frequencies $F < F_c$, the acoustic divergence is slightly larger than for F_c, and the incoming optical wavevectors $\mathbf{k}_i$ can interact with more acoustic wavevectors $\mathbf{q}_i$, yielding a higher intensity of the diffracted beam. For acoustic frequencies $F > F_c$, the situation is reversed because the acoustic divergence decreases.

Finally, we measure the relative reflectance angle, proportional to the scan angle $\Delta\theta$, as a function of acoustic frequency. We set the AOM and AOD to an RF power of 1 W and ramp again the acoustic frequency as described before. We then measure the position of the 0^{th} order, x_0, and the change in position x of the 1^{st} order with acoustic frequency using a translation stage and a beam profiler (Cinogy, *CMOS-1201-Nano*). We note the distance $\tilde{d}$ from the acousto-optic device to the beam profiler. From this distance and the lateral displacement $(x - x_0)$, we compute the diffraction angle $\theta \sim (x - x_0)/\tilde{d}$. The results are shown in Fig. 4.7.

The data has been offset-shifted for the different minimum diffraction angles of 12 mrad for the AOM and 101 mrad for the AOD. Linearly fitting the data according to Eq. (4.2),

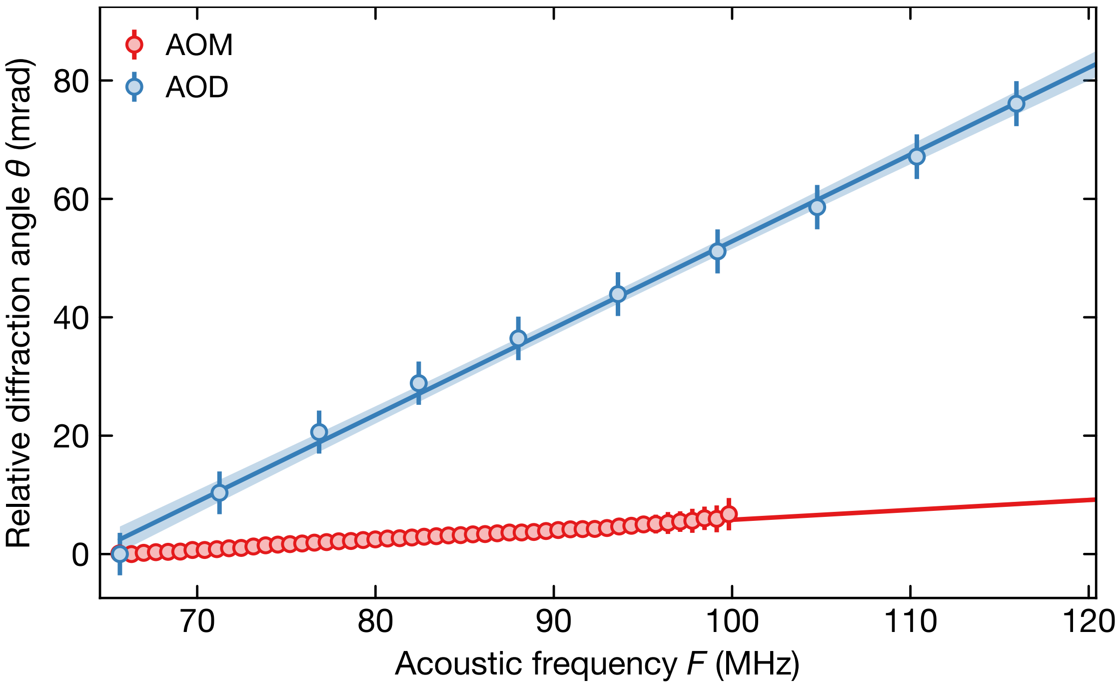

Figure 4.7 | Relative diffraction angle θ as a function of acoustic frequency F. The data has been offset-shifted for the different minimum diffraction angles of 12 mrad for the AOM and 101 mrad for the AOD. The solid lines are linear fits to the data and agree with the linear behavior of Eq. (4.2). The filled are indicates the 1σ confidence intervals of the fit. The AOM shows a much flatter response curve with a slope of 0.2 mrad/MHz as opposed to the AOD with 1.5 mrad/MHz. Error bars account for the uncertainty in the distance measurements.

we find a slope of 0.17(1) mrad/MHz for the AOM 1.5(1) mrad/MHz for the AOD. The 8.8 times larger slope of the AOD is mainly due to the ≈ 6.4 times slower acoustic velocity. This result emphasizes why AODs are preferable to AOMs when a light beam is to be diffracted over a large range of angles. A good measure for the accessible diffraction angles, *i.e.*, where the acoustic frequency is in the RF band, is the scan angle defined in Eq. (4.5). Taking into account the measured RF bandwidths of both devices we obtain a scan angle of 6.4(2) mrad for the AOM and 26.3(8) mrad for the AOD.

4.4 Scanning system and time-averaged potentials

After we discussed the theory of acousto-optic interaction and analyzed the AOM and AOD, we continue now by explaining the central ideas behind the scanning system.

It is possible to convert the angular displacement of the beam by the AOD into a parallel displacement using a lens at the right distance as shown in Fig. 4.8.

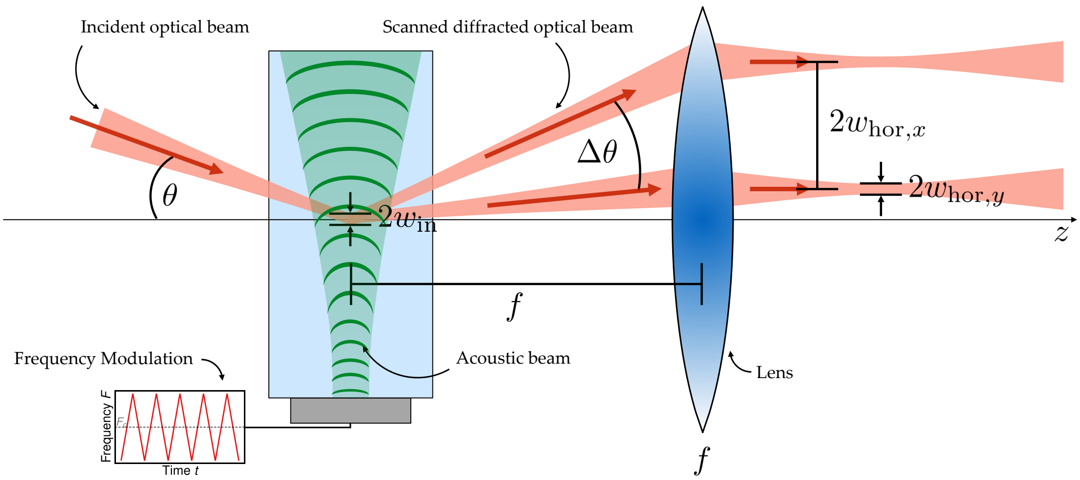

Figure 4.8 | Scanning system using AOD and lens. A diffracted beam is scanned over an angle $\Delta\theta$ by frequency modulating an AOD. This angular displacement can be fully converted into a parallel displacement to the optical axis by making use of a lens that is its focal length f away (elements not to scale). The resulting beam is elliptic and has a horizontal waist of $w_{\mathrm{hor},x}$ and a vertical waist of $w_{\mathrm{hor},y}$.

A Gaussian ABCD matrix calculation shows that this distance should be f, defining the *optimal scanning condition*:

$$\begin{pmatrix} 1 & d \\ -1/f & 1-d/f \end{pmatrix} \begin{pmatrix} 0 \\ \Delta\theta \end{pmatrix} \overset{d=f}{=} \begin{pmatrix} f\Delta\theta \\ 0 \end{pmatrix}. \tag{4.9}$$

Upon constantly scanning over the full scan angle, the resulting beam is elliptical with its long and short axes corresponding to the horizontal and vertical beam sizes $w_{\mathrm{hor},x}$ and $w_{\mathrm{hor},y}$. Combining $\tan(\Delta\theta/2) \approx \Delta\theta/2 = w_{\mathrm{hor},x}/f$ and Gaussian optics [28], we deduce:

$$\begin{aligned} w_{\mathrm{hor},x} &= \Delta\theta/2 \cdot f, \\ w_{\mathrm{hor},y} &= \frac{\lambda f}{\pi w_{\mathrm{in}}}. \end{aligned} \tag{4.10}$$

In combination both define a specific *aspect ratio*

$$\mathrm{AR} = \frac{w_{\mathrm{hor},x}}{w_{\mathrm{hor},y}} = \frac{\Delta\theta\pi w_{\mathrm{in}}}{2\lambda}. \tag{4.11}$$

Depending on the frequency modulation function, the actual intensity distribution can be tuned independently of the trap size as shown in Table 4.3.

Roy *et al.* [40] describe how to analytically calculate the frequency modulation function needed for a parabolic intensity shape, shown in the last picture of Table 4.3. This function assumes however a constant diffraction efficiency over the whole frequency range, which is clearly not the case (see Fig. 4.6). To counteract these efficiency variations, we also perform amplitude modulation (AM). As a first approach, based on Eq. (4.7), we define a minimum efficiency of $\eta/\rho = \text{const.} = 0.03$ and choose a scanning range of 35 MHz. This scanning range corresponds approximately to the frequency range between the first zeros of the diffraction efficiency in Fig. 4.6 of the AOD. These conditions now define the frequency-dependent part of the diffraction efficiency η_F. We then calculate the corresponding RF power-dependent part of the diffraction efficiency $\eta_P = \eta/(\rho\eta_F)$ to produce constant efficiency across the tuning range. Inverting the function $\eta_P(P_a)$, we obtain the desired RF power P_{RF} variation over one cycle. We can finally convert this RF power to the AM function using the calibration data of App. C on page 93. The resulting amplitude modulation function together with the frequency modulation function is also shown in the last picture of Table 4.3. Intuitively, the RF power is increased at the edges of the FM and lower in the center.

To benchmark the scanning system, an optional test point can be set up. It is located after the AOD, consisting of another mirror and a lens of focal length $f = 100\,\mathrm{mm}$ at

Table 4.3 | Normalized frequency modulation functions and resulting beam shapes. Depending on the frequency modulation (FM) function, one obtains different trap shapes. A square function produces two distinct points, a triangular function a straight uniform line and a sine function shows both features of distinct end points and uniform line. The last function is analytically calculated to give a parabolic intensity profile of the trap [40], looking very similar to an arccos function also used in previous experiments (see, *e.g.*, [41–43]). Also shown in the last picture is the additional amplitude modulation used to counteract trap imperfections through frequency-dependent efficiency losses of the AOD. Intuitively, the RF power is increased at the edges of the FM and lowered in the center. The pictures are not to scale.

FM function	Beam shape
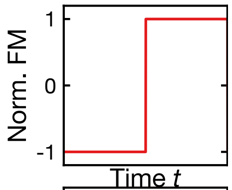	
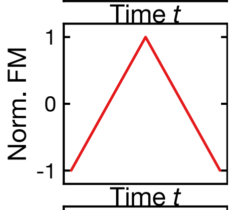	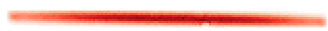
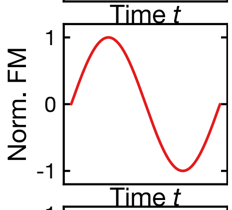	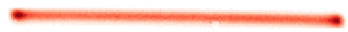
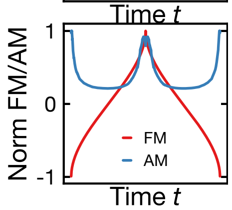	

a distance f from the AOD. We perform frequency modulation at 10 kHz. The data presented subsequently was not taken with the newer AM function shown in Table 4.3, but with an older one for a not polarization-optimized input beam to the AOD. The efficiency η_P saturated not at 0.86 but already at 0.6 and thus the tuning range was smaller. Nevertheless, no qualitative or substantial quantitative changes for the beam shapes are expected. The resulting beam profiles are shown once with amplitude modulation (see Fig. 4.9a) and without (see Fig. 4.9b).

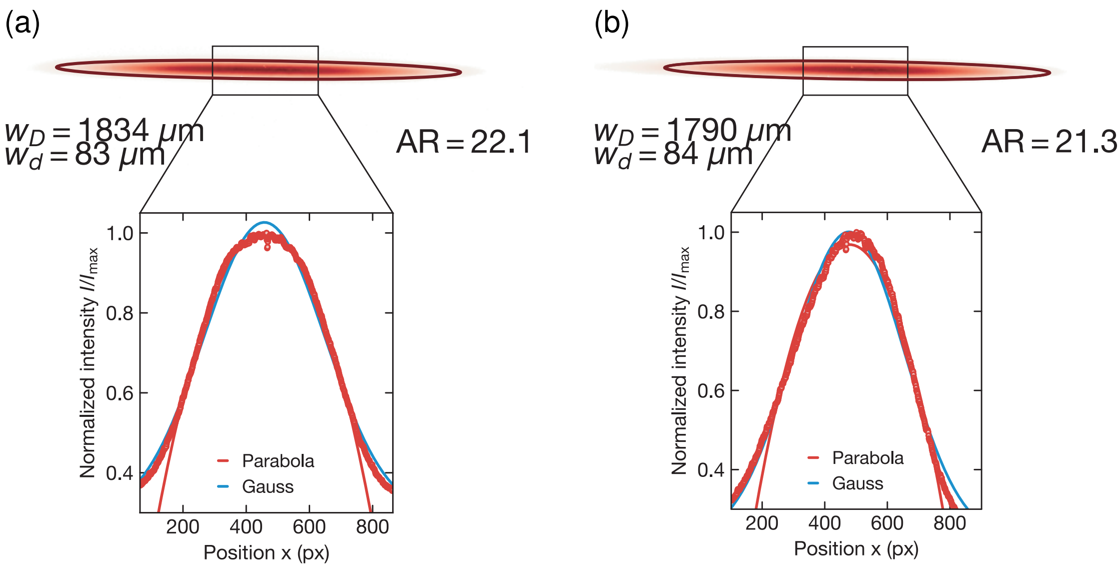

Figure 4.9 | FM trap shapes with and without AM. Pictures of the beam with FM, fitted with a 2D Gaussian (solid lines mark the $1/e^2$ value), and the intensity profile averaged over the vertical direction. This intensity profile is fitted with a parabola and a Gaussian. (*a*) The beam with AM has an AR of 22.1 and a more parabolic than Gaussian shape. (*b*) The beam without AM has a smaller AR of 21.3, is slightly asymmetric and shows no clear parabolic or Gaussian intensity profile.

Comparing the ARs 22.1 and 21.3 of the traps, we see that the trap size with amplitude modulation slightly exceeds the trap size without amplitude modulation. Furthermore, the amplitude modulation improves the trap intensity by “flattening” the diffraction efficiency curve as expected, favoring a parabolic intensity profile.

The fast can the sound frequency be modulated is determined by the input beam size and the crystal that has a particular speed of sound. The time to alter an optical beam roughly corresponds to the time it takes a wavefront of the acoustic beam to propagate across the whole optical beam of width $2w_{\text{in}}$. This determines the so-called *access time* and the corresponding *modulation bandwidth* (not to be confused with the RF bandwidth):

$$\begin{aligned} T &= \frac{2w_{\text{in}}}{v_s}, \\ \text{MBW} &= \frac{1}{T}. \end{aligned} \tag{4.12}$$

The modulation bandwidth is mainly limited by the used VCO in the AOM Driver, which has a 3 dB modulation bandwidth of 100 kHz. We found that up to 10 kHz, no distortions due to the limited modulation bandwidth are visible. Increasing the modulation frequency above that limit causes the VCO to not correctly follow the favored, custom FM waveform, *i.e.*, not reproducing the sharp maxima and minima. As a result, the trap starts to look more like in the sine modulation case shown in Table 4.3. If higher modulation frequencies are desired, *e.g.*, Baier [42] recommends the VCO model *VCO190-112T* from Varil. The *ratio of the modulation frequency to the trap frequencies* is the figure of merit that quantifies our degree of time-averaging. We calculate it after the next Chapter when we simulate the optical dipole trap.

We proceed, in the next Chapter, with explaining the telescopes of the transport laser with shape and amplitude control.

5 Dynamical beam shaping

In the last Chapter, we saw how to create an elliptical beam shape using an acousto-optic deflector. In this Chapter, we describe how we use *focus-tunable lenses* to perform dynamical beam shaping.

In Sec. 5.1, the general operation principle of the focus-tunable lenses is explained. In Sec. 5.2, we briefly show that the implemented telescopes do not affect the aspect ration of our elliptical beam.

5.1 Focus-tunable lenses

The focus-tunable lenses used in our setup can alter their focal length. They play an important role throughout the experiment, serving as means to tune beam sizes or enabling optical transport. For this reason, we explain their operation principle here, that is accompanied with certain limitations.

The layout of all tunable lenses we use in the setup is shown in Fig. 5.1.

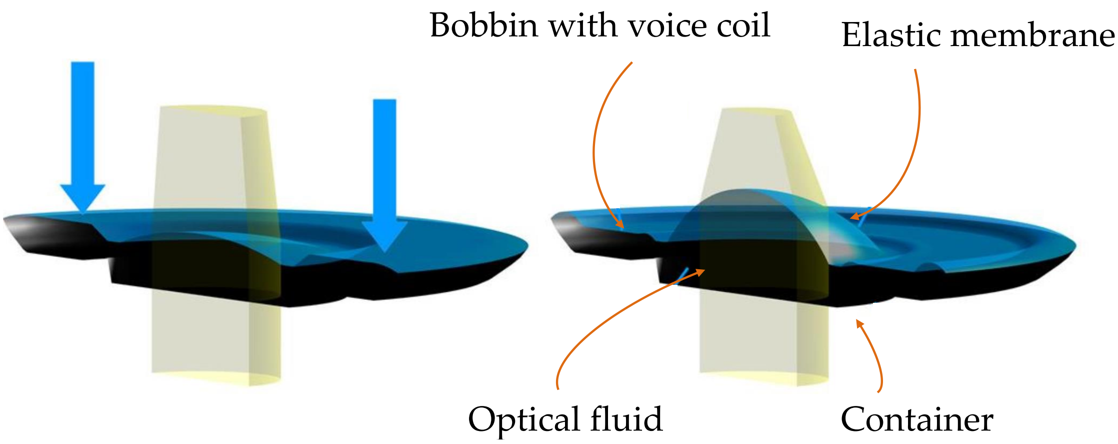

Figure 5.1 | Operating principle of the focus-tunable lenses. Inside the focus-tunable lens, an optical fluid is infolded by an elastic polymer membrane. An electromagnetic actuator, controlled by electrical current, can exert pressure on the container. As a result, the lens' curvature and therefore its focal length are changed. (adapted from Optotune [44])

Inside the tunable lens, an optical fluid is contained within an elastic polymer membrane. The focal length is changed using an electromagnetic actuator, controlled by an electrical current. The current is limited to 250 mA for all tunable lenses used in the setup [44]. This actuator can exert pressure on the container and change the lens' curvature and therefore its focal length. To conclude, we can control the focal length of the focus-tunable lens by current modulation.

We use a custom setup to drive this current through the lens coils. It is composed of a microcontroller (Arduino, *Leonardo ETH*) that controls a 12-bit digital-to-analog (DAC) converter chip (Microchip, *MCP4922*). This DAC, in turn, is connected to a current driver (Thorlabs, *LD1255R*), that converts a range of $0 - 5\,\mathrm{V}$ to a current range of $0.2 - 250\,\mathrm{mA}$.

Several things should be kept in mind when operating the focus-tunable lenses:

1. Upon mounting the lens in an upright position, *gravity* pulls the optical liquid inside the lens down and induces aberrations. Thus, operating the lenses with their horizontal axis parallel to the ground is recommended to minimize wavefront distortions.

2. *Larger beam sizes* on the order of the clear aperture of the lenses also cause optical aberrations. One should therefore use the smallest beam sizes possible.

3. *Correct alignment* is crucial for reducing shifts of the focus position in the image plane upon changing the focal length of the lens. To align the tunable lenses, we continuously ramp the current through them and observe the resulting beam

position at different distances in the image plane with a camera. When a movement of the beam center at different distances is not detectable on the camera anymore, the tunable lenses are correctly aligned.

4. *Temperature changes* also have an effect on the focal length of the lenses. If the current through the coil or a high-power laser beam heat up the lens, the focal length increases due to a decrease in refractive index of the optical fluid. At the same time, the optical fluid expands and decreases its focal length. The latter effect is the dominant one [44]. One way to correct for this, is feedforward control. By reading out the temperature of the lens through a built-in sensor, one can compute an interpolated calibration curve "focal length vs. current" from the two built-in calibration curves [45].

5.2 Effect of telescopes on the trap size

As evident from Eq. (4.11) and Eq. (4.5), the resulting aspect ratio of a scanned laser beam is only dependent on intrinsic properties of the laser, the AOD and the incident beam size. Telescopes, obeying the optimal scanning condition of Eq. (4.9), magnify w_{in} by M, and demagnify $\Delta\theta$ by M [28]. The resulting AR thus remains unchanged and we can tune the beam size without affecting the aspect ratio.

To dynamically tune the beam size of the optical dipole trap in our setup, we use two of the tunable lenses (Optotune, *EL-10-30-TC*), that can vary their focal length between 50 – 120 mm, in a telescope configuration (see Fig. 1.1). Regarding the aforementioned effects, the tunable lenses are mounted lying flat, and an additional fixed telescope of magnification 4 is used to achieve smaller beam sizes at the tunable telescope (see Fig. 1.1).

In the next Chapter, we proceed with describing in detail how we can form optical dipole traps with Gaussian beams.

6 Optical dipole trap with shape and amplitude control

Previously, we explored the theoretical background for optical trapping and cooling of strontium. We also looked at every individual element of the optical dipole trap setup, that enables shape and amplitude control. These elements were the laser, the acousto-optic deflector and the focus-tunable lenses. In this Chapter, we therefore combine all these components and analyze the performance of the setup.

We start by reviewing how a single Gaussian beam forms a dipole trap in Sec. 6.1. We then extend our discussion in Sec. 6.2 to combined, arbitrarily shaped Gaussian beams, forming a crossed dipole trap (XODT). This XODT represents our combined horizontal and vertical dipole trap. We thus continue with deducing the requirements of this XODT for the experiment and simulate its beam sizes in Sec. 6.3. Next, in Sec. 6.4, we realize the trap with our test setup and analyze its performance. Finally, in Sec. 6.5, we take realistic powers used for our crossed optical dipole trap and calculate its key parameters, namely the trap depths and trap frequencies.

6.1 Single circular and elliptical beams with gravity

In this Section, we continue our discussion of optical dipole traps with Gaussian beams from Sec. 2.4 and extend it.

First of all, we define a coordinate system inside our octagonal MOT chamber that we use from on and that is summarized in Fig. 6.1.

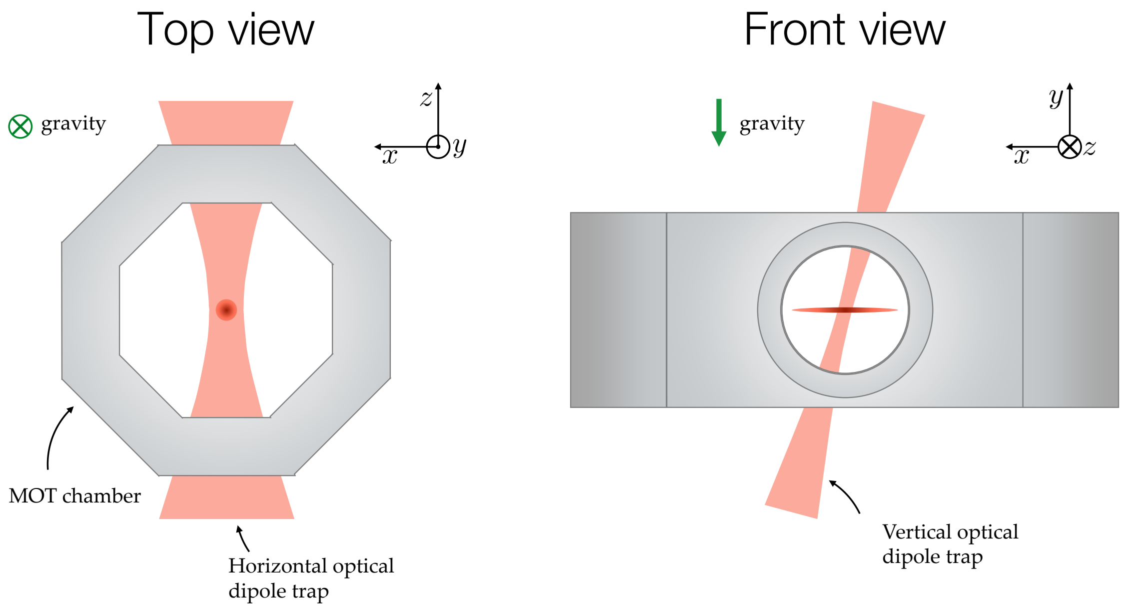

Figure 6.1 | Schematic view of the octagonal MOT chamber. (*left*) A top view of the octagonal MOT chamber (gray) shows the horizontal optical dipole trap which is elongated along the x direction. Also depicted is the vertical dipole trap (red dot). Gravity points into the $x-z$ plane. (*right*) A front view of the MOT chamber through the viewport for transport shows the vertical optical dipole trap. Also depicted is the elongated horizontal dipole trap (red ellipse). Gravity points downwards.

Consider an *elliptical Gaussian beam* that has the following intensity distribution [28]:

$$I(x,y,z) = \frac{2P}{\pi w_x(z) w_y(z)} \exp\left[-2\left(\frac{x^2}{w_x^2(z)} + \frac{y^2}{w_y^2(z)}\right)\right], \tag{6.1}$$

where P denotes the total power of the beam, $w_{x,y}(z) = w_{x/y,0}\sqrt{1+z/z_{R_{x,y}}}$ is the $1/e^2$ beam radius with Rayleigh range $z_{R_{x,y}} = \pi w_{x/y,0}^2/\lambda$ along the respective axis, minimal waist $w_{x/y,0}$, and vacuum wavelength $\lambda = \lambda_0$, and x, y, z are the coordinates specified in Fig. 6.1.

For small excursions, we can approximate the dipole potential defined in Eq. (2.10a) as a harmonic potential

$$V_{\text{dip}} \approx V_{\text{dip}}^{\text{harm}} = \sum_i \frac{1}{2}\frac{\partial^2 V_{\text{dip}}}{\partial x_i^2} x_i^2, \tag{6.2}$$

over all coordinates x_i. This harmonic approximation, together with the contribution from the gravitational potential mgy, gives us the *harmonic dipole potential for an elliptical*

Gaussian beam with gravity:

$$V_{\mathrm{ell}} \approx V_{\mathrm{ell}}^{\mathrm{harm}} = V_0 \left[1 - 2\left(\frac{x^2}{w_{x,0}^2} + \frac{y^2}{w_{y,0}^2} \right) - \frac{z^2}{z_{R_{\mathrm{eff}}}^2} \right] + mgy,$$
$$\omega_x = \sqrt{\frac{4V_0}{m w_{x,0}^2}}, \quad \omega_y = \sqrt{\frac{4V_0}{m w_{y,0}^2}}, \quad \omega_z = \sqrt{\frac{2V_0}{m z_{R_{\mathrm{eff}}}^2}}, \tag{6.3}$$

where we obtained the trap frequencies ω_i through comparison of the resulting potential with the harmonic potential $1/2 m \omega_i^2 x_i^2$. We also defined the *amplitude* V_0

$$V_0 = -\frac{1}{2\epsilon_0 c} \mathrm{Re}(\alpha) \cdot \frac{2P}{\pi w_{x,0} w_{y,0}}, \tag{6.4}$$

and an *effective Rayleigh range* $z_{R_{\mathrm{eff}}}$

$$z_{R_{\mathrm{eff}}} = \frac{z_{R_x} z_{R_y}}{\sqrt{\frac{1}{2}\left(z_{R_x}^2 + z_{R_y}^2 \right)}}. \tag{6.5}$$

We reproduce the already known case of a *circular Gaussian beam* (see Sec. 2.4) by taking $r^2 = x^2 + y^2$, $w_0 = w_{x,0} = w_{y,0}$ and $z_{R_{\mathrm{eff}}} = z_R$, giving the *harmonic dipole potential for a circular Gaussian beam with gravity*:

$$V_{\mathrm{circ}} \approx V_{\mathrm{circ}}^{\mathrm{harm}} = V_0 \left(1 - \frac{2r^2}{w_0^2} - \frac{z^2}{z_R^2} \right) + mgy \tag{6.6}$$

6.2 Crossed beams at 90° with gravity

Knowing the dipole potential for a single beam, we can also find the combined dipole potential of several beams. To keep the expressions simple, we restrict ourselves to the case of two elliptical Gaussian beams crossed at 90°. For including arbitrary angles, the reader is referred to Baier [42]. We denote the dipole potentials of our horizontal ODT by V_{hor} and our vertical ODT by V_{ver}. To deduce the dipole potential of our XODT, we simply add both horizontal and vertical potential, as well as the gravitational potential mgy while paying close attention to the geometry depicted in Fig. 6.1. A harmonic approximation of the resulting potential gives the *harmonic dipole potential for two crossed, elliptical*

Gaussian beams with gravity:

$$\begin{aligned} V_{\text{crossed}} \approx V_{\text{crossed}}^{\text{harm}} &= V_{\text{hor}}\left[1 - 2\left(\frac{x^2}{w_{\text{hor},x}^2} + \frac{y^2}{w_{\text{hor},y}^2}\right) - \frac{1}{2}\frac{z^2}{z_{R_{\text{hor,eff}}}^2}\right] \\ &+ V_{\text{ver}}\left[1 - 2\left(\frac{x^2}{w_{\text{ver},x}^2} + \frac{y^2}{w_{\text{ver},y}^2}\right) - \frac{1}{2}\frac{z^2}{z_{R_{\text{ver,eff}}}^2}\right] + mgy \\ \omega_x &= \sqrt{\frac{4}{m}\left(\frac{V_{\text{hor}}}{w_{\text{hor},x}^2} + \frac{V_{\text{ver}}}{w_{\text{ver},x}^2}\right)} \\ \omega_y &= \sqrt{\frac{1}{m}\left(\frac{4V_{\text{hor}}}{w_{\text{hor},y}^2} + \frac{2V_{\text{ver}}}{z_{R_{\text{ver,eff}}}^2}\right)} \\ \omega_z &= \sqrt{\frac{1}{m}\left(\frac{2V_{\text{hor}}}{z_{R_{\text{hor,eff}}}^2} + \frac{4V_{\text{ver}}}{w_{\text{ver},z}^2}\right)}, \end{aligned} \tag{6.7}$$

where $z_{R_{\text{hor/ver,eff}}}$ denotes the effective Rayleigh range of the horizontal or vertical dipole trap and $w_{\text{hor/ver},x_i}$ denotes their minimal waist along a specific axis.

With the knowledge of this Chapter, we are able to calculate trap depths and trap frequencies of various combinations of Gaussian beams. Before we do that, we deduce the requirements for our dipole trap, mainly the beam sizes, in the following Section.

6.3 Requirements

To infer the beam sizes for the horizontal and vertical dipole traps (HODT, VODT), we first think about the requirements for trapping the atoms. In the crossed dipole trap, the horizontal and vertical traps fulfill different purposes:

1. The HODT mainly *supports the atoms against gravity and sets the trap depth* through its beam waists w_{hor} and power P_{hor} (see Sec. 6.1). Therefore, it will be also used for evaporative cooling. Looking at Fig. 2.5a and Fig. 2.5b, we remember that the red MOT for strontium typically has an elliptical or even a "pancake" shape. To reach a high transfer efficiency from the red MOT into the HODT, we should thus mode-match both traps. This is the first reason why an elliptical HODT is preferable. During evaporation, atoms leave the trap predominantly in the vertical direction aided by gravity. Consider focusing the HODT tightly in the vertical y

direction, achieving a small vertical waist $w_{\mathrm{hor},y}$, while maintaining a elongated waist $w_{\mathrm{hor},x}$ in the horizontal x direction. By doing this, we generate a high trap frequency ω_y (see Eq. (6.3)) compared to the scattering rate. High-energy atoms produced in a collision are thus more likely to escape the trap vertically before colliding with other atoms and possibly removing them from the trap. This is the second reason why we need an elliptical HODT.

2. The VODT mainly *controls the density of the sample and confines the atoms to the horizontal plane*. It does not support them against gravity. Regarding evaporative cooling, we need a high rate of elastic collisions for thermalization of the sample, while maintaining low losses, *e.g.*, by three-body collisions [19]. It turns out that the density is the only parameter available to tune this ratio. We can tune the density via the waist w_{ver} and power P_{ver} of the vertical dipole trap. The best parameters are highly dependent on the isotope.

For convenience, we review a simplified version of the setup, engineered to meet those requirements, once more in Fig. 6.2. A complete sketch of the setup is shown in Fig. A.1 and Fig. A.2a.

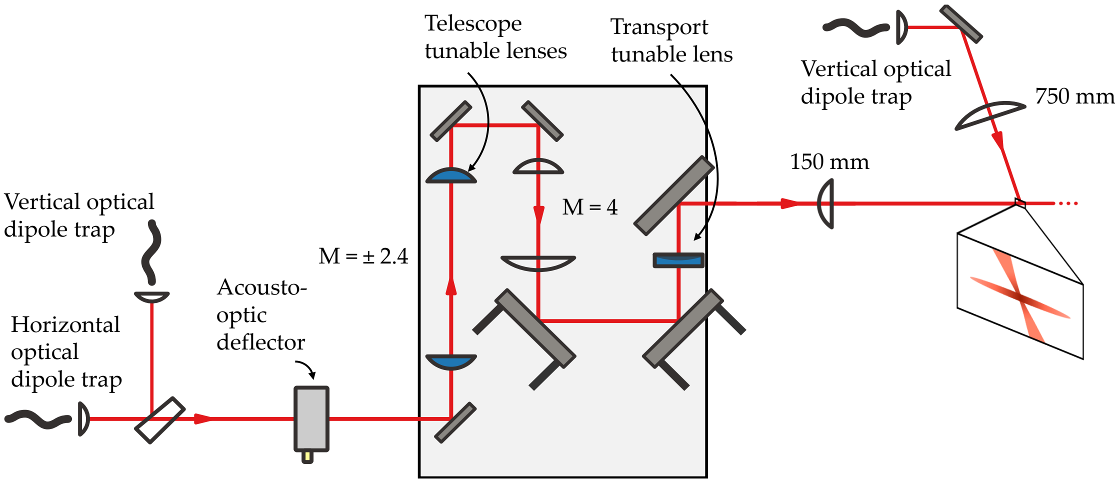

Figure 6.2 | Schematic overview of the setup for the optical dipole trap with shape and amplitude control. The HODT beam is first sent through an acousto-optic deflector. The beam is subsequently magnified on the vertical breadboard by the adjustable telescope with magnification $M = \pm 2.4$ and the fixed telescope with magnification $M = 4$. The transport tunable lens is idle at this stage. The HODT beam finally is focused onto the atoms with a lens of 150 mm focal length. The VODT beam is focused by a 750 mm lens.

In the setup, the HODT beam is first deflected by the acousto-optic deflector (Gooch & Housego, *AODF 4090-6*). The beam is then magnified by our adjustable telescope, consisting of two focus-tunable lenses (two Optotune *EL-10-30-TC*) to a magnification of 1.2. According to [44], both lenses are able to tune their focal length ranging from 50 – 120 mm. This range enables, in principle, a positive or negative magnification of 2.4. This magnification is once more increased by the fixed telescope of magnification 4 that uses a 20 mm (Optosigma, *HFTLSQ-15-20PF1*) and 80 mm lens (Lightpath Technologies, *GPX40-80*). The resulting beam is focused through the final lens with $f = 150\,\mathrm{mm}$ (Optosigma, *HFDLSQ-30-150PF1*).

For the VODT, we use a split-off from the main beam of the fiber laser. We plan to extend this beam to $w_0 = 4.4\,\mathrm{mm}$ and focus it onto the atoms by a 750 mm lens. This procedure would give us a waist of $w_{\mathrm{ver}} = 58\,\mu\mathrm{m}$ for the vertical optical dipole trap.

To show that this setup fulfills our requirements for the HODT, we simulated the backpropagation of different final beam waists $w_{\mathrm{hor},y}$ with an ABCD matrix calculation [32], giving us different input beam waists w_{in}. We finally chose a waist of $w_{\mathrm{hor},y} = 23\,\mu\mathrm{m}$, obtained with an input waist of $w_{\mathrm{in}} = 0.47\,\mathrm{mm}$. This input waist is a good compromise between the beam size for the AOD, recommended in the datasheet [39], the HODT requirements, and, as we see later, the optical transport. The results of the simulation are shown in Fig. 6.3.

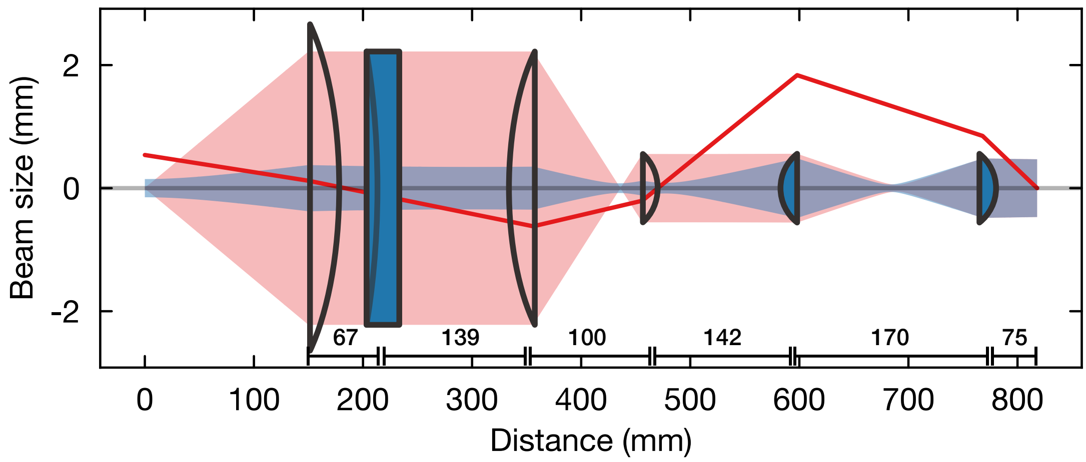

Figure 6.3 | ABCD matrix simulation of the HODT. The propagation of an input beam of waist $w_{\mathrm{in}} = 0.47\,\mathrm{mm}$ for the HODT (red filled area) is simulated through the setup shown in Fig. 6.2 using Gaussian ABCD matrices. The adjustable telescope has a magnification of 1.2. We obtain a final beam size of $w_{\mathrm{d}} = 23\,\mu\mathrm{m}$. Also shown is the deflection of the beam center by the AOD, simulated using ray ABCD matrices (red line). The setup is not perfectly fulfilling the optimal scanning condition of Eq. (4.9). In this case, all rays in between the telescopes and after the final would be parallel to the optical axis. Taking a scanning angle of $\theta = 53.5\,\mathrm{mrad}$, we obtain an elongated waist $w_{\mathrm{hor},x} = 541\,\mu\mathrm{m}$. Also shown is the reshaped beam of waist $w_{\mathrm{trans}} = 148\,\mu\mathrm{m}$, later used for the transport. It is generated by the same input waist and explained in the subsequent Chapter (blue filled area).

We simulate the propagation of an input beam of waist $w_{\mathrm{in}} = 0.47\,\mathrm{mm}$ for the HODT through the setup using Gaussian ABCD matrices. The adjustable telescope has in the simulation a magnification $M = 1.2$. Together with a fixed magnification $M = 4$ and a final lens with focal length 150 mm, we obtain a final beam size of $w_{\mathrm{d}} = 23\,\mathrm{\mu m}$. To simulate the elongated HODT for time-averaged potentials, we calculate the deflection of the beam center by the AOD using ray ABCD matrices. As can be seen from this trace, the setup is not perfectly fulfilling the optimal scanning condition of Eq. (4.9). In this case, all rays in between the telescopes and after the final would be parallel to the optical axis. If we assume a scanning angle of $\theta = 53.5\,\mathrm{mrad}$, we obtain an elongated waist of $w_{\mathrm{hor},x} = 541\,\mathrm{\mu m}$. In total, this gives us an aspect ratio of $AR = 23.5$.

6.4 Performance

After the simulation, we can proceed to realize the horizontal optical dipole trap in our test setup.

The test setup used is equivalent to the one we plan to install in the experiment, which is shown in completeness in Fig. A.1 and Fig. A.2a. To obtain the desired beam sizes, we iteratively varied the currents of the tunable lenses in the adjustable telescope and the position of the final lens. As a result, setting the currents to $i_0 = 250\,\mathrm{mA}$, the specified maximum through the lens coils, and $i_1 = 88\,\mathrm{mA}$ gave us the expected beam size. The resulting beam was recorded with a beam profiler and is shown in Fig. 6.4.

The resulting trap has a long axis waist $w_D = 541\,\mathrm{\mu m}$ and a short axis waist $w_d = 23\,\mathrm{\mu m}$, giving an aspect ration of AR ≈ 23.5, equal to the simulated one. Even higher AR are reached compared to the beams at the test point, which was 22.1 (see Fig. 4.9a) and presumably closer to the optimal scanning condition. This is not expected since we assumed from Fig. 6.3 that we would lose some of the scanning potential. Also, from the scanning range used of 35 MHz, we calculate a scanning angle of 52.5 mrad using the AOD slope of 1.5 mrad/MHz (see Fig. 4.7). This result only slightly deviates from the 53.5 mrad used in the simulation. The profile is again slightly asymmetric and shows no clear parabolic or Gaussian intensity profile. For the measurement, the amplitude and frequency modulation was left unchanged, compared to the optimization at the test point (see Sec. 4.4). However, we did reduce the attenuation at the last attenuator for easier alignment, which changed the polarization before the AOD. Since we did not optimize for polarization at the AOD again, the intensity profile slightly deviates from the optimum.

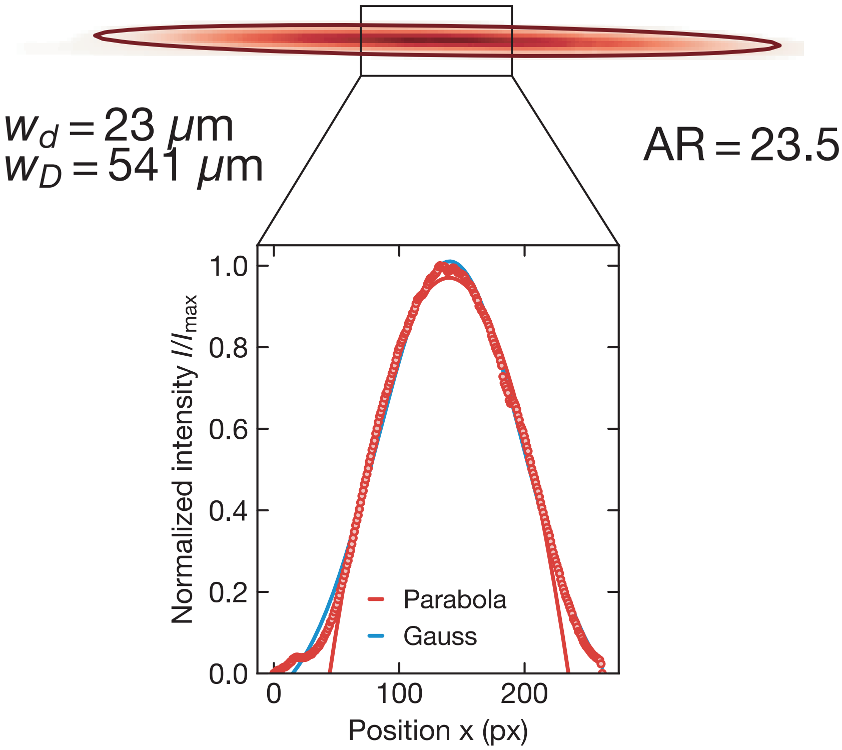

Figure 6.4 | Horizontal optical dipole trap. (*top*) The resulting trap is fitted with a 2D Gaussian (solid line marks the $1/e^2$ value). It has a long axis waist $w_D = 541\,\mu m$ and a short axis waist $w_d = 23\,\mu m$, giving an aspect ration of AR ≈ 23.5. (*bottom*) The intensity profile averaged over the vertical direction is shown. The profile is again slightly asymmetric and shows no clear parabolic or Gaussian intensity profile.

6.5 Trap potential and trap frequencies

Since we know the requirements of our optical dipole trap and tested its performance, we can calculate the trap potential and trap frequencies as outlined in Sec. 6.2.

We calculate the resulting crossed dipole trap potential for the HODT with waists $w_{\mathrm{hor},x} = 541\,\mu\mathrm{m}$ and $w_{\mathrm{hor},y} = 23\,\mu\mathrm{m}$, respectively, shown in Fig. 6.4, and our planned VODT with waist $w_{\mathrm{ver}} = 58\,\mu\mathrm{m}$. In this definition, we used the geometry shown in Fig. 6.1. To calculate the total potential, we use Eq. (6.1), Eq. (2.10a) and the mass of ^{87}Sr. We assume a typical power of $P_{\mathrm{ver}} = 100\,\mathrm{mW}$ for the VODT [19]. As before, we only consider the dominant blue MOT transition, effectively modeling strontium as a two-level system. The results are shown in Fig. 6.5.

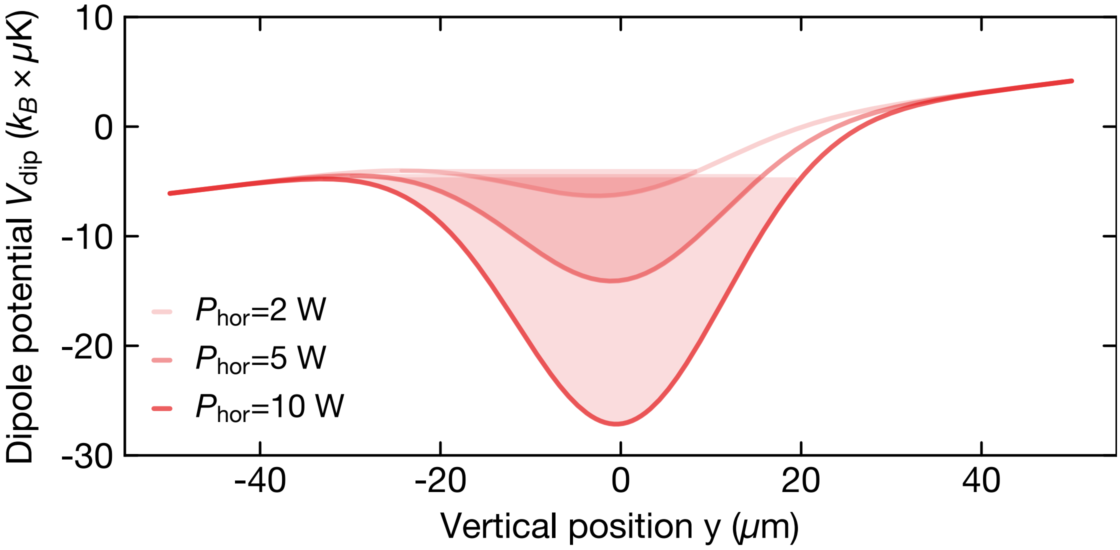

Figure 6.5 | Crossed dipole trap potential along the axis of gravity for different HODT powers. The crossed dipole trap potential was calculated according to Eq. (6.1) and Eq. (2.10a) using the geometry in Fig. 6.1. The beam sizes used for the HODT are the ones of Fig. 6.4. For the VODT we expect a waist of $w_{\mathrm{ver}} = 58\,\mu\mathrm{m}$. The power of the VODT is held constant at 100 mW while the power of the HODT is varied through 2 W (light red), 5 W (mid red) and 10 W (dark red) yielding trap depths of $k_B \times 2\,\mu\mathrm{K}$, $k_B \times 10\,\mu\mathrm{K}$ and $k_B \times 22\,\mu\mathrm{K}$ (colored filled areas).

Looking at the trap depths of Fig. 6.5, a minimum power of 5 W for the HODT seems reasonable, if we want to trap atoms with ~ 1 µK, produced in the red MOT. Changing the power of the VODT only affects the offset of the trap and does not change its depth. From the harmonic approximation (see Eq. (6.7)), we obtain the trap frequencies $\omega_x = 2\pi \times 57\,\mathrm{Hz}$ in the horizontal direction, $\omega_y = 2\pi \times 488\,\mathrm{Hz}$ along the axis of gravity and $\omega_z = 2\pi \times 53\,\mathrm{Hz}$ along the later axis of transport. Looking at the ratio of modulation frequency of 10 kHz and ω_x, we see that we modulate ~ 175 times faster than the trap frequency. Baier [42] reports, that already a factor of 100 along this axis is sufficient for the atoms to not heat up.

In conclusion, we are able to create sufficient sizes for the horizontal optical dipole trap. In addition, we are also able to modulate it fast enough, such that the atoms indeed experience a time-averaged potential.

We proceed with the optical transport in the next Chapter.

7 Optical transport

The next step, after trapping the atoms in the dipole trap and evaporatively cooling them, is the optical transport from the MOT to the science chamber, which is described in this Chapter.

In Sec. 7.1, we start by presenting the principles of optical transport. We also deduce the requirements of the transport for the experiment and simulate its beam sizes. In Sec. 7.2, we again realize the optical transport in our test setup and analyze its performance. Finally, In Sec. 7.3, we take realistic powers used for our transport trap and calculate the trap depths and trap frequencies. These are essential to know to achieve high transport efficiencies without heating, *e.g.*, choosing the right transport duration and power.

7.1 Theory and requirements

After capturing the atoms in the elliptical optical dipole trap, we reshape the beam to a circular waist of $w_{\text{trans}} = 148\,\mu\text{m}$. Suitable for transport, we consider an evaporative cooling step at this point [19]. Here, however, we concentrate on the subsequent optical transport.

For the transport, we again simulated the backpropagation of different final beam waists w_{trans} through the setup on the vertical breadboard (see Fig. 1.1) with an ABCD matrix calculation [32], giving us different input beam waists w_{in}. But as opposed to before, we start from a distance $\sim 100\,\text{cm}$ away from the initial position of the atoms, corresponding to the maximum planned transport distance. To understand how the transport works, we first discuss the lower part of Fig. 7.1.

As an example, let us choose a transport waist $w_{\text{trans}} = 148\,\mu\text{m}$ and a transport distance $z_{\text{trans}} = 100\,\text{cm}$, defined as the distance between the initial focus at atoms. The initial focus at the atoms is the zero in Fig. 7.1, and the focus after transport is 100 cm away along the negative axis.

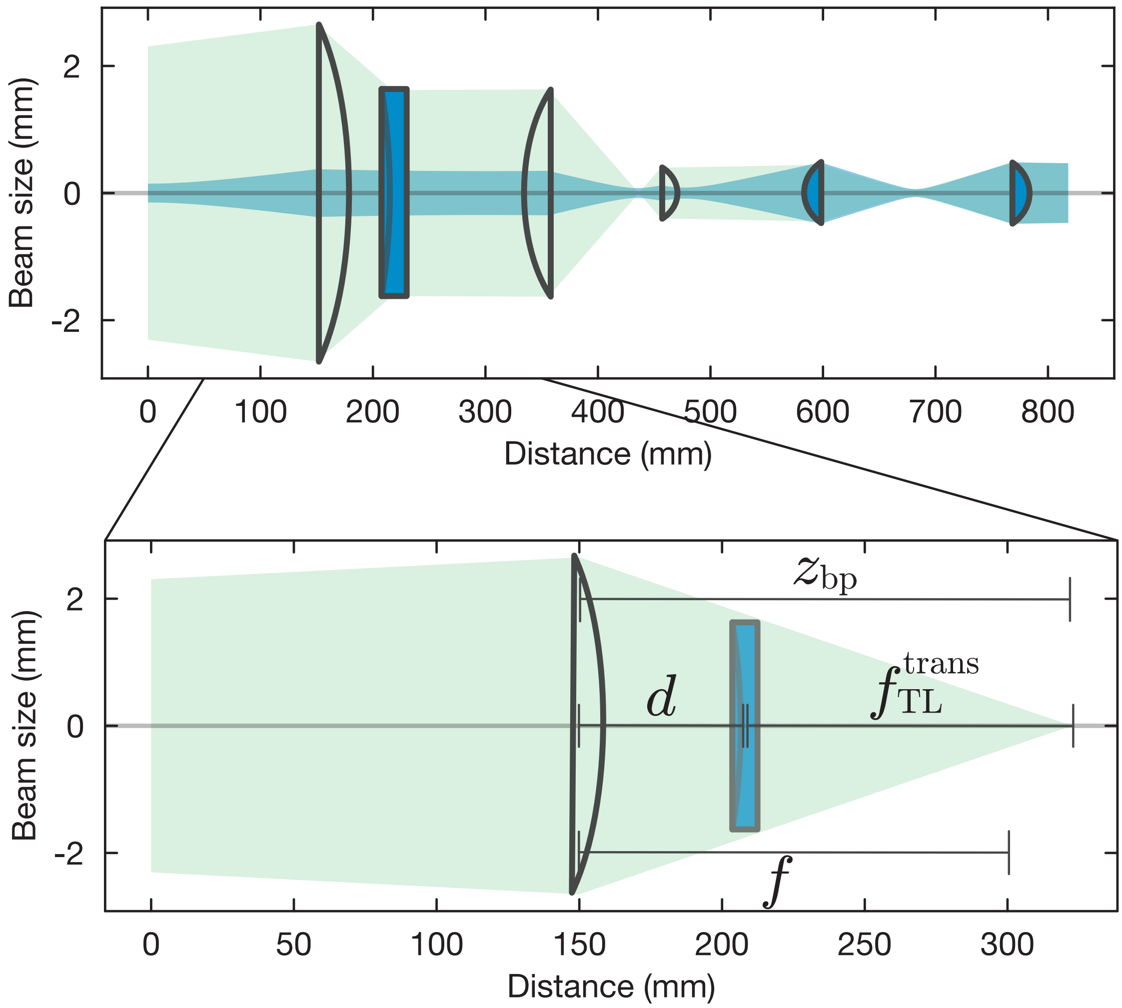

Figure 7.1 | ABCD matrix simulation of the optical transport. (*top*) The beams for the different configurations, circular (blue) and transport (green), were simulated with the optical setup using Gaussian ABCD matrix optics . All optical elements are at their real distances. Both configurations are simulated with the same input beam of $w = 0.47\,\mathrm{mm}$ and give the same output beam size $w_{\mathrm{trans}} = 148\,\mu\mathrm{m}$. The circular beam was simulated using $f_0 = 82\,\mathrm{mm}, f_1 = 51\,\mathrm{mm}$ and $f_2 \sim \infty$ for the tunable lenses from right to left. The transported beam was generated using $f_0 = 85\,\mathrm{mm}, f_1 = 77\,\mathrm{mm}$ and $f_2 = -105\,\mathrm{mm}$. (*bottom*) The cutout shows the transported beam backpropagated through the final lens f. The distance between the position of the focused beam and the final lens is called the distance of backpropagation z_{bp}. A diverging, tunable lens of focal length $f_{\mathrm{TL}}^{\mathrm{trans}}$ has to be placed somewhere between the final lens at distance d and the focus to achieve the transport (see text for details).

We can let this Gaussian beam backpropagate using ABCD matrices [32] all the way through our final lens of focal length f. The backpropagated beam is focused by the final lens at a distance z_{bp}. This tells us, what beam we have to generate to perform our transport. Coming back to the upper part of Fig. 7.1, assume that we have a collimated beam incident on our transport tunable lens. We want to generate our backpropagated transport beam from this incident collimated beam. For this to happen, we have to position our special, diverging tunable lens such that its separation from the final lens d and its negative focal length $f_{\mathrm{TL}}^{\mathrm{trans}}$ equal the backpropagated distance, z_{bp}, of our transport beam. This defined the *equation of backpropagation*:

$$z_{\mathrm{bp}} \stackrel{!}{=} d + f_{\mathrm{TL}}^{\mathrm{trans}}, \qquad f_{\mathrm{TL}}^{\mathrm{trans}} \in [-100\,\mathrm{mm}, \infty). \tag{7.1}$$

This condition already implies a negative focal length of the tunable lens. Therefore, we use here a different model (Optotune, *EL-16-40-TC, custom*), that is also able to generate negative focal lengths $f_{\mathrm{TL}}^{\mathrm{trans}} \in [-100\,\mathrm{mm}, \infty)$. If this condition can be fulfilled for the geometrically constrained distance d and the limited $f_{\mathrm{TL}}^{\mathrm{trans}}$, we can perform a transport over the distance z_{trans} with the desired waist w_{trans}.

Fig. 7.1 shows how the backpropagation distance z_{bp} varies as a function of the transport distance z_{trans}.

Given a transport distance z_{trans} and given that Eq. (7.1) can be fulfilled for this distance, a larger beam waist simplifies the transport since the focal length $f_{\mathrm{TL}}^{\mathrm{trans}}$ needs to be changed by a smaller amount. At the same time, if one is limited by the backpropagation distance z_{bp}, a smaller transport waist enables a larger transport distance. For large transport distances $z_{\mathrm{trans}} \sim 1000\,\mathrm{mm}$, the behavior of all waist sizes becomes comparable.

As a good starting compromise, we thus chose $w_{\mathrm{trans}} = 148\,\mu\mathrm{m}$ and realized it in Fig. 7.1 using $f_0 = 85\,\mathrm{mm}, f_1 = 77\,\mathrm{mm}$ and $f_2 = -105\,\mathrm{mm}$. The circular beam that marks our starting point of the transport was generated using $f_0 = 82\,\mathrm{mm}, f_1 = 51\,\mathrm{mm}$ and $f_2 \sim \infty$. We realized both configurations with the same input beam of $w = 0.47\,\mathrm{mm}$.

From the different focal lengths of the telescope tunable lenses we see, that in general, we need to vary the beam size before the transport tunable lens to generate a focus of constant waist. Only for the special case where $d = f$, one can see from a brief ray ABCD matrix optics calculation that we would obtain a *transport with conserved beam waist* [46]. Due to geometrical constrains like the *ideal scan condition*, necessary to achieve the maximum aspect ratio of the horizontal dipole trap, we can only come close but not actually meet this condition in our setup.

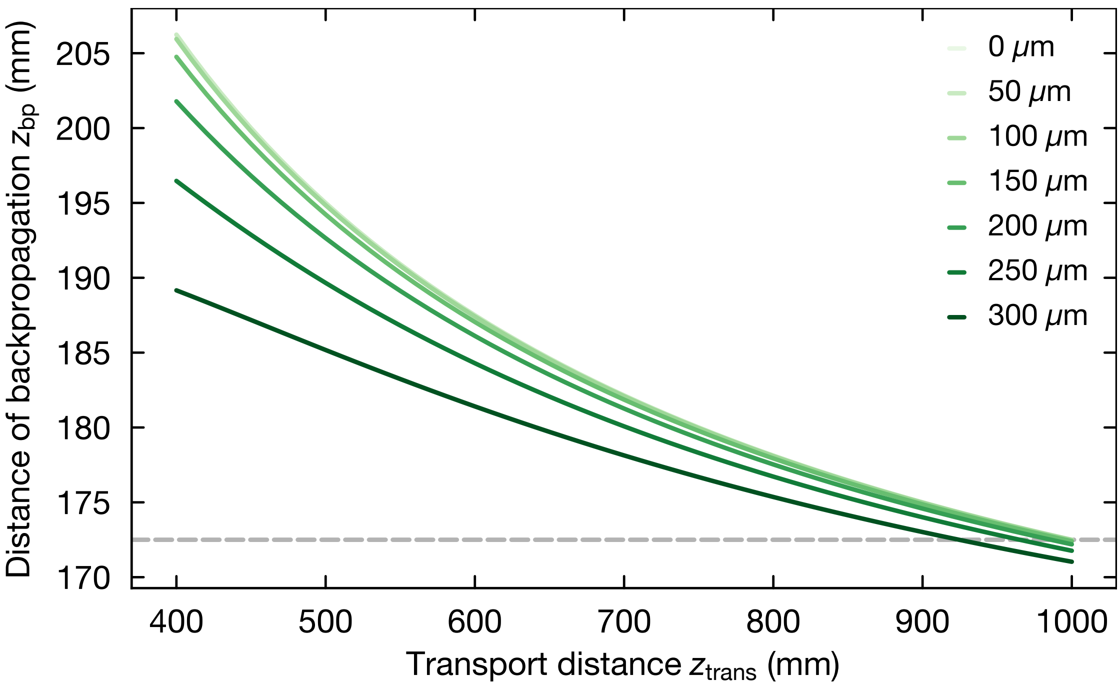

Figure 7.2 | Simulated backpropagation distance z_{bp} as function of transport distance z_{trans}. The backpropagation distance z_{bp} as function of transport distance z_{trans} was simulated with Gaussian ABCD matrix optics for different transport waists w_{trans} (green lines). The dashed line indicates the backpropagation distance of 172.4 mm used in Fig. 7.1 and approximately realized in the setup. As apparent from Eq. (7.1), the backpropagation distance can be tuned by changing the distance d between the final lens and the transport tunable lens, or by adjusting the focal length f_{TL}^{trans} of the transport tunable lens. Given a transport distance z_{trans} and given that Eq. (7.1) can be fulfilled for this distance, a larger beam waist makes it easier to transport since the focal length f_{TL}^{trans} needs to be changed by a smaller amount. At the same time, if one is limited by the backpropagation z_{bp}, a smaller transport waist enables a larger transport distance. For large transport distances $z_{trans} \sim 1000$ mm, the behavior of all waist sizes converges.

7.2 Performance

After the simulation, we can proceed to realize the optical transport in our test setup.

The test setup used is equivalent to the setting we plan to install in the experiment, which is shown in completeness in Fig. A.1 and Fig. A.2a. We determined the position of the focus using a beam profiler on a rail and finding the minimal cross-sectional area of the beam since this corresponds to the point of highest intensity in a real trap. First, we adjust the current through the tunable lenses i_0 and i_1 of the adjustable telescope to obtain a mean waist $w_{\text{trans}} = 148\,\mu\text{m}$ at the position of the atoms without using the transport tunable lens. Now, we subsequently increased the current of the transport tunable lens i_2 and adjusted the currents i_0 and i_1 to give the same waist w_{trans} in every measurement. We note that for continuous optical transport, different current ramp profiles can be used [46]. We then fit every measured beam with a 2D Gaussian and obtain its waists along the long and short axis, denoted w_D and w_d, respectively, and their ratio AR. The resulting pictures are shown in Fig. 7.3 with the corresponding currents in Fig. 7.4.

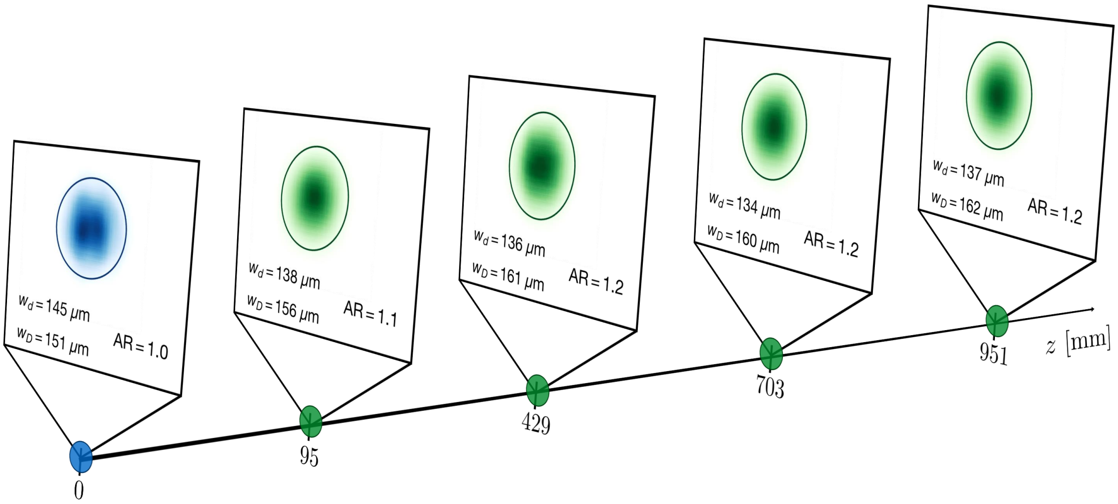

Figure 7.3 | Optical transport. Sample pictures of the beam at its focus were taken for different transport distances z_{trans} along the transport axis z. The beam colors correspond to the simulated beams in Fig. 7.1 and applied currents at each of the tunable lenses in Fig. 7.4. Every picture is fitted with a 2D Gaussian (solid lines mark the $1/e^2$ value) and shows the waists along the long and short axis of the beam, denoted w_D and w_d, respectively (solid lines), and their ratio AR. Without the transport lens, the reshaped circular beam (blue) is almost fully round with AR = 1.0. When the transport lens is actively operated, the beam acquires an additional astigmatism apparent by the larger AR ≈ 1.2. The additional astigmatism is comparable for all transport distances.

Without the transport lens, we can see that the reshaped circular beam is nearly round with

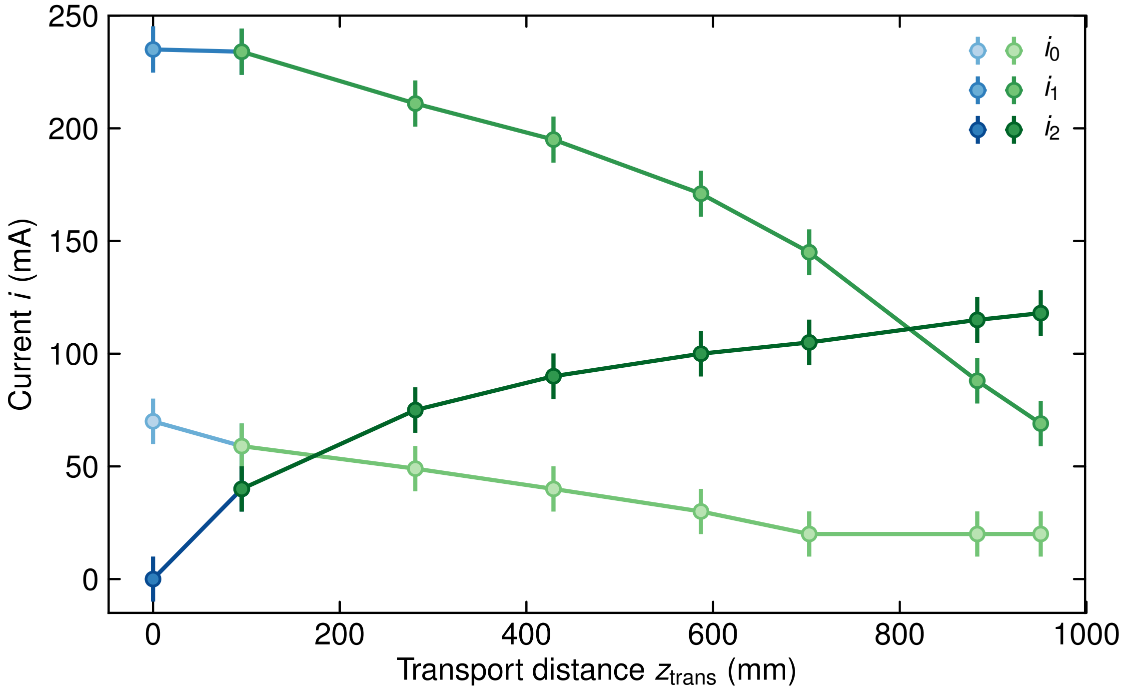

Figure 7.4 | Currents of the tunable lenses used for the optical transport. The currents applied to the three tunable lenses before (blue) and during transport (green) are shown (see Fig. 7.3). Higher currents translate to smaller focal lengths. No temperature stabilization was used in these measurements. All currents applied to the corresponding tunable lenses increase or decrease in a monotonous manner. For the telescope tunable lenses 0 and 1, the current is always positive and thus converging. For the transport tunable lens 3, the current is always negative and thus diverging.

AR = 1.0. When the transport lens is actively operated, the beam acquires an additional astigmatism apparent by the larger AR = 1.2. The additional astigmatism is comparable for all transport distances and thus the transported beam shape is nearly constant. A non-perfect alignment through the last lens is probably causing the astigmatism, since in the setup, both the tunable lens and the final lens are aligned with the same mirrors. For the alignment, we followed the same procedure outlined in Chapter 5.

During the individual measurements, we could observe that the focus position in the image plane on the beam profiler shifted by several mm. This in-plane shift is consistent with non-ideal alignment of the transport tunable lens. One improvement would be to change the last, fixed mirror on the vertical breadboard to a kinematic one. Also, Morales [45] reports that tilting the final lens helps to counteract the astigmatism caused by the transport tunable lens.

7.3 Trap potential and trap frequencies

Finally, we calculated the trapping potential along the axis of transport z using Eq. (6.1) and Eq. (2.10a) for a waist of 148 µm and a power of 15 W. We note again, that the tunable lenses are actually the most sensitive element in the optical setup with a maximum optical power density of $10\,\mathrm{kW/cm^2}$. In the simulation, the smallest beam at the tunable lenses is the input beam waist of $w_{\mathrm{in}} = 0.47\,\mathrm{mm}$ giving an optical power density of $\sim 2\,\mathrm{kW/cm^2}$, well below this threshold. The results of the calculations are shown in Fig. 7.5a.

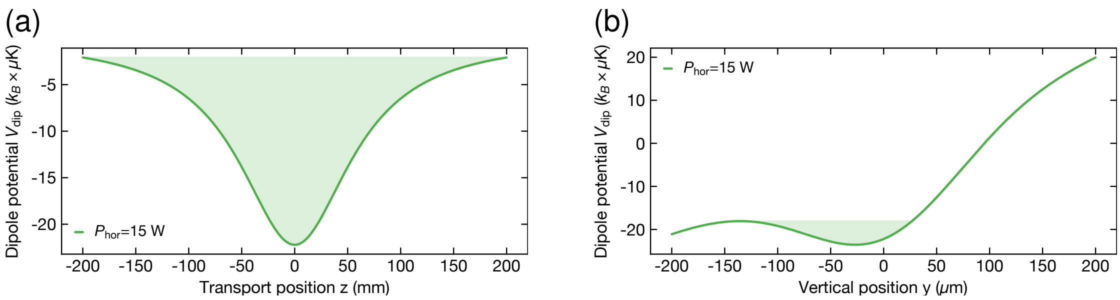

Figure 7.5 | Trapping potentials of the transport beam. (a) The dipole potential along the axis of transport z is calculated using Eq. (6.1) and Eq. (2.10a) for a waist of 148 µm and a power of 15 W. The resulting trap depth is $k_B \times 20\,\mu\mathrm{K}$ over the shown distance interval around the focus. The axial trap frequency according to Eq. (6.3) is $\omega_z = 2\pi \times 0.2\,\mathrm{Hz}$. ($b$) The dipole potential along the axis of gravity y is calculated in an analogue way. The resulting trap depth is $k_B \times 5\,\mu\mathrm{K}$. The corresponding trap frequency according to Eq. (6.3) is $\omega_y = 2\pi \times 99\,\mathrm{Hz}$.

Along the axis of transport, the trap depth is $k_B \times 20\,\mu\text{K}$ over the shown distance interval of 40 mm around the focus. One could think of decreasing the trap size in a real experiment to achieve stronger localization of the atoms. Léonard *et al.* [46] report on using $w_{\text{trans}} = 47\,\mu\text{m}$ and a power of 3.5 W for a transport distance of 28 cm with ^{87}Rb. The corresponding axial trap frequency is $\omega_z = 2\pi \times 0.2\,\text{Hz}$. If we choose the transport duration larger than $1/f_z$, we assume that the cloud adiabatically follows the transported trap and no dipole oscillations are excited. This would allow transport durations on the order of several seconds. We note that this is only a rough order of magnitude estimate and the exact proportionality has to be determined specifically, enabling ,*e.g.*, full suppression of these oscillations [46, 47].

We also calculated the dipole potential along the axis of gravity y for a waist of 148 µm and a power of 15 W. The resulting trap depth is $k_B \times 5\,\mu\text{K}$, which should be sufficient for the atoms in the red MOT with a temperature of ~ 1 µK. The corresponding trap frequency is $\omega_y = 2\pi \times 99\,\text{Hz}$.

Léonard *et al.* [46] found highly nonlinear behavior of heating and transport efficiency as functions of transport duration and power. Thus in conclusion, we expect the transport to happen on the order of several hundreds of µs without significant heating or atom loss, but the optimal parameters are yet to be determined in the experiment.

8 Conclusion and outlook

The goal of my Master's thesis was the design and implementation of a system that combines a shape and amplitude controllable optical dipole trap (ODT) with a means for optical transport.

In the setup presented here, we generated a time-averaged horizontal ODT for strontium atoms using an acousto-optic deflector (AOD) that scans a 1070 nm laser beam with a 10 kHz modulation frequency. We took advantage of a particular frequency modulation function [40], producing an elongated parabolic trap potential. Additionally, we used custom amplitude modulation to counteract the non-uniform efficiency of our AOD over the scan range. By applying dynamical beam shaping through our tunable telescope we achieved an elliptical horizontal ODT with small axis waist $w_{\text{hor},y} = 23\,\mu\text{m}$ in the vertical direction, and long axis waist $w_{\text{hor},x} = 541\,\mu\text{m}$ in the horizontal direction, yielding an aspect ratio of AR = 23.5. Subsequently, we plan on combining the horizontal with a vertical ODT of waist $w_{\text{ver}} = 58\,\mu\text{m}$ to generate a crossed dipole trap. Using typical beam powers for the vertical and horizontal ODT of $P_{\text{ver}} = 100\,\text{mW}$ and $P_{\text{hor}} = 5\,\text{W}$ [19], we expect a trap depth of $k_B \times 10\,\mu\text{K}$ along the vertical axis of gravity. This trap depth should be sufficient to trap atoms from our second, "red" magneto-optical trap (MOT) with a temperature of $\sim 1\,\mu\text{K}$. The corresponding trap frequencies are $\omega_x = 2\pi \times 57\,\text{Hz}$ in the horizontal direction, $\omega_y = 2\pi \times 488\,\text{Hz}$ along the axis of gravity and $\omega_z = 2\pi \times 53\,\text{Hz}$ along the axis of transport. All trap frequencies are considerably smaller than the modulation frequency ensuring that the atoms will experience a time-averaged potential.

To prepare the horizontal ODT for optical transport, we reshaped the horizontal ODT from an elliptical to a circular shape, resulting in a waist of $w_{\text{trans}} = 148\,\mu\text{m}$. By using a third focus-tunable lens in a diverging mode, while also simultaneously adjusting the tunable telescope, we achieved a reproduction of the same waist over a distance of 95 cm. Using an optical power of $P_{\text{trans}} = 15\,\text{W}$, the resulting trap depth is $k_B \times 5\,\mu\text{K}$ along the axis of gravity, which should be sufficient to transport the atoms without significant losses. The trap frequency along the axis of transport is $\omega_z = 2\pi \times 0.2\,\text{Hz}$, that also determines the order of magnitude of the transport duration, expected to be several seconds [46].

Looking towards the future, several aspects are yet to be addressed: Regarding the scan system, PID controlling the desired amplitude modulation would be desirable to achieve even more homogeneous trap shapes. Additionally, the temperature stabilization of all tunable lenses used in the setup to ensure reproducible and stable performance will be of major importance. Undoubtedly, however, the comparison between the theoretical predictions and the optimal experimental parameters will be of greatest interest to us, especially with regards to evaporative cooling. It will be exciting to see how the setup engineered here integrates into the experimental apparatus and we hope that it serves as a valuable addition to our experiment on the way of exploring fascinating quantum many-body physics with strontium.

Acknowledgements

First of all, I want to thank my supervisor, Dr. Sebastian Blatt. His deep and precise knowledge about everything related to the experiment and far beyond never stopped to amaze me. None of my questions were left unanswered, and he undoubtedly is a guidance for me in many ways. I am very grateful to him for giving me the opportunity to learn so much about so many different areas during my time in the strontium lab.

I would also like to thank Professor Immanuel Bloch for giving me the opportunity to work in his group, when TUM students were not yet such a frequent appearance in the quantum many-body physics division at MPQ. I am much obliged for his constant support in all kinds of matters.

I am also deeply grateful to Professor Rudolf Gross. His help and advice during my whole studies, including this thesis, was indispensable. I cannot imagine how my way would have gone without him.

A big thanks goes to the whole strontium lab team. Annie, who was a great office mate and simply is the nicest person I have *ever* met. Her knowledge about every screw of the experimental apparatus and sequence always was very valuable. André, for being my fitness and kicker buddy and for sharing *so* many funny hours. I also want to thank him for sharing his physics and lab experience, as well as many other insights, with me. Stepan, for simply being, among many other fields, *the* IT guy. His programming abilities are marvelous and I am grateful to have picked up a little bit of it. He always had a friendly ear for all my problems, including proof reading the thesis, and I wish him all the best for his new career in “crypto”. Neven, for already being such a great addition to the lab. How fast he worked himself into the experiment is really admirable. I am also deeply grateful for his extensive, high-frequency proof reading, which teached me a lot about writing. Stephan, for his valuable lessons to a soon-to-be master’s student. Rudi, for sharing many, insightful moments in figuring out electronics problems. I am sure, he will have many more, after taking over this job now. Etienne, for bringing some excellent British humor to the lab. His proof reading was very valuable and he always teaches me new, incredibly fancy words. Lukas, for nice talks during his Bachelor’s thesis and afterwards. Also, I want to thank all our interns Luisa, Emil and Lucas. All of them were a lot of fun to work with, and I probably learned as much as they did during our collaborations.

Of course, I am more than thankful to all other members of the Bloch group. Since naming them all would probably take up too much space, I will simply say that they all made me feel like a part of a big family. I have so many good memories about our times together: let it be the daily kicker at MPQ or abroad at conferences and our group retreat. I do hope to see many of you again sometime, somewhere.

I would also like to thank the technical staff at MPQ, Anton, Olivia and Karsten, for teaching me how to design and assemble all kinds of electronic and mechanical pieces of art, and generally always helping me wherever they could.

Finally, I would like to thank my family, for supporting me, no matter where my ways take me.

Bibliography

[1] Cisco, *The Zettabyte Era: Trends and Analysis*, White paper (2017), `https://www.cisco.com/c/en/us/solutions/collateral/service-provider/visual-networking-index-vni/vni-hyperconnectivity-wp.pdf` (Cited on page **7**).

[2] I. M. Georgescu, S. Ashhab, and F. Nori, *Quantum simulation*, Reviews of Modern Physics **86**, 153 (2014) (Cited on page **7**).

[3] R. Gross and A. Marx, *Festkörperphysik*, Walter de Gruyter GmbH (2018) (Cited on page **7**).

[4] M. Greiner, O. Mandel, and T. Esslinger, *Quantum phase transition from a superfluid to a Mott insulator in a gas of ultracold atoms*, Nature **415**, 6 (2002) (Cited on page **7**).

[5] F. Dalfovo, S. Giorgini, L. P. Pitaevskii, and S. Stringari, *Theory of Bose-Einstein condensation in trapped gases*, Reviews of Modern Physics **71**, 463 (1999) (Cited on page **7**).

[6] R. Grimm, M. Weidemüller, and Y. B. Ovchinnikov, *Optical dipole traps for neutral atoms*, Advances in atomic, molecular, and optical physics (2000) (Cited on pages **7**, **21**, **22**).

[7] T. Esslinger, *Fermi-Hubbard Physics with Atoms in an Optical Lattice*, Annual Review of Condensed Matter Physics **1**, 129 (2010) (Cited on page **7**).

[8] W. Hofstetter, J. I. Cirac, P. Zoller, E. Demler, and M. D. Lukin, *High-Temperature Superfluidity of Fermionic Atoms in Optical Lattices*, Physical Review Letters **89** (2002) (Cited on page **7**).

[9] P. A. Lee, N. Nagaosa, and X.-G. Wen, *Doping a Mott insulator: Physics of high-temperature superconductivity*, Reviews of Modern Physics **78**, 17 (2006) (Cited on page **7**).

[10] K. Le Hur and M. T. Rice, *Superconductivity close to the Mott state: From condensed-matter systems to superfluidity in optical lattices*, Annals of Physics (2009) (Cited on page **7**).

[11] W. S. Bakr, J. I. Gillen, A. Peng, S. Fölling, and M. Greiner, *A quantum gas microscope for detecting single atoms in a Hubbard-regime optical lattice*, Nature **462**, 74 (2009) (Cited on page **7**).

[12] J. F. Sherson, C. Weitenberg, M. Endres, M. Cheneau, I. Bloch, and S. Kuhr, *Single-atom-resolved fluorescence imaging of an atomic Mott insulator*, Nature **467**, 68 (2010) (Cited on page **7**).

[13] C. Gross and I. Bloch, *Quantum simulations with ultracold atoms in optical lattices*, Science **357**, 995 (2017) (Cited on page **8**).

[14] I. Bloch, J. Dalibard, and W. Zwerger, *Many-body physics with ultracold gases*, Reviews of Modern Physics **80**, 885 (2008) (Cited on page **8**).

[15] A. J. Daley, *Quantum computing and quantum simulation with group-II atoms*, Quantum Information Processing **10**, 865 (2011) (Cited on page **8**).

[16] A. D. Ludlow, M. M. Boyd, J. Ye, E. Peik, and P. O. Schmidt, *Optical atomic clocks*, Reviews of Modern Physics **87**, 637 (2015) (Cited on page **8**).

[17] H. J. Metcalf and P. Van der Straten, *Laser cooling and trapping*, Springer (1999) (Cited on pages **8, 13, 14, 17, 18, 21**).

[18] S. L. Campbell, R. B. Hutson, G. E. Marti, A. Goban, N. Darkwah Oppong, R. L. McNally, L. Sonderhouse, J. M. Robinson, W. Zhang, B. J. Bloom, and J. Ye, *A Fermi-degenerate three-dimensional optical lattice clock*, Science **358**, 90 (2017) (Cited on pages **8, 12**).

[19] S. Stellmer, R. Grimm, and F. Schreck, *Production of quantum-degenerate strontium gases*, Physical Review A **87** (2013) (Cited on pages **8, 11, 63, 67, 69, 77**).

[20] M. M. Boyd, *High Precision Spectroscopy of Strontium in an Optical Lattice: Towards a New Standard for Frequency and Time*, PhD thesis, University of Colorado (2002) (Cited on pages **12, 19, 20**).

[21] M. M. Boyd, T. Zelevinsky, A. D. Ludlow, S. Blatt, T. Zanon-Willette, S. M. Foreman, and J. Ye, *Nuclear spin effects in optical lattice clocks*, Physical Review A **76** (2007) (Cited on page **12**).

[22] M. Inguscio and L. Fallani, *Atomic physics: precise measurements and ultracold matter*, Oxford University Press (2013) (Cited on pages **15, 16, 18**).

[23] N. Ramsey, *Molecular beams*, Oxford University Press (1990) (Cited on page **15**).

[24] R. G. Escudero, *Magnetic Field Control and Laser Frequency Stabilization for Strontium Magneto-Optical Traps*, Master's thesis, Ludwig-Maximillians-Universität München (2016), `http://ultracold.sr/publications/thesis_rodrigo_gonzalez_escudero.pdf` (Cited on page **19**).

[25] T. H. Loftus, T. Ido, M. M. Boyd, A. D. Ludlow, and J. Ye, *Narrow line cooling and momentum-space crystals*, Physical Review A **70** (2004) (Cited on page **19**).

[26] J. P. Bartolotta, M. A. Norcia, J. R. K. Cline, J. K. Thompson, and M. J. Holland, *Laser cooling by sawtooth-wave adiabatic passage*, Physical Review A **98** (2018) (Cited on page **21**).

[27] L. Allen and J. H. Eberly, *Optical Resonance and Two-level Atoms*, Courier Corporation (1987) (Cited on page **22**).

[28] B. Saleh and M. C. Teich, *Fundamentals of Photonics*, Wiley (2007) (Cited on pages **23, 27, 31, 36, 38, 39, 44, 50, 57, 60**).

[29] IPG Photonics, *YLR-100-LP-WC datasheet*, Datasheet (2017) (Cited on page **25**).

[30] N. Janša, *A frequency-stable diode laser system for spectroscopy and trapping of Sr atoms*, Master's thesis, Ludwig-Maximillians-Universität München (2016), `http://ultracold.sr/publications/thesis_nejc_jansa.pdf` (Cited on page **28**).

[31] A. Siegman, *Lasers*, University Science Book (1986) (Cited on pages **29, 31**).

[32] S. Wissenberg, *Stabilizing diode lasers to an ultrastable reference cavity*, Master's thesis, Ludwig-Maximillians-Universität München (2017), `http://ultracold.sr/publications/thesis_stephan_wissenberg.pdf` (Cited on pages **30, 64, 69, 71**).

[33] M.-A. Lapointe and M. Piché, *Linewidth of high-power fiber lasers*, Photonics North 2009 **7386** (2009) (Cited on page **31**).

[34] V. Roy, M. Piché, F. Babin, and G. W. Schinn, *Nonlinear wave mixing in a multilongitudinal-mode erbium-doped fiber laser*, Optics Express **13**, 6791 (2005) (Cited on page **31**).

[35] Isomet, *Maximizing AO Diffraction Efficiency*, Application note (2006), `http://www.isomet.com/App-Manual_pdf/Maximizing%20DE.pdf` (Cited on page **37**).

[36] Isomet, *All About Bragg Angle Error in AO Modulators & Deflectors*, Application note (2007), `http://www.isomet.com/App-Manual_pdf/Bragg%20Angle%20Errors.pdf` (Cited on pages **38, 39, 47**).

[37] Isomet, *AO Scanning*, Application note (2004), `http://www.isomet.com/App-Manual_pdf/AO%20Scanning.pdf` (Cited on pages **43, 44**).

[38] Gooch & Housego, *AOMO 3080-198 datasheet*, Datasheet (2015) (Cited on pages **43, 44, 46, 47**).

[39] Gooch & Housego, *AODF 4090-6 datasheet*, Datasheet (2013) (Cited on pages **43, 44, 47, 64**).

[40] R. Roy, A. Green, R. Bowler, and S. Gupta, *Rapid cooling to quantum degeneracy in dynamically shaped atom traps*, Physical Review A **93** (2016) (Cited on pages **50, 51, 77**).

[41] C. Kohstall, *A New Toolbox for Experiments with Ultracold ^{6}Li*, Master's thesis, Universität Innsbruck (2007), `http://www.ultracold.at/theses/diplom_christoph_kohstall/diplomarbeit_christoph_kohstall.pdf` (Cited on page **51**).

[42] S. Baier, *An optical dipole trap for Erbium with tunable geometry*, Master's thesis, Universität Innsbruck (2012), `http://www.erbium.at/FF/wp-content/uploads/2015/10/master_simon_baier.pdf` (Cited on pages **51, 53, 61, 67**).

[43] C. Politi, *Optical dipole trap for an erbium and dysprosium mixture*, Master's thesis, Eidgenössische Technische Hochschule Zürich (2016), `http://www.erbium.at/FF/wp-content/uploads/2017/11/Master_Claudia_Politi.pdf` (Cited on page **51**).

[44] Optotune, *EL-10-30-TC datasheet*, Datasheet (2018), `https://www.optotune.com/images/products/Optotune%20EL-10-30.pdf` (Cited on pages **56, 57, 64**).

[45] A. Morales, *Temperature stabilized optical transport with focus-tunable lenses*, Master's thesis, Eidgenössische Technische Hochschule Zürich (2013) (Cited on pages **57, 75**).

[46] J. Léonard, M. Lee, A. Morales, T. M. Karg, T. Esslinger, and T. Donner, *Optical transport and manipulation of an ultracold atomic cloud using focus-tunable lenses*, New Journal of Physics **16**, 093028 (2014) (Cited on pages **71, 73, 76, 77**).

[47] A. Couvert, T. Kawalec, G. Reinaudi, and D. Guéry-Odelin, *Optimal transport of ultracold atoms in the non-adiabatic regime*, EPL (Europhysics Letters) **83**, 13001 (2008) (Cited on page **76**).

A

Complete optical setup

In this part of the Appendix, we present the complete optical setup, that was designed and implemented during this Master's thesis.

The first part of the complete optical setup is used for generating the vertical optical dipole trap (VODT) and part of the horizontal optical dipole trap (HODT) and shown in Fig. A.1

After the fiber output, the laser is attenuated and split into the HODT and VODT part. The attenuators and splits consist of $\lambda/2$ plates in combination with a Brewster plate.

The sub-setup left from the laser fiber output is used for the vertical optical dipole trap (VODT). In the sub-setup, we currently use a 3:1 telescope composed of a 100 mm lens (Thorlabs, *LA4380-YAG-ML*) and a 30 mm lens (Optosigma, *HFTLSQ-20-30PF1*) that collimates the beam from $w_0 = 1.41\,\mathrm{mm} \rightarrow 0.79\,\mathrm{mm}$ at the AOM (Gooch & Housego, *AOMO 3080-198*), used for intensity control. The beam is then fiber coupled to a polarization maintaining, single mode 1064 nm fiber (Thorlabs, *P3-1064PM-FC-5*). We plan to subsequently extend the beam to $w_0 = 4.4\,\mathrm{mm}$ and focus it onto the atoms by a 750 mm lens. This procedure would give us a waist of $w_{\mathrm{ver}} = 58\,\mu\mathrm{m}$ for the VODT.

The rest of the setup is used for the horizontal optical dipole trap (HODT). The beam is collimated at the position of the AOD having a waist $w_0 = 0.47\,\mathrm{mm}$. To benchmark the scanning system, an optional test point after the AOD consisting of a mirror and a lens of focal length $f = 100\,\mathrm{mm}$ at a distance f from the AOD can be set up. The angular movement of the AOD is reproduced at the vertical breadboard (see Fig. A.2a) by a $4f$ system consisting of two 500 mm lenses.

This vertical breadboard is the second part of the complete optical setup, shown in Fig. A.2a.

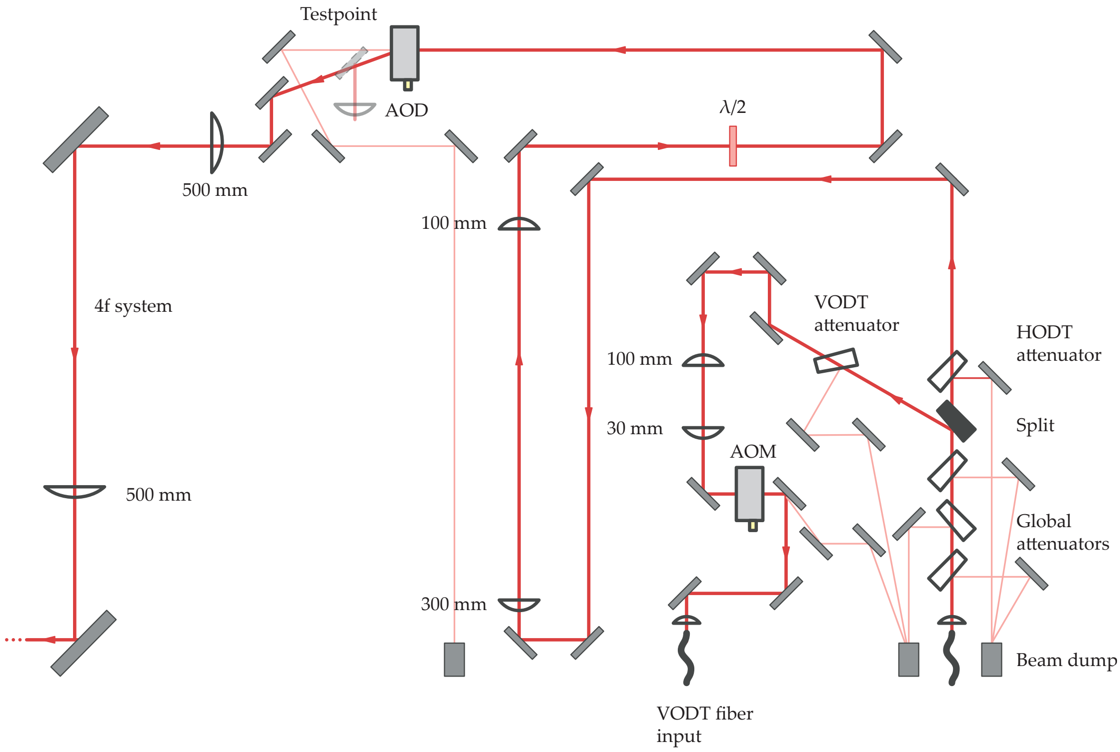

Figure A.1 | Complete optical setup part 1. Beams relevant for operation are shown in red, beams not relevant for operation are marked in light red. After the fiber output, the laser is attenuated and split into the HODT and VODT part. The sub-setup left from the laser fiber output is used for the vertical optical dipole trap (VODT). The rest of the setup is used for the horizontal optical dipole trap (HODT). To benchmark the scanning system, an optional test point after the AOD consisting of a mirror and a lens can be set up. The angular movement of the AOD is reproduced at the vertical breadboard (see Fig. A.2a) by a $4f$ system. The red dots indicate the starting point of Fig. A.2a. The distances and angles are not to scale.

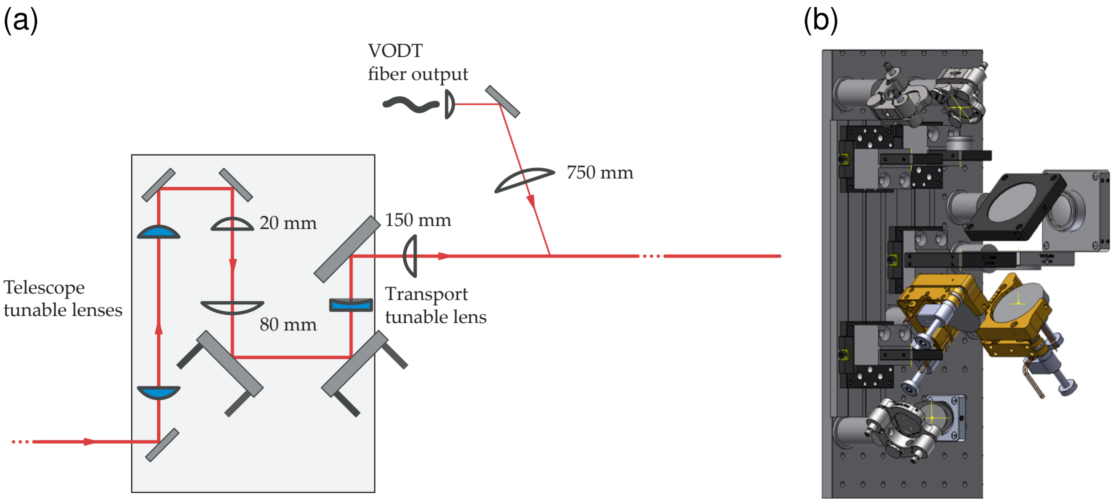

Figure A.2 | Complete optical setup part 2. Continuing from the red dots of Fig. A.1. (*a*) The different tunable lenses are marked in blue. The HODT beam is first sent through two of the tunable lenses in a telescope configuration. Subsequently the beam is magnified by a 1:4 telescope. Large mirrors with handles mark picomotor operated 2"mirrors. Finally, the beam passes another tunable lens and is focused by a 150 mm final lens onto the atoms. The VODT beam is planned to be focused down by a 750 mm lens onto the atoms. (*b*) Drawing of the vertical setup in Autodesk Inventor.

After the $4f$ system, the HODT beam is first sent through two of the tunable lenses in a telescope configuration. Subsequently the beam is magnified by a 1:4 telescope consisting of a 20 mm and 80 mm lens. The beam is aligned using 2"mirrors with picomotors (Newport, *8302 Picomotor Actuator*). Finally, the beam passes the tunable lens used for transport (Optotune, *EL-16-40-TC, custom*) and is focused by a final lens of focal length 150 mm onto the atoms.

B

Measuring relative intensity noise (RIN)

The following part is a manual for measuring the relative intensity noise of a laser.

To measure relative intensity noise (RIN), your setup will consist of a laser, a photodiode with at least one DC output (PD), a voltmeter (VM), the FFT machine (FFT) and the spectrum analyzer (SA).

Components

- *Laser:* For the measurement, the laser has to be attenuated with beam samplers, filters etc., to not damage the used photodiode, and still remaining in the linear region of the photodiode (both usually indicated in the data sheet of the photodiode model).

- *Photodiode:* Be sure to choose a model that is specified for your wavelength, power etc., and put in appropriate gain resistors, as well as filter capacitors. To differentiate between noise/oscillations of the photodiode and the laser, you should know the spectrum of your photodiode.

- *True-RMS Voltmeter:* Use one of the voltmeters to measure the carrier power.

- *FFT machine:* Set the FFT machine up via Ethernet using the `sr760.py` in the srlab hardware folder. Choose a frequency range up to 100 kHz. Set the units to $\mathrm{dBV_{rms}}/\sqrt{\mathrm{Hz}}$.

- *Spectrum Analyzer:* To get your data from the spectrum analyzer, prepare a USB stick and make sure to use the `anritsu.py` in the srlab hardware folder. Set the spectrum analyzer to RMS measurement method and to the frequency range you want to cover. Be sure to use an input attenuator.

Measurement

When you set up the components individually, we can start putting everything together.

- P_{dc} *with voltmeter:* Connect one DC output of the photodiode to a voltmeter. Note the RMS value of the voltage displayed on the voltmeter.

- *Spectrum from mHz to* 100 *kHz with FFT machine:* Now connect the same DC output to the FFT machine's input. Adjust the reference level such that you make use the whole range of the screen. Get your data and note the RBW.

- *Spectrum from* 9 *kHz to* 7.1 *GHz with Spectrum analyzer*: Now connect the same DC output to the spectrum analyzer. In general, it makes sense to run the spectrum analyzer one time with very small RBW to see which frequency regions show peaks and should be investigated. If you know where you want to look, define your new frequency range and set the resolution bandwidth (RBW) such that you are able to identify all relevant features in this region. Save your data to a USB stick and note the RBW used for every measurement.

Analysis

Every measurement device mentioned beforehand will give you its data in a different unit. The following sections describe how to convert these units to the ones you want for RIN measurements. This unit is dBc/Hz. It renders your RIN measurement independent of the laser power and RBW you used. Thus, it simplifies the comparison with other RIN measurements.

- *Voltmeter:* The voltmeter gives you a rms voltage U_{VM}, which you can use to calculate the carrier power of your laser light:

$$P_{\mathrm{dc}} = U_{\mathrm{VM}}^2 / Z_{\mathrm{VM}}$$

using its input impedance $Z_{\mathrm{VM}} = 10\mathrm{M}\Omega$.

- *FFT machine:* Your measured data is in $\mathrm{dBV_{rms}}/\sqrt{\mathrm{Hz}}$, taken by the FFT machine with certain RBW. First, convert it to

$$\mathrm{data(dBV_{rms})} = \mathrm{data(dBV_{rms}}/\sqrt{\mathrm{Hz}}) + 20\log(\sqrt{\mathrm{RBW/Hz}})$$

To convert this to rms voltage:

$$\mathrm{data(V_{rms})} = 10^{\mathrm{dBV_{rms}}/20}$$

Since the FFT machine's input impedance $Z_{\mathrm{FFT}} = 1\ \mathrm{M}\Omega$ is much greater than the output impedance of the photodiode $Z_{\mathrm{PD}} = 50\Omega$, we can safely assume that the measured voltage at the FFT machine is equal to the voltage at the photodiode with negligible error. Now you can calculate the power present at the FFT machine using

$$P_{\mathrm{FFT}} = \mathrm{data(V_{rms})}^2 / Z_{\mathrm{FFT}}$$

and then normalize it to your carrier power measured at the voltmeter

$$\mathrm{data(dBc)} = 10\log_{10}(P_{\mathrm{FFT}}/P_{\mathrm{dc}})$$

To normalize your data to 1 Hz and rendering it independent of the used RBW:

$$\mathrm{data(dBc/Hz)} = \mathrm{data(dBc)} - 10\log_{10}(\mathrm{RBW/Hz})$$

- *Spectrum analyzer:* Your measured data is in dBm, taken by the spectrum analyzer with certain RBW. First, get rid of your input attenuator by

$$\mathrm{data(dBm)} = \mathrm{rawdata(dBm)} + \mathrm{attenuator(dB)}$$

The input impedance of the spectrum analyzer $Z_{\mathrm{SA}} = 50\Omega$ in combination with

$Z_{\mathrm{PD}} = 50\Omega$ creates a $1:2$ voltage divider. Your carrier power is thus

$$P_{\mathrm{dc}} = \frac{(U_{\mathrm{VM}}/2)^2}{Z_{\mathrm{SA}}}$$

Now you calculate the power present at the spectrum analyzer using

$$P_{\mathrm{SA}} = 1\ \mathrm{mW} \cdot 10^{\frac{\mathrm{dBm}}{10}}$$

After that, convert your data again to dBc and subsequently dBc/Hz as described in the preceding paragraph.

Finally, just stack your different graphs now all in dBc/Hz together.

C

AOM/AOD Driver Characterization

This part of the appendix is a summary of the calibration curves of the used AOM and AOD driver.

We measured the output power of both driver modules P_{driver} as a function of the input voltage AM at the amplitude modulation input. We then fit the data with a polynomial of 3[rd] order $\frac{P_{\mathrm{driver}}}{\mathrm{W}} = \sum_{i0}^{3} a_i(\frac{\mathrm{AM}}{\mathrm{V}})$. Also, we measured the output acoustic frequency of the driver modules determined by the built-in VCO as a function of the input voltage FM at the frequency modulation input. The data is fitted with a linear function $\frac{F}{\mathrm{MHz}} = y_0 + k \cdot \frac{\mathrm{FM}}{\mathrm{V}}$.

The results are shown in Fig. C.1a, Fig. C.1b, Fig. C.2a, and Fig. C.2b.

We first look at the AOM Driver module. There, we obtain for the fitted AM curve the coefficients $a_0 = 0.02 \pm 0.01$, $a_1 = -0.07 \pm 0.01$, $a_2 = 0.16 \pm 0.01$ and $a_3 = -0.012 \pm 0.001$. For the FM curve, we obtain the parameters $y_0 = 64.3 \pm 0.3$ and $k = 8.4 \pm 0.1$.

Now, we analyze the AOD Driver module. There, we obtain for the fitted AM curve very similar coefficients $a_0 = 0.02 \pm 0.01$, $a_1 = -0.08 \pm 0.02$, $a_2 = 0.17 \pm 0.01$ and $a_3 = -0.013 \pm 0.001$ For the FM curve, we obtain the parameters $y_0 = 65.7 \pm 0.3$ and $k = 5.6 \pm 0.1$.

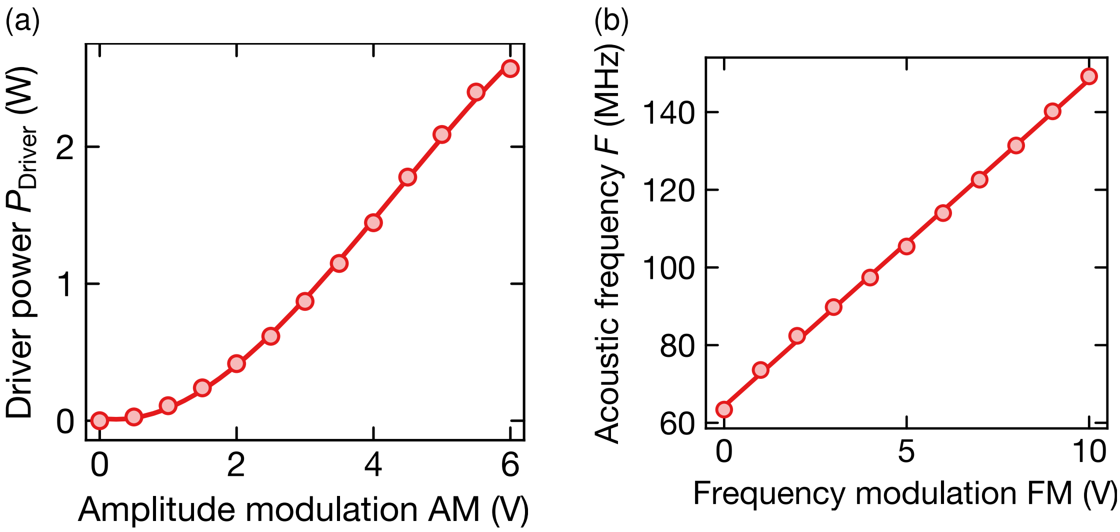

Figure C.1 | Characterization of the AOM driver module. (a) The output power of the driver module P_{driver} was measured as a function of the input voltage AM at the amplitude modulation input. The data is fitted with a polynomial of 3^{rd} order $\frac{P_{\mathrm{driver}}}{\mathrm{W}} = \sum_{i_0}^{3} a_i(\frac{\mathrm{AM}}{\mathrm{V}})$ where $a_0 = 0.02 \pm 0.01$, $a_1 = -0.07 \pm 0.01$, $a_2 = 0.16 \pm 0.01$ and $a_3 = -0.012 \pm 0.001$ (solid line). (b) The output acoustic frequency of the driver module determined by the built-in VCO was measured as a function of the input voltage FM at the frequency modulation input. The data is fitted with a linear function $\frac{F}{\mathrm{MHz}} = y_0 + k \cdot \frac{\mathrm{FM}}{\mathrm{V}}$ where $y_0 = 64.3 \pm 0.3$ and $k = 8.4 \pm 0.1$ (solid line).

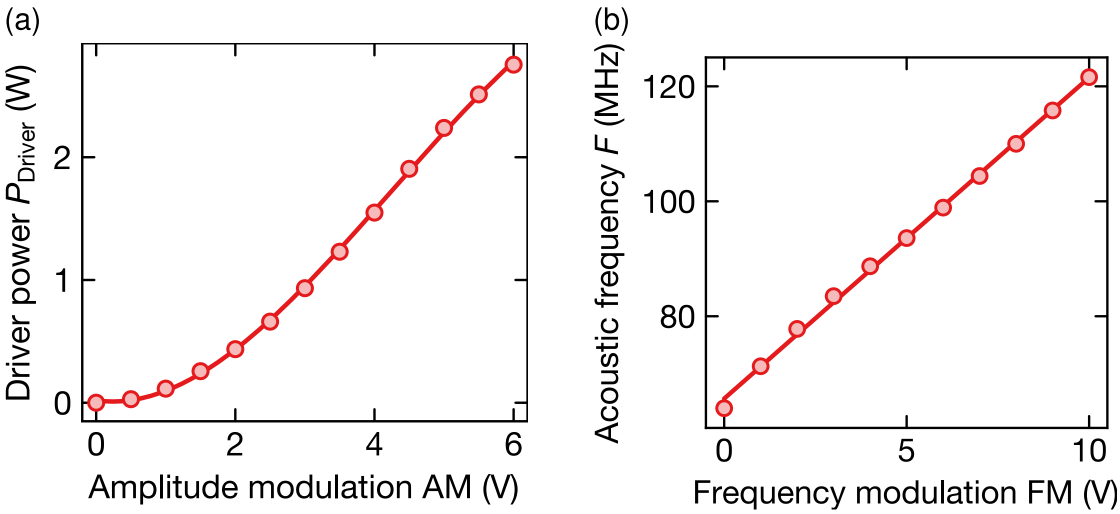

Figure C.2 | Characterization of the AOD driver module. (a) The output power of the driver module P_{driver} was measured as a function of the input voltage AM at the amplitude modulation input. The data is fitted with a polynomial of 3^{rd} order $\frac{P_{\mathrm{driver}}}{\mathrm{W}} = \sum_{i_0}^{3} a_i(\frac{\mathrm{AM}}{\mathrm{V}})$ where $a_0 = 0.02 \pm 0.01$, $a_1 = -0.08 \pm 0.02$, $a_2 = 0.17 \pm 0.01$ and $a_3 = -0.013 \pm 0.001$ (solid line). (b) The output acoustic frequency of the driver module determined by the built-in VCO was measured as a function of the input voltage FM at the frequency modulation input. The data is fitted with a linear function $\frac{F}{\mathrm{MHz}} = y_0 + k \cdot \frac{\mathrm{FM}}{\mathrm{V}}$ where $y_0 = 65.7 \pm 0.3$ and $k = 5.6 \pm 0.1$ (solid line).

Erklärung

Ich versichere hiermit, dass ich die von mir eingereichte Abschlussarbeit selbstständig verfasst und keine anderen als die angegebenen Quellen und Hilfsmittel benutzt habe.

Garching, 5.10.2018, Unterschrift